/N,-20
69306
P- 109

NASA

A STUDY OF IGNITION AND SIMULATION CIRCUITS FOR ARCJET THRUSTERS

prepared for

LEWIS RESEARCH CENTER
NATIONAL AERONAUTICS AND SPACE ADMINISTRATION

GRANT NAG3-1102

by

Thomas A. Stuart
Roger J. King
Gene P. Altenburger

December 1991

Department of Electrical Engineering
The University of Toledo
Toledo, Ohio 43606

REPORT DOCUMENTATION PAGE

Public reporting burden for this collection of information is estimated to average 1 hour per response, including the time for reviewing instructions, searching existing data sources, gathering and maintaining the data needed, and completing and reviewing the collection of information. Send comments regarding this burden estimate or any other aspect of this collection of information, including suggestions for reducing this burden, to Washington Headquarters Services, Directorate for Information Operations and Reports, 1215 Jefferson Davis Highway, Suite 1204, Arlington, VA 22202-4302, and to the Office of Management and Budget, Paperwork Reduction Project (0704-0188), Washington, DC 20503.

1. AGENCY USE ONLY (Leave blank)	2. REPORT DATE	3. REPORT TYPE AND DATES COVERED
	December 1991	Final Contractor Report

4. TITLE AND SUBTITLE

A Study of Ignition and Simulation Circuits for Arcjet Thrusters

5. FUNDING NUMBERS

Grant NAG3-1102

6. AUTHOR(S)

Thomas A. Stuart
Roger J. King
Gene P. Altenburger

7. PERFORMING ORGANIZATION NAME(S) AND ADDRESS(ES)

Department of Electrical Engineering
University of Toledo
Toledo, OH 43606

8. PERFORMING ORGANIZATION REPORT NUMBER

NASA CR-189097

9. SPONSORING/MONITORING AGENCY NAME(S) AND ADDRESS(ES)

National Aeronautics and Space Administration
Lewis Research Center
Cleveland, Ohio 44135-3191

10. SPONSORING/MONITORING AGENCY REPORT NUMBER

11. SUPPLEMENTARY NOTES Grant Technical Offices-John A. Hamley, NASA Lewis Research Center, Cleveland, OH 44125. This report is presented in two parts: Part I deals with the simulation of arcjet loads and is based on the MSEE thesis of G. Altenburger. Part II describes the design and testing of a 1kW arcjet power supply.

12a. DISTRIBUTION/AVAILABILITY STATEMENT

Unclassified - Unlimited
Subject Category

12b. DISTRIBUTION CODE

13. ABSTRACT (Maximum 200 words)

Part I: A 1-kW electronic load was programmed to simulate the nonlinear v-i character-istics of an arcjet, both ignited and un-ignited. The simulator was tested and found to closely resemble an arcjet both for large transients and small perturbances up to about 40 kHz. No attempt was made to simulate the ignition process itself. The dynamic behavior of the arcjet (and the simulator) was shown to differ significantly from that of a resistor bank.

Part II: Previous research described in [12] led to the design and construction of a 1 KW arcjet power supply. A high voltage ignition circuit was added to this hardware, and tests on a 1KW arcjet were performed at NASA LeRC. All tests were successful and no ignition failures were observed. Circuit documentation and test results are included.

14. SUBJECT TERMS Arcjet simulation, high voltage ignition, phase shift control.

15. NUMBER OF PAGES

16. PRICE CODE

17. SECURITY CLASSIFICATION OF REPORT	18. SECURITY CLASSIFICATION OF THIS PAGE	19. SECURITY CLASSIFICATION OF ABSTRACT	20. LIMITATION OF ABSTRACT
Unclassified	Unclassified	Unclassified	

Part I

Simulation of an Electric Arc Using a Nonlinear Active Load

Chapter 5: SUMMARY for PART I 64

Part II

ARCJET IGNITION CIRCUIT DEVELOPMENT

Chapter 6: INTRODUCTION 73

Chapter 7: THEORY OF OPERATION for Ignition Circuit.......81

Chapter 8: EXPERIMENTAL RESULTS 89

Chapter 9: SUMMARY for PART II...............103

Chapter 1

INTRODUCTION

1.1   BACKGROUND

In recent years arcjet thrusters have found increased use in aerospace applications. Originally developed in the 1950s and 1960's, the arcjet thruster can be described as a device in which an arc is created in the presence of a propellant, with the resultant hot gases expanded through a nozzle creating a thrust in the opposite direction. The cutaway view of an arcjet thruster is shown in Fig. 1.1. The thruster has been described in detail elsewhere [1].
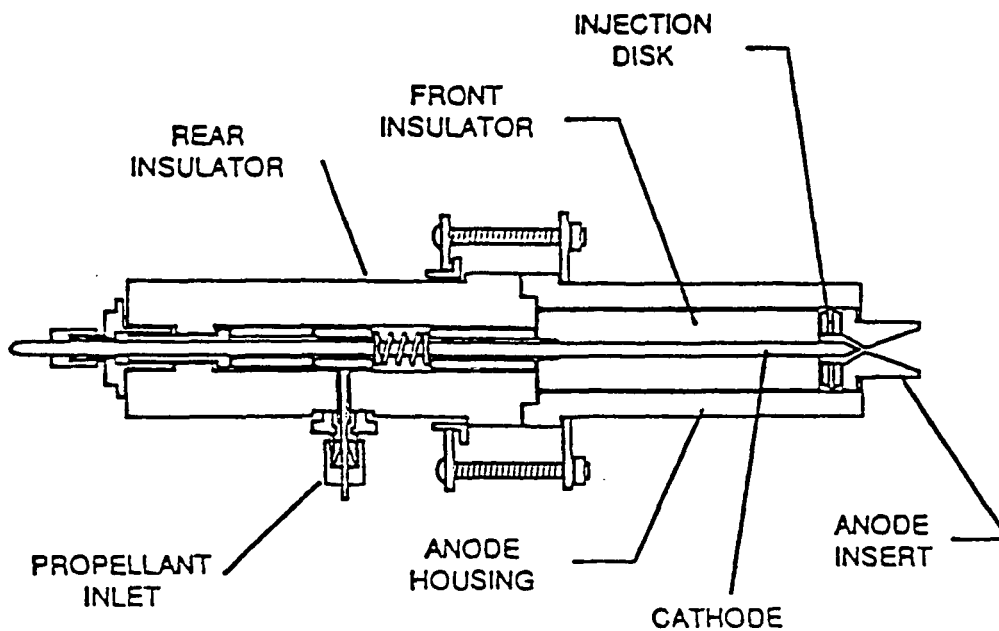
Fig. 1.1 Cutaway view of an arcjet thruster (Source: [4])

Because of lack of sufficient space electric power (such as solar panels) and forseeable near term applications, work on the thruster was temporarily abandoned in the 1960's. However, new space mission requirements along with major advances in power electronics technology over the last two decades have caused a dramatic revival of interest in the arcjet thruster [2]. The primary interest in arcjet thrusters stems from the fact that they are up to two times more efficient than present chemical engines and resistojet technologies [3]. The resultant savings can be used to realize: 1) increased satellite lifetime, 2) larger satellite payloads, 3) use of a smaller rocket booster, or any combination of these [3]. Currently, thrusters of various power levels are being researched primarily for prime propulsion and North-South/East-West stationkeeping of geosynchronous satellites [1, 2, 4, & 5].

The standard output of a satellite solar panel is approximately 30 volts DC, while the arcjet thruster requires an operating voltage greater than or equal to 100 volts DC, and an operating current of approximately 10 amps DC. It is therefore obvious that a DC to DC converter will be required by this system. The converter will also serve to limit the following: 1) arcjet voltage fluctuations caused by variations in the solar panel output voltage (voltage regulation); 2) solar panel output voltage fluctuations caused by variations in the arcjet voltage (input/output isolation). Further details concerning converter design can be found elsewhere [2, 4].

It has been shown that the arcjet thruster has a static volt-ampere (I-V) characteristic which exhibits a decrease in voltage with increasing current (negative resistance slope) over the practical operating range [4]. The static volt-ampere characteristics of an arcjet thruster for various gas flow rates is shown in Fig. 1.2.

Once the required converter has been assembled, it must be tested to see if it will perform as desired. By connecting resistors to the converter output, resistive load test can
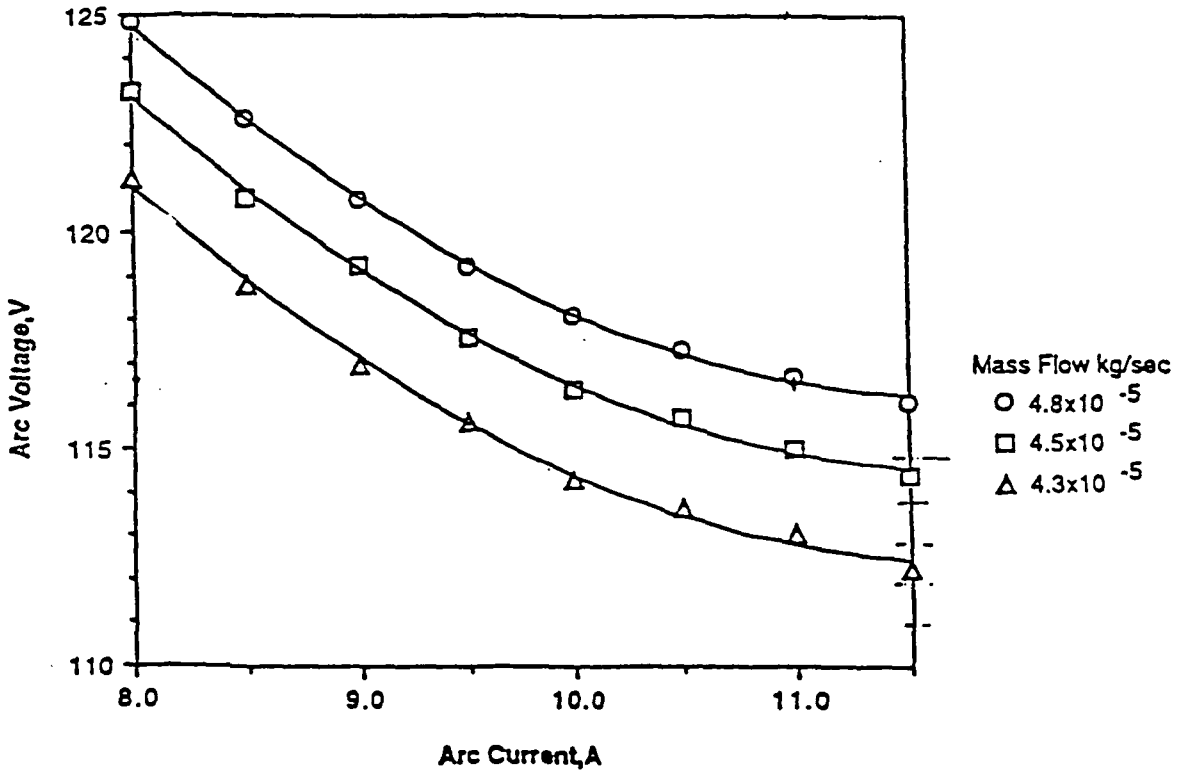
Fig. 1.2 Static Volt/Ampere characteristics for various flow rates (Source: [4])

be performed to determine load and line current regulation, load transient response, output ripple and power efficiency [2, 5]. The resistive load tests provide helpful information needed to evaluate converter performance. However, they provide no indication as to whether the converter will be stable when connected to a load device which has the negative resistance I-V characteristic shown in Fig. 1.2.

One of two methods can be used to indicate whether the converter will be stable when operating with a negative resistance load. The converter can be tested either by using the actual load device, or by using a device which simulates the I-V characteristics

of the actual load.

Using the actual load device for converter testing has several drawbacks. First of all, the converter designer may not have access to the necessary equipment required for arcjet thruster operation, such as a vacuum chamber, fuel (or propellant), or even the thruster itself. Acquisition of the necessary fixtures and equipment would be time consuming as well as expensive. It might be possible to test the converter at a facility which has access to the required equipment, but this to can be costly and time consuming as, the nearest facility could be hundreds of miles away. Test complexity can also present a problem as the designer must become familiar with the necessary procedures required when operating a thruster, such as vacuum chamber operation, proper fuel mixtures and flow rates, and arc establishment criteria.

By using an electronic load which simulates the I-V characteristics of an arcjet thruster, all of the problems mentioned above can be eliminated.

1.2 OBJECTIVE

This study considers the development of an electronic load (hereafter referred to as a simulator) which has an I-V load characteristic similar to that of the arcjet thruster, shown in Fig. 1.2. The simulator was constructed in the laboratory using relatively inexpensive power electronics components. To avoid unnecessary labwork in future applications, care was taken so that the simulator adequately resembled the load and was free of internal instabilities. After construction and successful operation, the simulator was then used to provide an experimental demonstration of the stability of various arcjet supply arrangements.

To evaluate simulator performance, the simulator was tested with an actual current mode controlled (CMC) converter designed for a 1 kilowatt arcjet thruster. Upon successful operation with the simulator, the converter was then tested on an actual arcjet thruster at the NASA Lewis Research Center in Cleveland, Ohio, after which, the static and dynamic load responses of the simulator and thruster testing were compared.

In addition, methods of varying the simulator dynamic impedance so that it could be made to more closely resemble that of an arcjet thruster, were also explored. Finally, possible simulator applications with other arc producing devices (such as in welding) were investigated.

Chapter 2

SIMULATOR DEVELOPMENT

2.1   CIRCUIT DEVELOPMENT

2.1.1 Introduction

Upon further examination of Fig. 1.2, it can be seen that the static I-V load characteristic of an arcjet thruster is similar to that of a constant-power (IV=k, where k is a constant) curve. The dynamic impedance data from [4] also suggest that the arcjet has a load characteristic similar to IV=k for frequencies up to about 60 kHz. Therefore, if the simulator is constructed in such a way that it produces a constant-power I-V load characteristic, it will then have an I-V load charcteristic similar to that of an arcjet thruster. This leads to the development of the two-loop feedback system shown in Fig. 2.1.

Examination of Fig. 1.2 reveals that the large signal, steady state operation of an arcjet can be described by the function:

$$v = f_A (i)$$

Since for large signal, steady state operation the compensation capacitor (C_a) of Fig. 2.1 will block current flow through its path, the multiplier output voltage (v_a) must equal the reference voltage (v_{ref}). Thus,

$$v_{ref} = v_a$$

where for the particular multiplier used (MC1494L) it can be shown that v_a of Fig. 2.1 is given by:

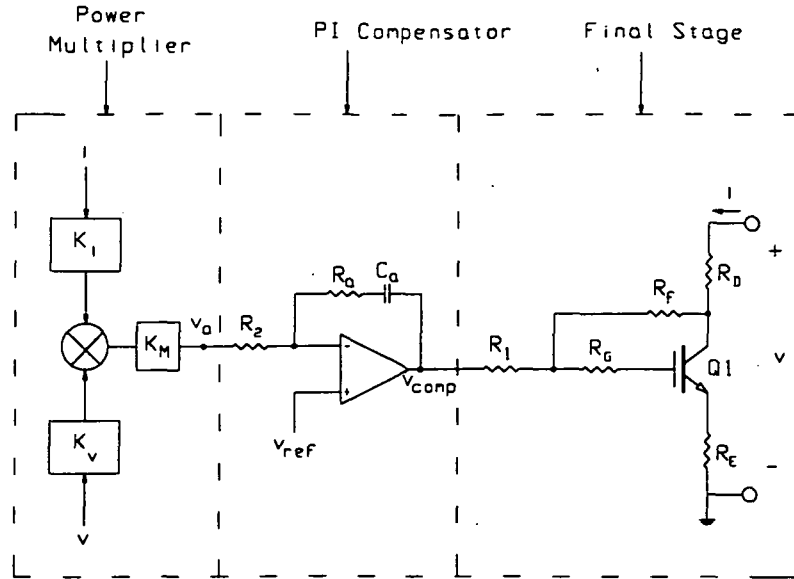$$v_a = k_1 + k_2 \cdot i + k_3 \cdot v + k_i \cdot k_v \cdot k_M \cdot i \cdot v = v_{ref} \qquad (2.1a)$$

6

Fig. 2.1 Initial cicuit design

Rearrangement of (2.1a) yields:

$$v = f_S(i) = \frac{v_{ref} - k_1 - k_2 \cdot i}{k_3 + k_T \cdot i} \quad where \quad k_T = k_i \cdot k_v \cdot k_M \qquad (2.1b)$$

Originally k_1, k_2 and k_3 were set to zero, such that the large signal, steady state operation of Fig. 2.1 would be determined from,

$$v = f_S(i) = \frac{v_{ref}}{k_T \cdot i} \qquad (2.2a)$$

or,

$$i \cdot v = k \quad where \quad k = \frac{v_{ref}}{k_T} \qquad (2.2b)$$

as desired.

The circuit in Fig. 2.1 can be subdivided into the following three parts: 1) the power multiplier, 2) the PI compensator, and 3) the final stage.

2.1.2 The Power Multiplier

The purpose of the power multiplier is to produce a constant power I-V

characteristic at the terminals of the final stage by multiplying a sense of the final stage voltage by a sense of the final stage current, and providing this signal as an input to the PI compensator.

2.1.3 The PI Compensator

The purpose of the PI compensator is to provide enough gain such that sufficient simulator bandwidth is achieved, while at the same time providing a means of compensation to aid in stabilizing this two-loop feedback system.

2.1.4 The Final Stage

The desired I-V characteristics should be produced at the terminals of the final stage when they are connected to an appropriate arcjet power supply. Almost all of the power dissipated by the simulator (1 kW for this design) will be dissipated by the final stage. Therefore, it will be necessary to parallel several transistors when constructing the final stage transistor (Q1) of Fig. 2.1, in order to keep from exceeding specified device ratings on current, power, and operating temperature. The emitter resistance (R_E) is used to ensure that the final stage transistor current divides equally among each of the paralleled transistors.

The dissipative resistance (R_D) is used to reduce the amount of power dissipation in the final stage transistor by an amount equal to $i^2 \cdot R_D$, thereby allowing the use of fewer transistors and a smaller heat sink. For this design i will be approximately 10 A. Therefore, a relatively low value of R_D will provide sufficient power reduction in the final stage transistor. It should be noted that the final stage can be incrementally approximated by a current-dependent voltage source in series with R_D (see Fig. 2.2). From simple voltage division it can be seen that:
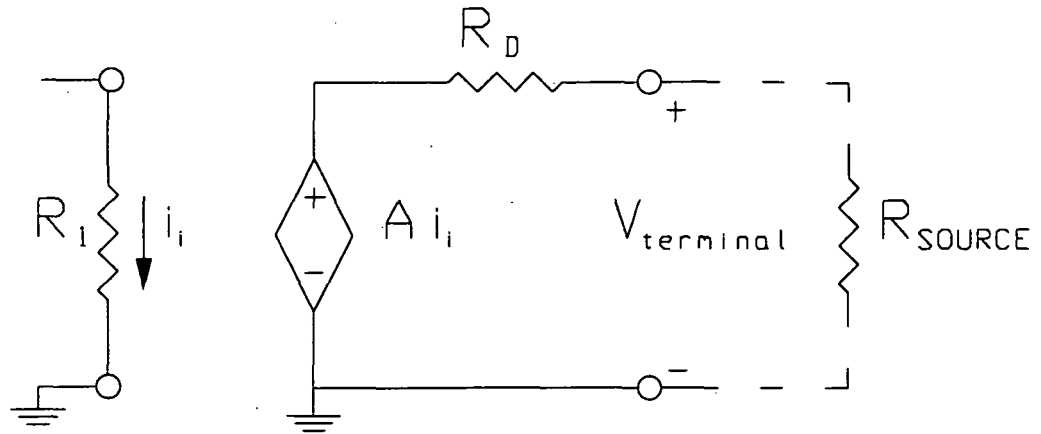
Fig. 2.2 Approximate final stage midband incremental circuit

$$V_{terminal} = A \cdot i_i \left(\frac{R_{SOURCE}}{R_{SOURCE} + R_D} \right) \qquad (2.3)$$

where R_{SOURCE} represents the internal impedance of the arcjet power supply connected at the final stage terminals. Therefore, as long as $R_D \ll R_{SOURCE}$ then $V_{terminal} \approx A \cdot i_i$ for all R_{SOURCE}. Thus, the low value of R_D also aids in producing a simulator terminal response that is independent of the impedance of the arcjet power supply.

The final stage transistor was constructed from Insulated Gate Bipolar Transistors (IGBT's). Reasons for choosing IGBT's include simplicity of gate drive, low thermal resistance per unit cost, and high power handling capabilities. Gate resistors (R_G) were connected to the gates of each IGBT to prevent parasitic oscillations in the paralleled transistors, as described in [6].

As will be seen shortly, the feedback resistance (R_f) transforms the final stage into a transresistance amplifier, converting it to the current-dependent voltage source mentioned above. The resistance R_1 was added to form the current drive for the transresistance amplifier.

2.2 THE FINAL CIRCUIT

The final working version of the simulator is shown in Fig. 2.3. Each R_E was chosen to be 4.7 Ω to ensure equal current division among the 16 IGBT's and to provide a sufficient current sense signal to the current sense amplifier (OP-27). The input voltage range of the multiplier (MC1494L) is ±10 V. As a result the voltage divider and the OP-27 are arranged such that the simulator output voltage and current can go as high as 200 V and 20 A, respectively, before the multiplier inputs are overloaded. As described in [7], the power multiplier was assembled and its offsets adjusted to zero (thereby setting k_1, k_2 and k_3 of (2.1) to zero), such that its output voltage (v_a) would be given by:

$$v_a = -k_M \cdot V_x \cdot V_y$$

where k_M (the multiplier gain) is determined from:

$$k_M = \frac{2 \cdot R_L}{R_x \cdot R_y \cdot I_1} \qquad \text{(from [7] } I_1 \approx 0.5 \text{ mA)}$$

Substituting R_L=120 KΩ, R_x=30 KΩ, R_y=62 KΩ, and I_1=0.5 mA gives:

$$k_M = 0.258$$

This value of k_M will ensure a multiplier output voltage (v_a) within the output voltage range of ±10 V.

At midband, the feedback resistance (R_f) transforms the final stage into a transresistance amplifier, converting it into the current-dependent voltage source mentioned in section 2.1.4. This can be deduced from a two port network, midband analysis upon the small signal equivalent circuit of the final stage, as shown in Fig. 2.4, where again R_{SOURCE} represents the internal impedance of the arcjet power supply connected at the final stage terminals. For the reduced circuit of Fig. 2.4(b) it can be easily shown that the impedances (Z_1) and (Z_2), and the gain $\left(\dfrac{v_c}{i_1}\right)$ are given by:
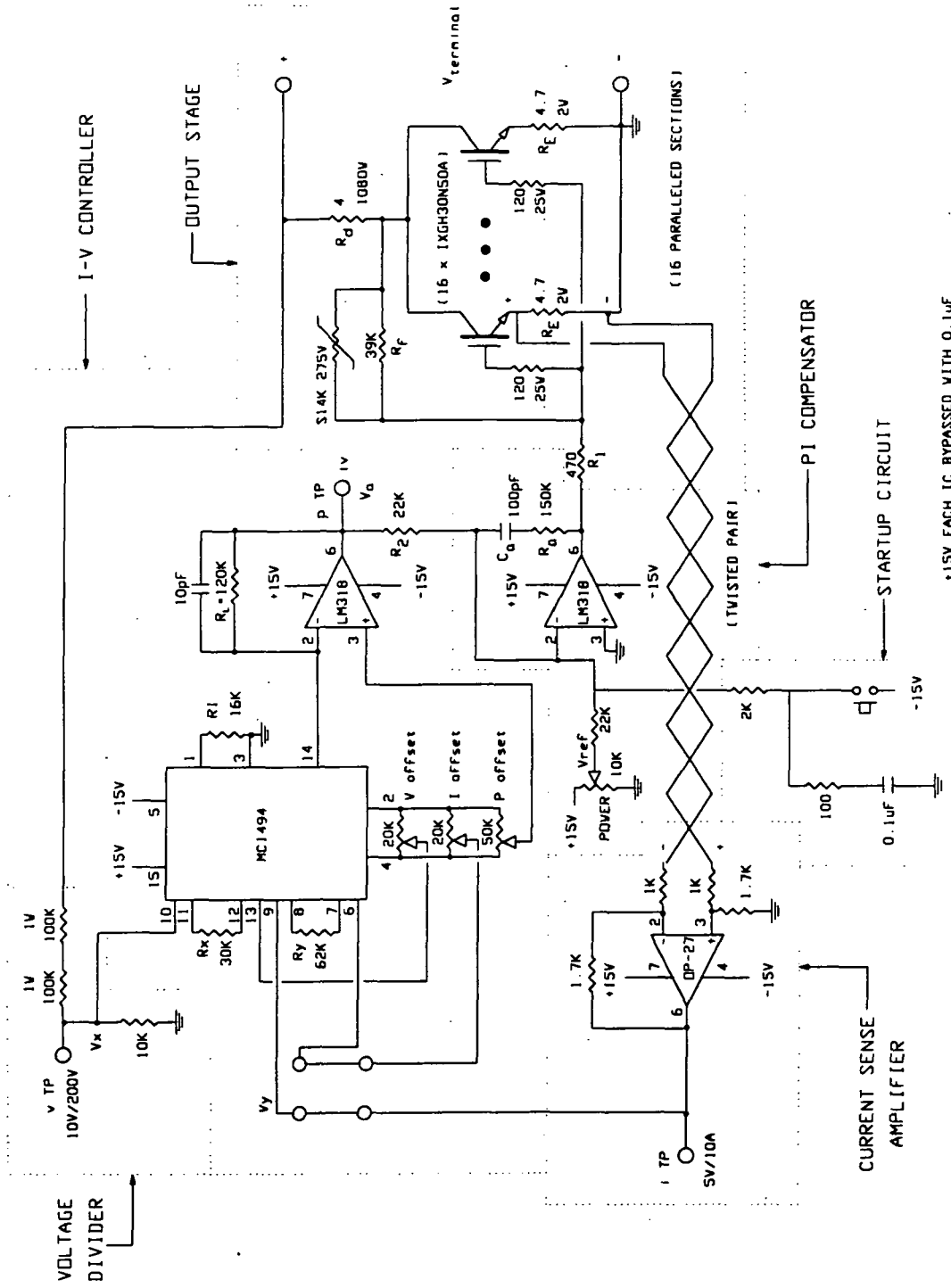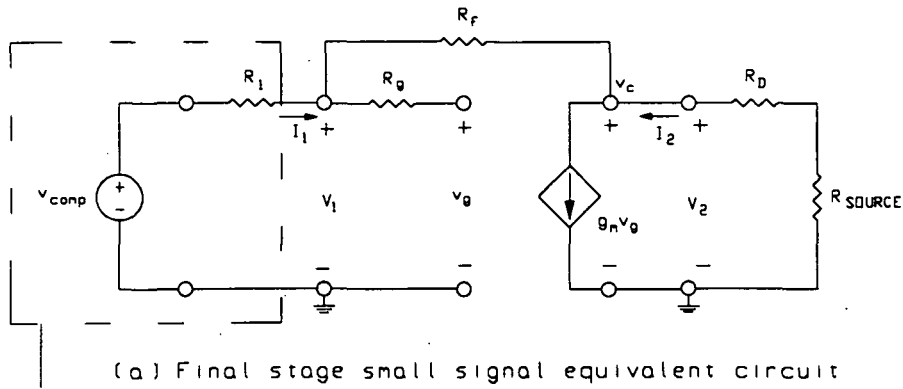
Fig. 2.3 Final simulator circuit

(a) Final stage small signal equivalent circuit

$$y_{11} = \frac{I_1}{V_1}\bigg|_{V_2=0} = \frac{1}{R_f}$$

$$y_{12} = \frac{I_1}{V_2}\bigg|_{V_1=0} = -\frac{1}{R_f}$$

$$y_{21} = \frac{I_2}{V_1}\bigg|_{V_2=0} = -\frac{1}{R_f}$$

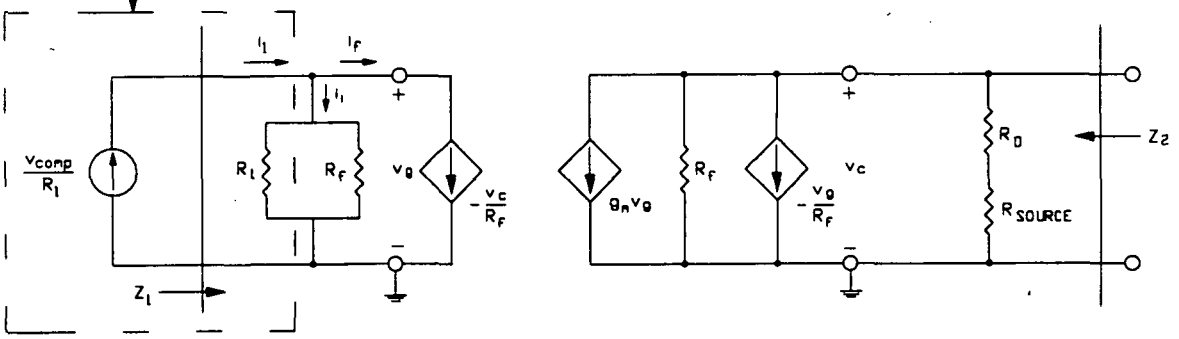$$y_{22} = \frac{I_2}{V_2}\bigg|_{V_1=0} = \frac{1}{R_f}$$

(b) Reduced final stage small signal equivalent obtained from two port network analysis

Fig. 2.4 Two port network reduction of the final stage

$$Z_1 = \frac{R_1 || R_f}{1 + A \cdot \beta} \qquad (2.4)$$

$$Z_2 = \frac{R_f || R_L}{1 + A \cdot \beta} \qquad (2.5)$$

$$\frac{v_c}{i_1} = \frac{A}{1 + A \cdot \beta} \qquad (2.6)$$

where:

$$R_L = R_D + R_{SOURCE}$$

$$A = -\left(g_m - \frac{1}{R_f}\right)\left(R_f || R_L\right)\left(R_f || R_1\right) \qquad (2.7)$$

$$\beta = -\frac{1}{R_f} \qquad (2.8)$$

Since $R_f \gg R_1$, and usually $g_m \gg R_f^{-1}$, $R_f \gg R_L$ then (2.7) can be approximated as:

$$A \approx -g_m \cdot R_L \cdot R_1 \qquad (2.9)$$

If the final stage component values are adjusted such that $A \cdot \beta \gg 1$, then (2.6) can be reduced to:

$$\frac{v_c}{i_1} \approx \frac{1}{\beta} = -R_f \qquad (2.10)$$

Substituting $\frac{v_{comp}}{R_1}$ for i_1 gives:

$$\frac{v_c}{v_{comp}} \approx -\frac{R_f}{R_1} \qquad (2.11)$$

Thus, by using R_f to transform the final stage into a transresistance amplifier, the transfer function of the final stage can be made relatively independent of uncontrollable parameters which change with output loading (specifically g_m and R_{SOURCE}). This will help to produce a simulator behavior which is independent of the arcjet supply converter's internal impedance, and aid in stabilizing this two-loop feedback system.

From (2.8) and (2.9), it can be seen that lower values of R_f will result in higher values of $A \cdot \beta$ (thus increasing the validity of (2.11)). But from (2.11) it can be seen that

lower values of R_f will also reduce the magnitude of the final stage transfer function. This can be compensated for by reducing R_1 by the same percentage as R_f, thereby keeping the transfer function magnitude constant. Since $i_1 = \dfrac{v_{comp}}{R_1}$, and the current i_1 is supplied by an LM318 op amp, the minimum value of R_1 will be determined by the output current capabilities of the LM318. For this design, R_1 was set to 470 Ω, the minimum allowable value which did not exceed the output current capabilities of the LM318. R_f was in turn set to 39 kΩ, which was high enough to provide sufficient gain for the amplifier, but still low enough to ensure that $A \cdot \beta \gg 1$.

R_D was chosen to be 4 Ω in order to relieve the power dissipation of the final stage transistor by approximately 40%, at an operating point corresponding to a simulator voltage of 100 V and current of 10 A, which is the expected operating point of an actual 1 kW arcjet thruster. It was also found that a gate resistance of 120 Ω was sufficient to prevent parasitic oscillations in the paralled transistors.

The compensator values were chosen by examining the open loop gain of the simulator. Referring to Fig. 2.1, the gain of the compensator is,

$$A_{comp}(s) = -\frac{1 + s \cdot R_a \cdot C_a}{s \cdot R_2 \cdot C_a} = \frac{v_{comp}}{v_a} \qquad (2.12)$$

and, with k_1, k_2 and k_3 of (2.1a) equal to zero, the multiplier output volatge is given by:

$$v_a = f(i, v) = k_T \cdot i \cdot v \qquad where \quad k_T = k_M \cdot k_i \cdot k_v$$

However, for the circuit arrangement of Fig. 2.3, the multiplier output voltage (v_a) will be negative. Therefore, for the final working version of the simulator, the multiplier output voltage is given by:

$$v_a = f(i, v) = -k_T \cdot i \cdot v$$

Replacing v_a by the sum of its DC and incremental parts, and $k_T \cdot i \cdot v$ by its Taylor series

expansion about the operating point, yields:

$$v_a = V_a + \hat{v}_a = f\{I, V\} + \frac{\partial f}{\partial i}\bigg|_{op} \cdot \hat{i} + \frac{\partial f}{\partial v}\bigg|_{op} \cdot \hat{v} + H.O.T. \qquad (2.13)$$

Noting that $V_a = f\{I, V\}$, and assuming small incremental values so that the higher order terms (H.O.T.) of (2.13) can be neglected, yields the approximate incremental multiplier output voltage:

$$\hat{v}_a \approx - \left(k_T \cdot I \cdot \hat{v} + k_T \cdot V \cdot \hat{i} \right) \qquad (2.14)$$

To find the gain of the final stage the transistor must first be replaced with its small signal equivalent circuit. Recalling that the transistor actually consists of 16 paralleled IGBT's results in the transistor small signal equivalent circuit of Fig. 2.5(a). Using PSpice [8] to examine the AC steady state transfer function reveals that the circuit

(a) Small signal eqivalent circuit of
16 parolled IGBT's

(b) Simplified equivalent circuit
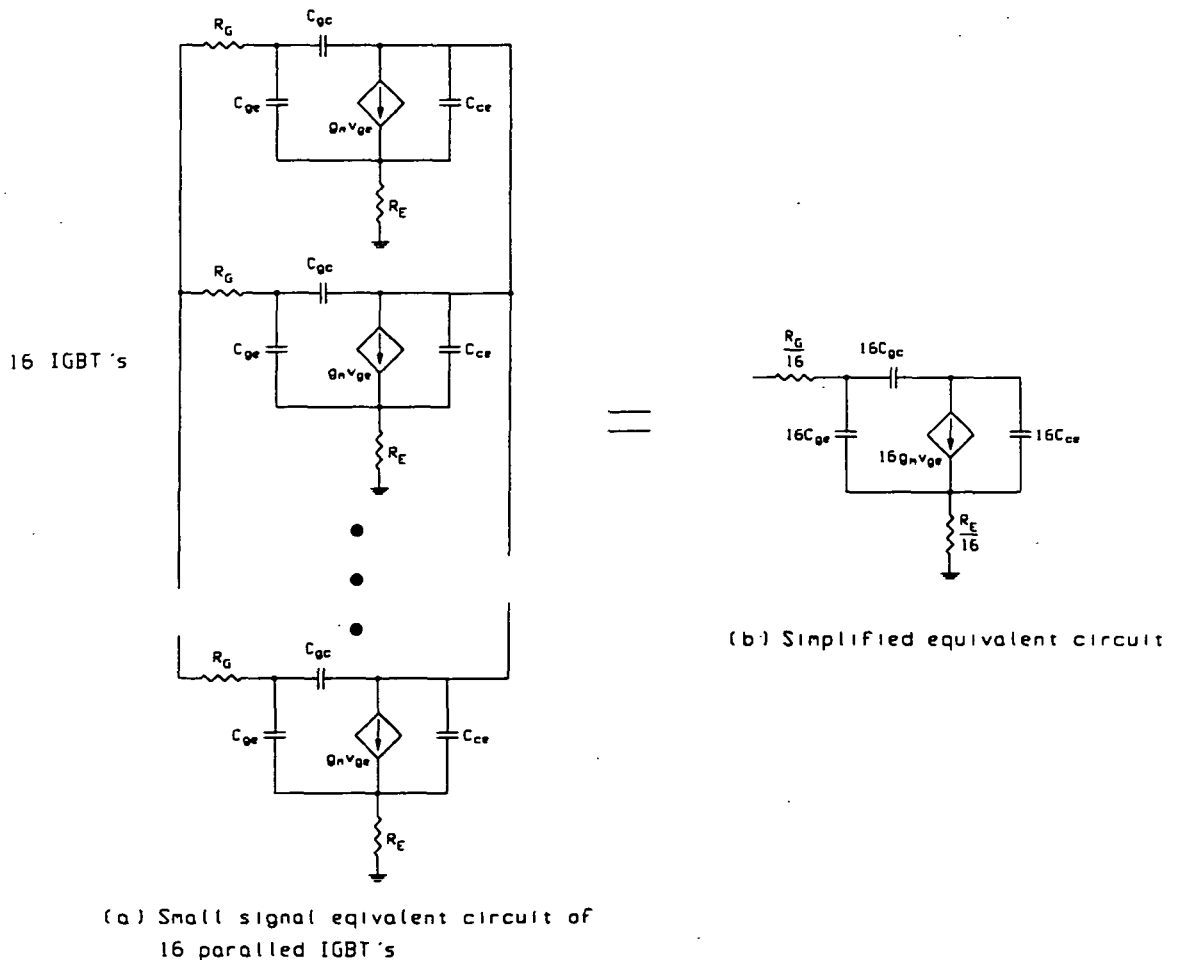
Fig. 2.5 Simplification of transistor small signal equivalent circuit

of Fig. 2.5(b) is identical to that of Fig. 2.5(a), as expected. Using the result of Fig. 2.5, the small signal equivalent circuit of the final stage can be drawn as shown in Fig. 2.6.
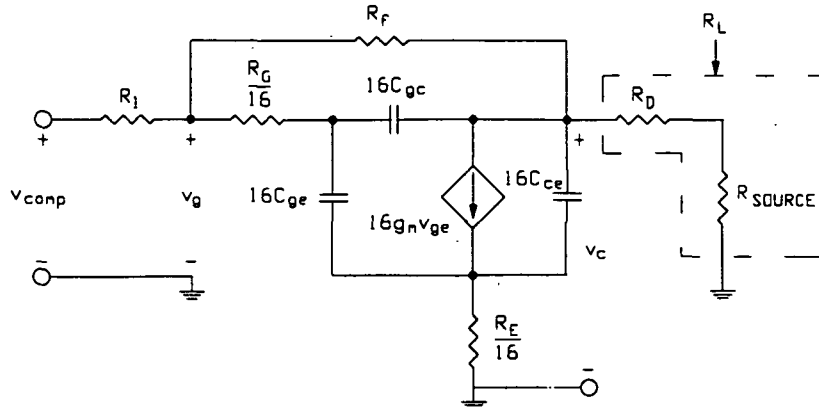

Fig. 2.6 Final stage small signal equivalent circuit

The hand analysis of this circuit is somewhat complex. However, as shown in Fig. 2.7, a PSpice [8] simulation of Fig. 2.6 shows that it has a dominant-pole frequency response for all values of R_{SOURCE} ranging from zero to infinity. (For this simulation final circuit values of R_1, R_G, R_f and R_D were used while values for C_{ge}, C_{gc}, C_{ce} and g_m were estimated from the IGBT data sheet.) Therefore, neglecting the effects of higher order poles and zeroes, a simplified circuit having a transfer function which very closely resembles that of Fig. 2.6 can be obtained. This circuit is shown in Fig. 2.8, where from hand analysis it can be shown that the midband gain (A_{mid}) and dominant high frequency pole (ω_H) are given by:

$$A_{mid} = \frac{-g_1 \cdot R_f \cdot R_L}{R_f + R_1 \cdot (1 + g_1 \cdot R_L)} = \frac{v_c}{v_{comp}} \qquad (2.15)$$

$$\omega_H = \frac{1}{\left(R_1 \mid\mid \frac{R_f}{(1 + g_1 \cdot R_L)}\right)(C \cdot (1 + g_1 \cdot R_L))} \qquad (2.16)$$
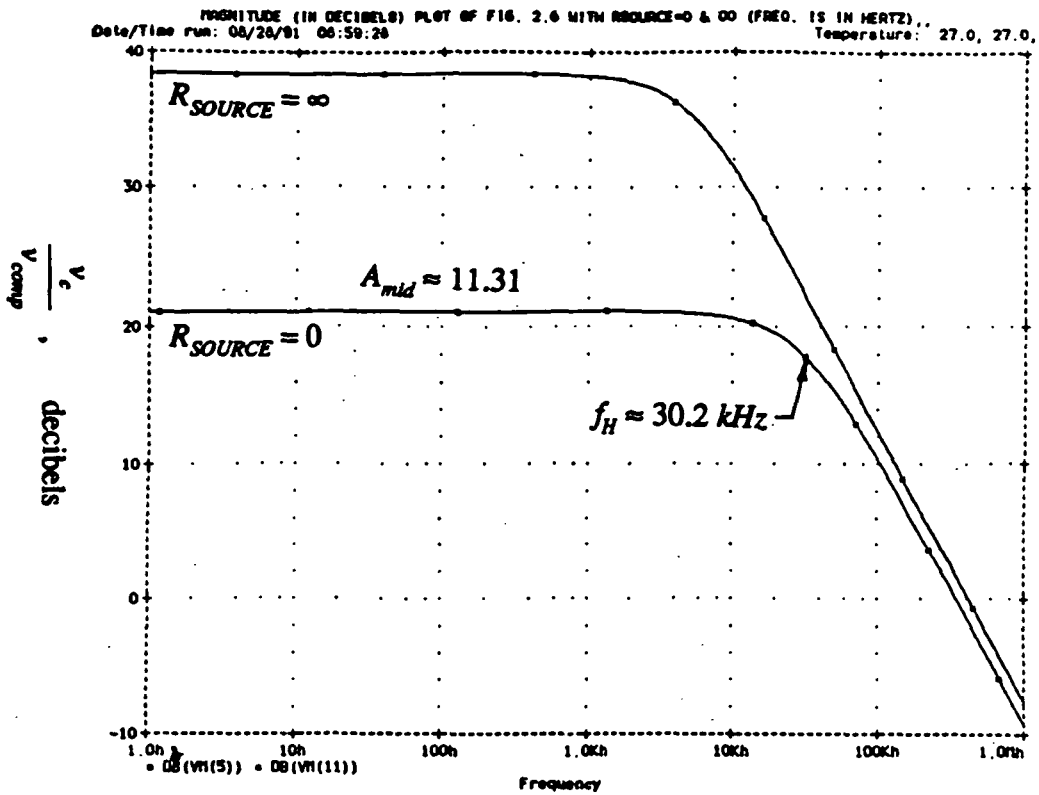
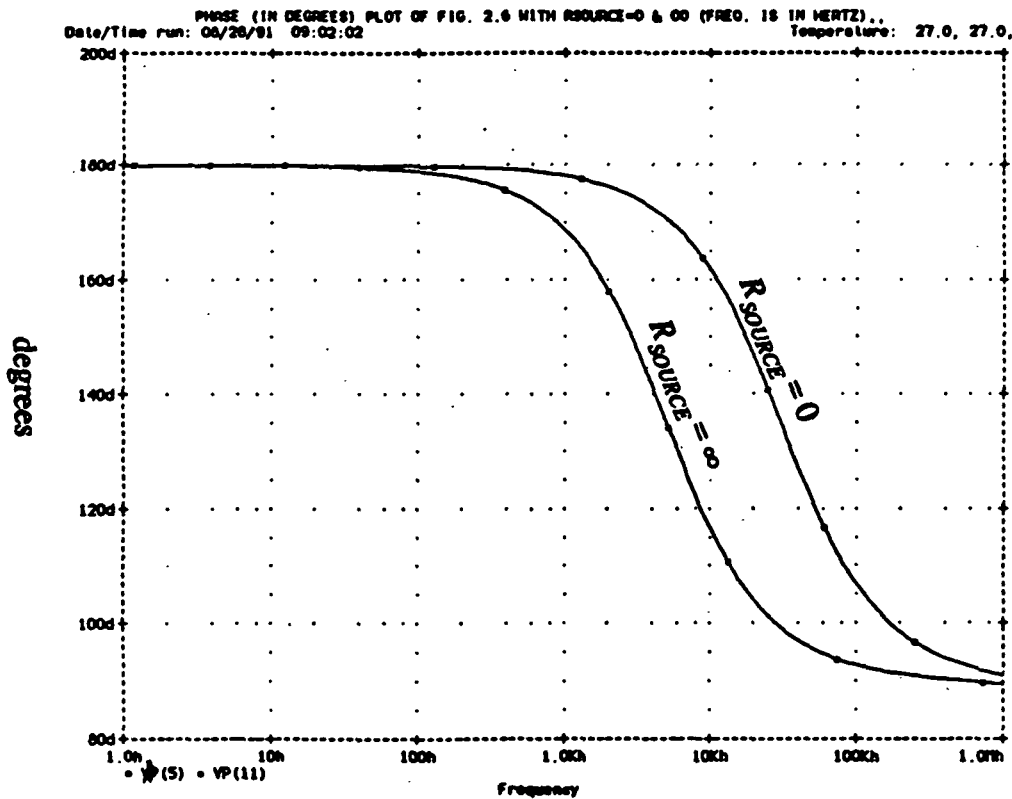Fig. 2.7(a) Pspice Bode magnitude plots of $\dfrac{v_c}{v_{comp}}$ of Fig. 2.6 for $R_{SOURCE}=0$ and ∞

Fig. 2.7(b) Pspice Bode phase plots of $\dfrac{v_c}{v_{comp}}$ of Fig. 2.6 for $R_{SOURCE}=0$ and ∞
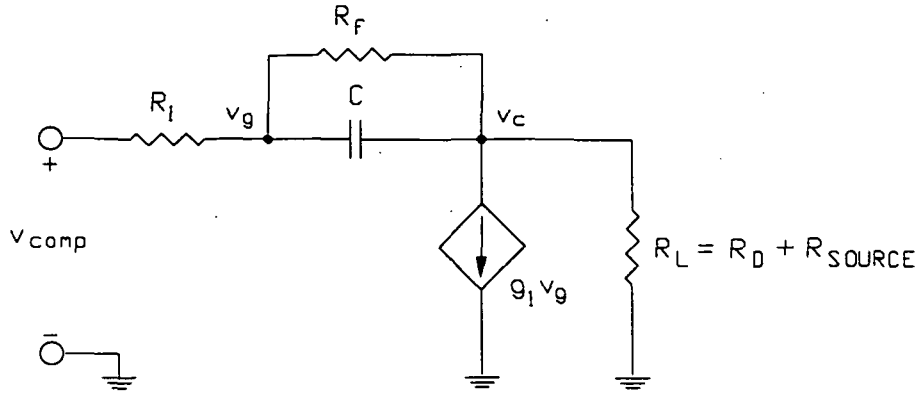
Fig. 2.8 Simplified circuit having a transfer function closely resembling that of Fig. 2.6

Usually $g_1 \cdot R_L \gg 1$ and (2.15) can be approximated as:

$$A_{mid} \approx - \frac{g_1 \cdot R_f \cdot R_L}{R_f + g_1 \cdot R_L \cdot R_1} \qquad (2.17)$$

and when R_L is large enough such that $g_1 \cdot R_L \cdot R_1 \gg R_f$ (2.17) reduces to:

$$A_{mid} \approx - \frac{R_f}{R_1} \qquad (2.18)$$

which is the same result obtained in (2.11).

Since Figs. 2.6 and 2.8 produce similar transfer functions, g_1 can be found by setting $\left| A_{mid} \right|$ of (2.15) equal to the A_{mid} of Fig. 2.7(a) for $R_{SOURCE} = 0$ $(R_L = R_D)$. Therefore:

$$g_1 = \frac{A_{mid} \cdot (R_1 + R_f)}{(R_f \cdot R_L - A_{mid} \cdot R_L \cdot R_1)} = 3.31 \ mhos \qquad (2.19)$$

Similarily, C can be found by setting ω_H of (2.16) equal to $2 \cdot \pi \cdot f_H$ of Fig. 2.7(a) for $R_{SOURCE} = 0$, giving:

$$C = \frac{1}{\left(R_1 || \frac{R_f}{(1 + g_1 \cdot R_L)} \right) \left(2 \cdot \pi \cdot f_H \cdot (1 + g_1 \cdot R_L) \right)} = 922.5 \ pF \qquad (2.20)$$

Using these values of g_1 and C along with the final circuit values of R_1, R_f and R_D, a PSpice [8] frequency response analysis of Fig. 2.8 yields the Bode plots of Fig. 2.9.
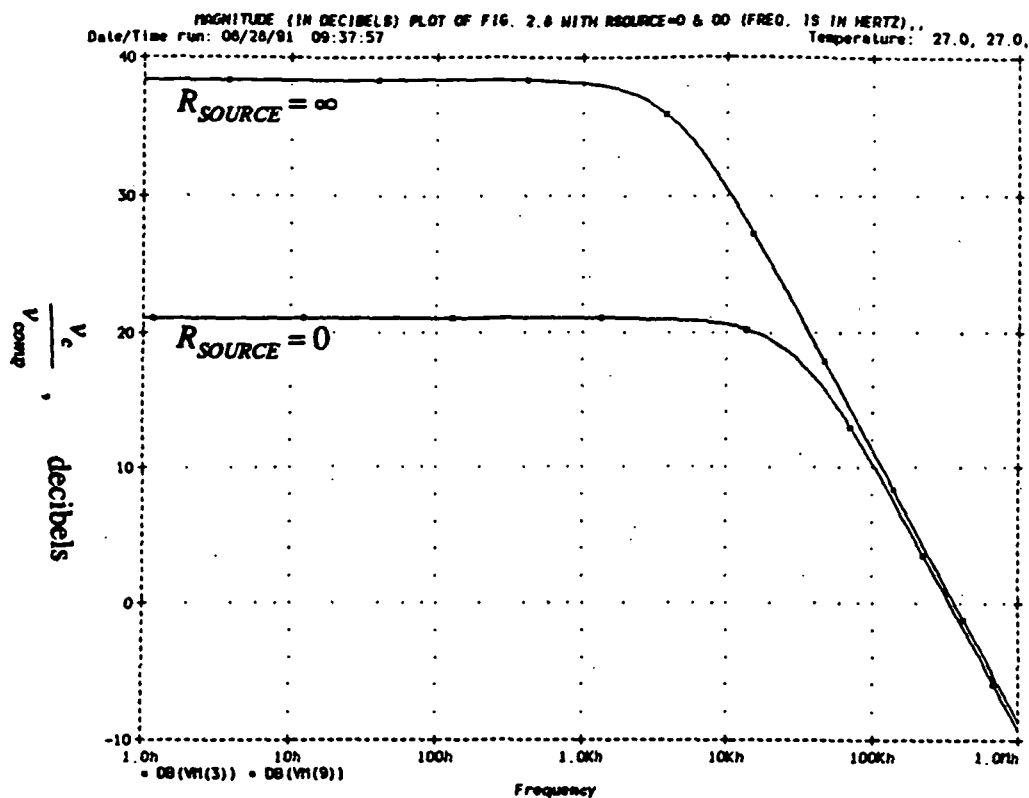
Fig. 2.9(a) Pspice Bode magnitude plots of $\dfrac{v_c}{v_{comp}}$ of Fig. 2.8 for $R_{SOURCE} = 0$ and ∞
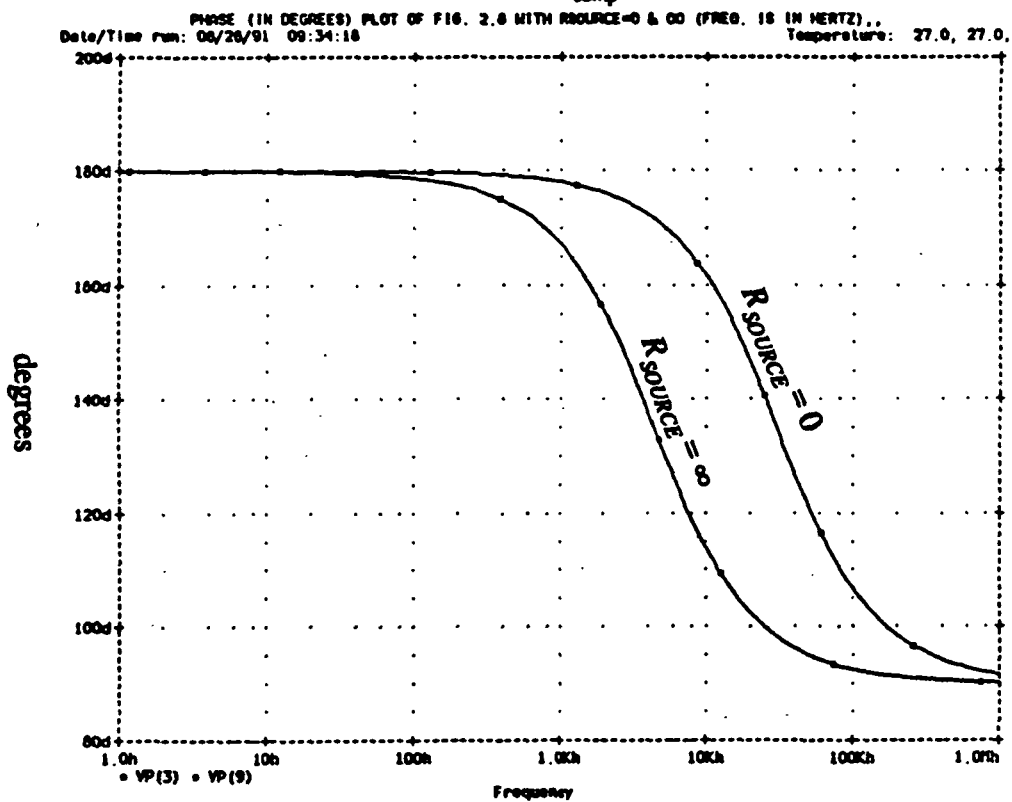

Fig. 2.9(b) Pspice Bode phase plots of $\dfrac{v_c}{v_{comp}}$ of Fig. 2.8 for $R_{SOURCE} = 0$ and ∞

Comparing Fig. 2.9 with Fig. 2.7 it can indeed be seen that the transfer functions of Figs. 2.6 and 2.8 closely resemble each other. Therefore, referring to (2.15) and (2.16), the gain of the final stage can be closely approximated as:

$$A_{fs}(s) = A_{mid} \cdot \left(\frac{1}{1 + \frac{s}{\omega_H}} \right) \qquad (2.21)$$

where as given in (2.15) A_{mid} (and therefore $A_{fs}(s)$) is a negative number.

The loop gain of the simulator can now be found by breaking the simulator circuit at a specific point, as shown in Fig. 2.10, and calculating the ratio of the output voltage to the input voltage at this point.
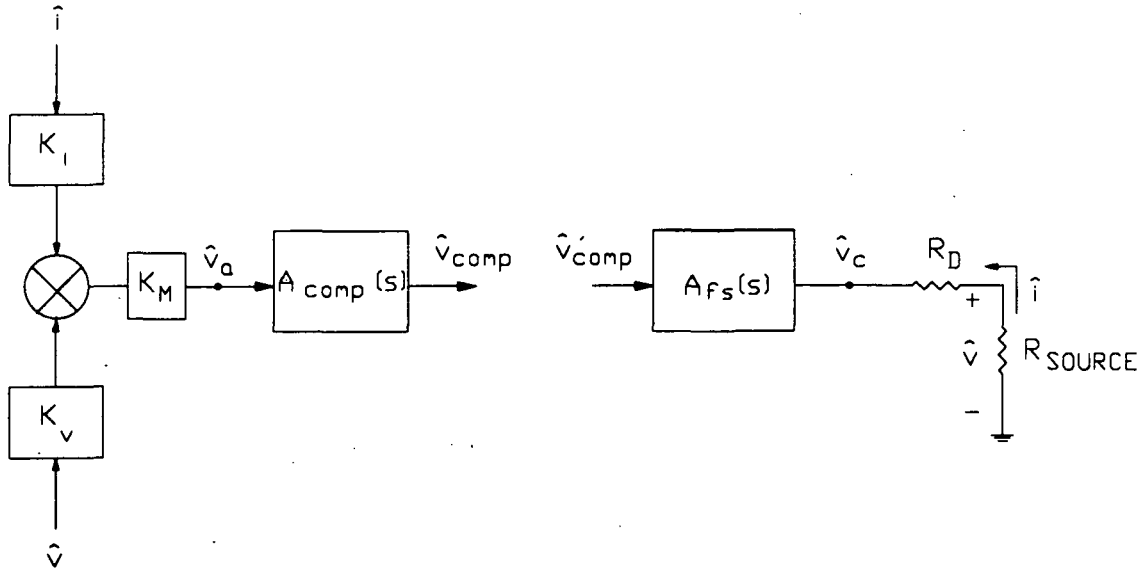

Fig. 2.10 Circuit used to calculate the simulator loop gain

From Fig. 2.10:

$$\hat{v}_c = \hat{v}_{comp} \cdot A_{fs}(s) \qquad (2.22)$$

$$\hat{v} = \hat{v}_c \cdot \frac{R_{SOURCE}}{R_D + R_{SOURCE}} = \hat{v}_{comp} \cdot A_{fs}(s) \cdot \frac{R_{SOURCE}}{R_D + R_{SOURCE}} \qquad (2.23)$$

$$\hat{i} = - \frac{\hat{v}}{R_{SOURCE}} = - \frac{\hat{v}_{comp} \cdot A_{fs}(s) \cdot \frac{R_{SOURCE}}{R_D + R_{SOURCE}}}{R_{SOURCE}} \qquad (2.24)$$

$$\hat{v}_{comp} = \hat{v}_a \cdot A_{comp}(s) \qquad (2.25)$$

Plugging (2.14) into (2.25) gives:

$$\hat{v}_{comp} = -\left(k_T \cdot I \cdot \hat{v} + k_T \cdot V \cdot \hat{i}\right) \cdot A_{comp}(s) \qquad (2.26)$$

and substitution of (2.23) and (2.24) into (2.26) gives:

$$\hat{v}_{comp} = -\left(k_T \cdot I \cdot \hat{v}_{comp} \cdot A_{fs}(s) \cdot Y - \frac{k_T \cdot V \cdot \hat{v}_{comp} \cdot A_{fs}(s) \cdot Y}{R_{SOURCE}}\right) \cdot A_{comp}(s) \qquad (2.27)$$

where,

$$Y = \frac{R_{SOURCE}}{R_D + R_{SOURCE}} \qquad (2.28)$$

Now, the loop gain can be found from:

$$LG = \frac{\hat{v}_{comp}}{\hat{v}_{comp}} = -\left(k_T \cdot I \cdot A_{fs}(s) \cdot Y - \frac{k_T \cdot V \cdot A_{fs}(s) \cdot Y}{R_{SOURCE}}\right) \cdot A_{comp}(s) \qquad (2.29)$$

Substitution of (2.28) into (2.29) and simplifying yields:

$$LG = -A_{fs}(s) \cdot A_{comp}(s) \cdot \left(\frac{k_T \cdot (I \cdot R_{SOURCE} - V)}{R_D + R_{SOURCE}}\right) \qquad (2.30)$$

From (2.30) it can be seen that the loop gain becomes positive when $I \cdot R_{SOURCE} < V$. Therefore, the following condition must be satisfied for stability:

$$R_{SOURCE} > \frac{V}{I} \qquad (2.31)$$

The result of (2.31) is entirely expected when a load device (such as the simulator) having the I-V characteristics of a constant power ($i \cdot v = k$) curve is connected to the output of an arcjet power supply having an internal impedance of R_{SOURCE}, as shown in Fig. 2.11.
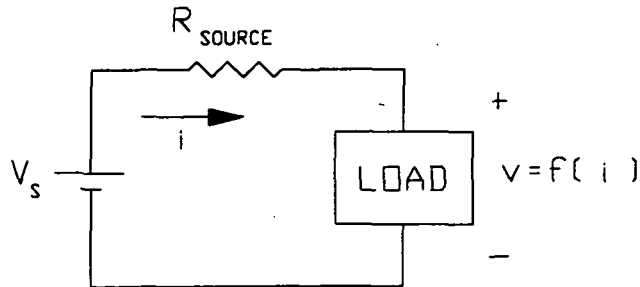

Fig. 2.11 Arcjet power supply having an internal impedance of R_{SOURCE} and its load

The incremental circuit of Fig. 2.11 is shown in Fig. 2.12 where $\hat{z}$ represents the dynamic impedance of the load which can be found from:

$$\hat{z} = \frac{\hat{v}}{\hat{i}} = \left[\frac{dv}{di}\right]_{I,V} = \left[\frac{df(i)}{di}\right]_{I,V} \qquad (2.32)$$

Note from (2.32) that $\hat{z}$ is also equivalent to the slope of the tangent to the I-V curve at the operating point (I,V).
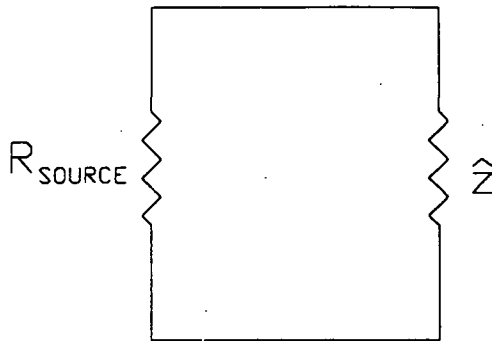

Fig. 2.12 Incremental circuit of Fig. 2.11

For stability the net resistance of Fig. 2.12 must be positive. Therefore R_{SOURCE} must be greater than the magnitude of $\hat{z}$, or:

$$R_{SOURCE} > |\hat{z}| \qquad (2.33)$$

Substitution of (2.32) into (2.33) yields:

$$R_{SOURCE} > \left| \left[\frac{df(i)}{di}\right]_{I,V} \right| \qquad (2.34)$$

which for the case of a constant power load $\left(v = f(i) = \dfrac{k}{i}\right)$ reduces to (2.31).

Returning to the simulator loop gain derivation, the substitution of (2.12) and (2.21) into (2.30) gives:

$$LG = A_{mid} \cdot \left(\frac{1}{1 + \dfrac{s}{\omega_H}}\right) \cdot \left(\frac{1 + s \cdot R_a \cdot C_a}{s \cdot R_2 \cdot C_a}\right) \cdot \left(\frac{k_T \cdot (I \cdot R_{SOURCE} - V)}{R_D + R_{SOURCE}}\right) \qquad (2.35)$$

Therefore, to increase system bandwidth the zero of the compensator was chosen such that it would cancel the pole of the final stage. In addition the $R_2 \cdot C_a$ product was made as small as possible to further increase the bandwidth. This product was chosen such that the unity-gain crossover frequency of (2.35) would provide maximum bandwidth without interference from higher order poles and zeroes of the IGBT's, op amps, and the multiplier. R_2 must also be large enough such that the output current capabilities of the LM318 are not exceeded, and small enough such that the LM318's offset currents do not interfere with simulator operation. For this design R_2 was therefore chosen to be 22 kΩ. Then C_a was chosen to be 100 pF in order to provide sufficient system bandwidth.

To choose R_a, first note from (2.16) that f_H can vary from approximately 5 kHz ($R_{SOURCE} = \infty$) to approximately 30 kHz ($R_{SOURCE} = 0$). Therefore, to cancel the final stage pole, the compensator zero should be placed somewhere in this range. As seen in Fig. 2.13, the worst case scenario occurs when $\omega_H < \dfrac{1}{R_a \cdot C_a}$. In this case, the gain falls off significantly between ω_H and $\dfrac{1}{R_a \cdot C_a}$, and the bandwidth is significantly reduced. In addition, if the 0 dB crossover should occur on the -40 dB/decade slope, the phase margin would be extremely small resulting in a conditionally stable system. To achieve desired simulator performance it is important that the simulator be free of unintended internal instabilities. Otherwise, possible internal instabilities of the simulator may be falsely interpreted as converter instabilities and much time may be wasted before the actual cause is determined and corrected. If the simulator is free of internal instabilities there will be no doubt as to the cause of any system (the converter and simulator) instabilities. Therefore, to minimize the scenario of Fig. 2.13, $\dfrac{1}{R_a \cdot C_a}$ was placed closer to the lower range of f_H (≈ 10 kHz). This results in a value of $R_a = 150$ kΩ.
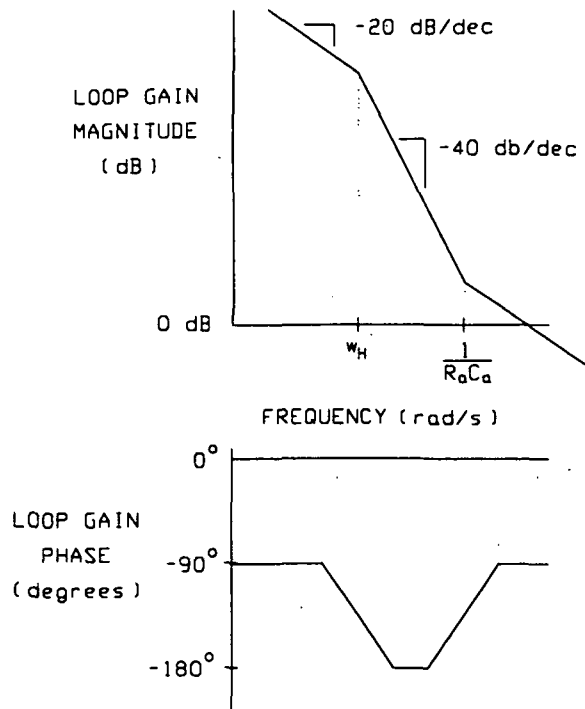
Fig. 2.13 Worst case scenario of zero placement

It should be noted that the reference voltage (v_{ref}) of Fig. 2.3 was supplied by a different method than that suggested in the initial circuit design of Fig. 2.1. Both methods, however, produce the same large signal, steady state operation equation, given by:

$$i \cdot v = \frac{v_{ref}}{k_T}$$

Thus, by adjusting the power potentiometer of Fig. 2.3 (changing v_{ref}) it is possible to shift the I-V curve from one level to another.

2.3 SIMULATOR I-V CHARACTERISTICS

Both the simulator and thruster have bifurcated I-V characteristics. The complete simulator I-V characteristic is shown in Fig. 2.14. Initially the final stage transistor will be in the off state and no current will flow in the simulator. This corresponds to an operating point along I-V charcteristic #1 in Fig. 2.14, and is a simulation of the
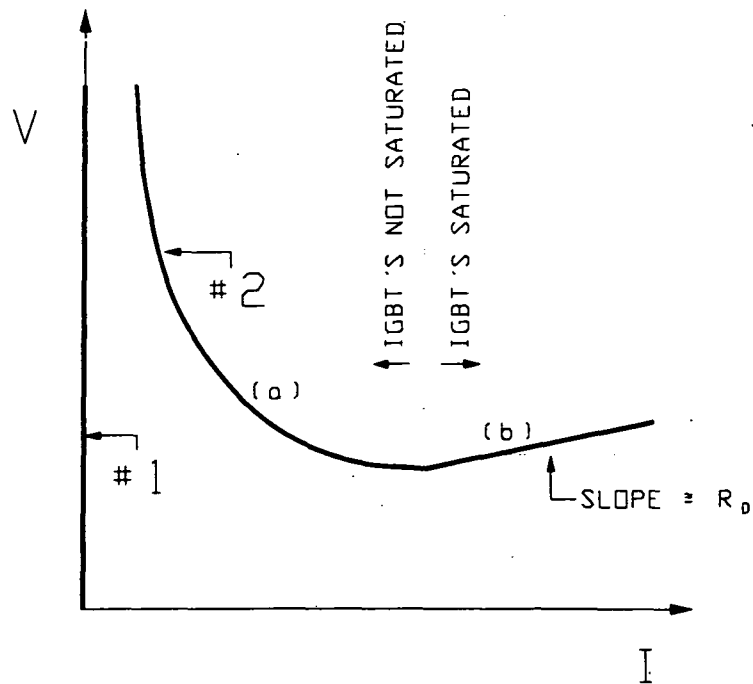
Fig. 2.14 Complete simulator I-V characteristic

thruster-off condition. The startup circuit in Fig. 2.3 was added to provide a convenient means of starting the simulator. When the startup button is pressed the final stage transistor turns on and the operating point jumps from I-V characteristic #1 to a point along I-V characteristic #2 in Fig. 2.14, thereby providing a simulation of the thruster-on condition. Instabilities of the combined arcjet supply-converter and simulator encountered during simulator operation will cause a jump from I-V characteristic #2 back to I-V characteristic #1, just as with the actual arcjet thruster.

For high enough simulator currents the IGBT's will saturate causing the collector to emitter voltage (v_{ce}) to become nearly zero. As a result, I-V characteristic #2 of Fig. 2.14 will shift from curve (a) to curve (b), which will have a slope of $\approx R_D$. Data for high current operation of the arcjet is not available. However, it is expected that for high currents the I-V characteristic of arc producing devices (such as the arcjet) will have a

positive slope, as shown in Fig. 2.15 for the case of TIG welding of aluminum [10]. This topic will be discussed further in Chapter 5. For now it is simply noted that the positively sloped portion of the I-V characteristic corresponds to current values too high for normal arcjet operation.
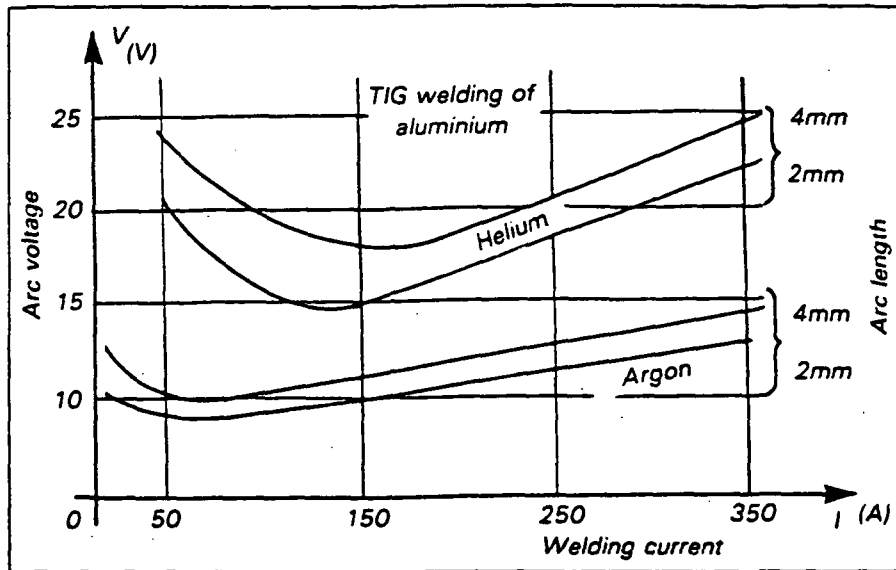

Fig. 2.15 I-V characteristics for the TIG welding of aluminum for two different arc lengths and gases (Source: [10])

2.4 STABILITY REQUIREMENTS FOR VARIOUS ARCJET POWER SUPPLY ARRANGEMENTS

As previously mentioned, the I-V characteristics of the arcjet and of the simulator are bifurcated. This bifurcated I-V characteristic is shown again in Fig. 2.16 as the bold line curves i=0 and $i \cdot v = k$. The load lines of an arcjet power supply having an internal resistance of R_{SOURCE} are also shown in Fig. 2.16 for two different values of arcjet supply output voltage. As shown for load line #1 of Fig. 2.16, if the arcjet supply output voltage is high enough, the load line of the arcjet power supply will intersect the simulator I-V characteristic at three points (points (a), (b) and (c) in Fig. 2.16). Point (c) is a stable
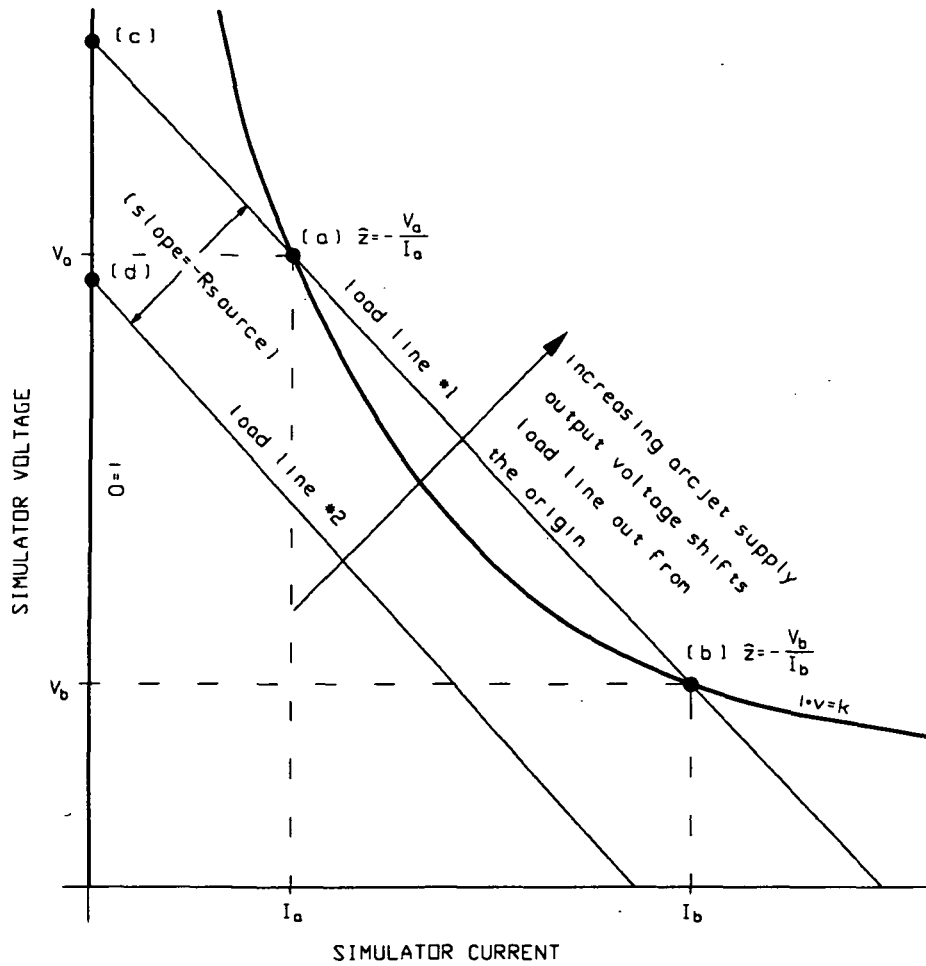
Fig. 2.16 Simulator I-V characteristic and arcjet supply load lines

operating point. It corresponds to the condition where the simulator is in its off state, thus conducting zero current and having a voltage equivalent to the arcjet power supply open circuit output voltage. The stability of points (a) and (b) can be determined by applying the stability condition of (2.34) to the respective points in Fig. 2.16.

From Fig. 2.16, note that the magnitude of the slope of the tangent to the $i \cdot v = k$ curve at point (a) ($|\hat{z}|$ at point (a)) is greater than the magnitude of the slope of the load line (R_{SOURCE}). Thus, (2.34) is not satisfied and this intersection point is unstable. However, the magnitude of the slope of the tangent to the same curve at point (b) ($|\hat{z}|$ at point (b)) is less than the magnitude of the slope of the load line (R_{SOURCE}). Thus, (2.34)

is satisfied and intersection point (b) is a stable operating point.

Therefore, for load line #1 of Fig. 2.16, (b) and (c) are both stable operating points. Which of these operating points the simulator will reach depends on the dynamics which occur after the startup button of Fig. 2.3 is pressed. Repeated testing has shown that these dynamics result in simulator operation at point (b) as long as the arcjet power supply voltage is sufficiently large such that its load line intersects the constant power curve.

As shown for load line #2 of Fig. 2.16, if the arcjet power supply voltage is not sufficiently large then the load line will intersect only with the curve i=0 at point (d). It has already been stated that this will be a stable operating point.

Thus for an arcjet power supply having an internal impedance R_{SOURCE}, it has been determined that for stable operation along the I-V curve, the slope of the load line must be steeper than the slope of the tangent to the I-V curve, at some point on the curve. This is the same as the result stated in (2.34).

The theoretical discussion of Fig. 2.16 can be demonstrated experimentally by using the test set-up shown in Fig. 2.17, where the power supply was adjusted such that the load line was close to separating from the power curve, and the peak square wave voltage was made sufficiently large to cause the load line to separate from the power curve when the square wave reached its negative value. By setting the Tektronix 11401 Digitizing Oscilloscope up for single trigger mode [9] and closing the switch of Fig. 2.17 the simulator voltage and current waveforms of Fig. 2.18 were obtained.

During time interval t_1 of Fig. 2.18, the load line corresponds to load line #1 of Fig. 2.16 and the simulator reaches its stable operating point at point (b). At the end of t_1 the rising square wave voltage causes the arcjet power supply voltage to increase thereby
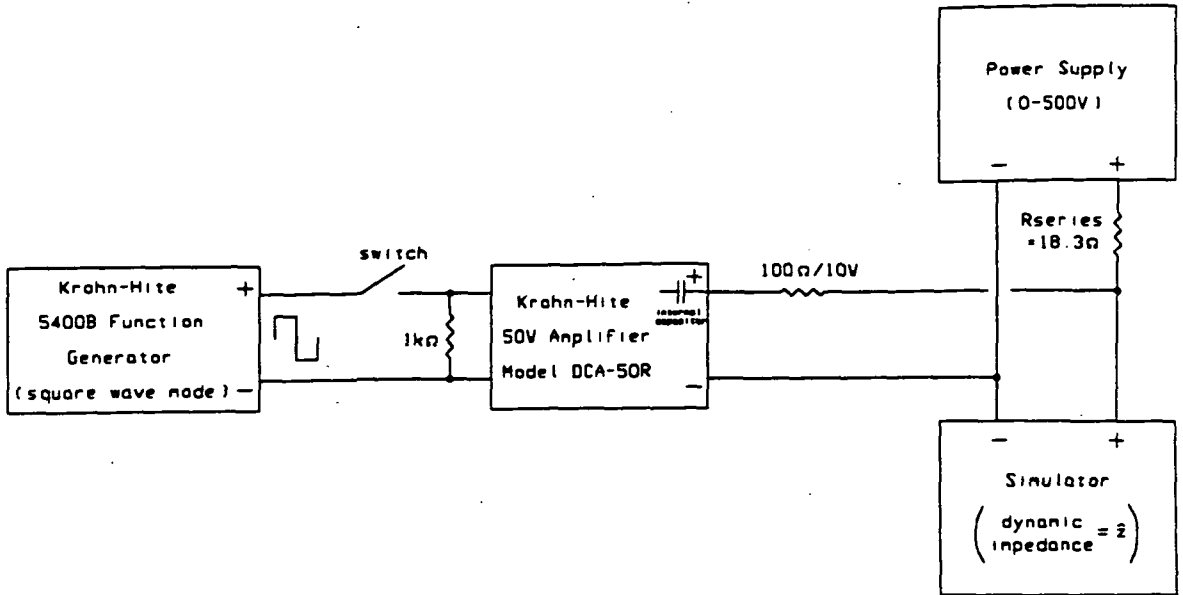
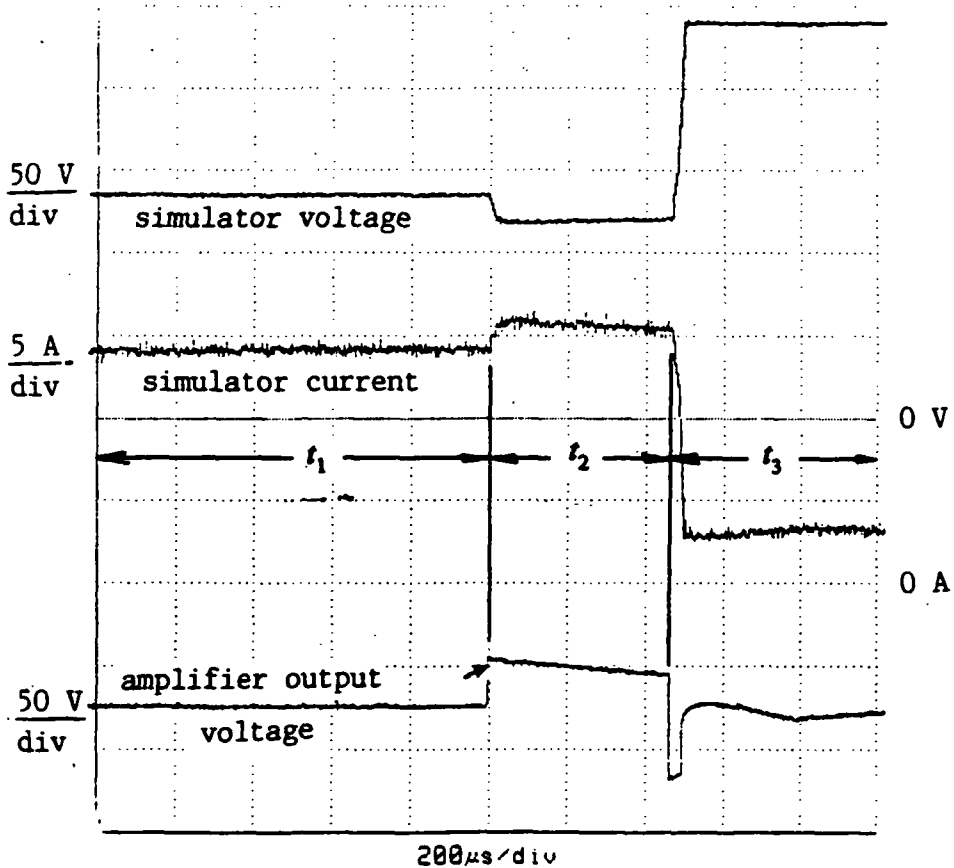Fig. 2.17 Experimental set-up used to demonstrate the effect of shifting load lines

Fig. 2.18 Simulator voltage and current waveforms obtained from the test set-up of Fig. 2.17

shifting the load line further away from the origin. Thus, the stable operating point will move down the I-V curve to the right resulting in a lower simulator voltage and a higher simulator current, as shown for time interval t_2 of Fig. 2.18. At the end of t_2 the falling square wave voltage causes the arcjet power supply voltage to decrease thereby shifting the load line to a position corresponding to load line #2 of Fig. 2.16, which is closer to the origin. Thus, the operating point moves back up the I-V curve to the left until the load line separates from the I-V curve, after which it follows the load line until it reaches its final position at point (d) in Fig. 2.11. Note that for time interval t_3 of Fig. 2.18, the current is not equal to zero. This is because of the finite time needed to charge the compensation capacitor (C_a) to its final value ($\approx$ 8 ms).

From Fig. 2.16 it can also be seen that larger values of R_{SOURCE} will result in more stable operating points since transient disturbances of the arcjet power supply would then be less likely to separate the load line from the I-V curve.

For more general cases the internal impedance $(Z(s))$ of the arcjet power supply will include some capacitance and inductance along with the resistance R_{SOURCE}. For this more general case the incremental circuit of the arcjet power supply and arcjet is shown in Fig. 2.19, where $\hat{v}_{dist}$ represents a transient disturbance voltage.
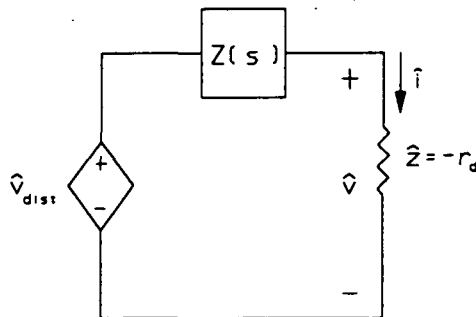

Fig. 2.19 Incremental circuit of the arcjet and arcjet power supply having a more general internal impedance of $Z(s)$

The transfer function $\left(\dfrac{\hat{v}}{\hat{v}_{dist}}\right)$ of Fig. 2.19 is given by:

$$T = \frac{\hat{v}}{\hat{v}_{dist}} = \frac{\hat{z}}{\hat{z} + Z(s)} = \frac{-r_d}{-r_d + Z(s)}$$

Therefore, if the response to the disturbance voltage $(\hat{v})$ is to die out the poles of T must be in the left-half plane. Thus, for the more general case the stability requirement can be stated as:

the zeros of $\{-r_d + Z(s)\}$ must be in the left-half plane.

Since the static I-V curves of the arcjet shown in Fig. 1.2 resemble that of Fig. 2.16, the above discussion on simulator stability also applies for arcjet operation.

Chapter 3

SIMULATOR DYNAMIC IMPEDANCE

3.1 INTRODUCTION

If the simulator is to perform as desired, its static and dynamic impedances should resemble those of an arcjet thruster as described in Hamley's paper, "Arcjet Load Characteristics" [4].

3.2 STATIC IMPEDANCE

The test set-up of Fig. 3.1 was used to obtain the static impedance data of the simulator. This was accomplished by adjusting the power supply voltage in order to obtain simulator current and voltage data for simulator currents ranging from 6 A to 15 A, at three different settings of v_{ref}.

As discussed in Chapter 2, R_{series} of Fig. 3.1 must be made large enough to ensure that the power supply load line does not separate from the simulator power curve before the static impedance data have been recorded down to 6 A. Also note that for Fig. 3.1:
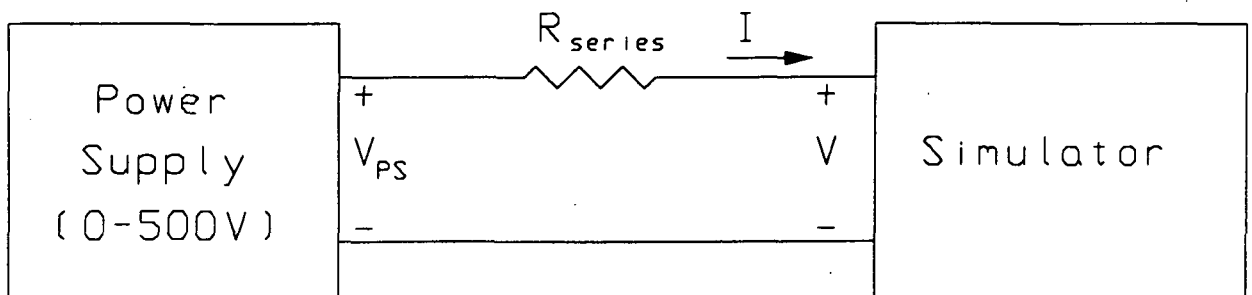
$$V_{PS} = R_{series} \cdot I + V$$

Fig. 3.1 Experimental set-up used to obtain static impedance data of the simulator

Thus, in order to record static impedance data up to I=15 A, R_{series} must be small enough such that the voltage determined by $R_{series}\cdot15$ plus the simulator voltage at I=15 A and the present setting of v_{ref} (V_{15}), does not exceed the output voltage capabilities of the power supply (500 V for this case). In other words, R_{series} must also satisfy:

$$R_{series} < \frac{V_{PS} - V_{15}}{15} = \frac{500 - V_{15}}{15}$$

By setting R_{series} to 18.3 Ω the simulator volt-ampere curves of Fig. 3.2, for several settings of v_{ref}, were obtained. For the purpose of comparison, a 1 kW constant power curve (shown in dotted lines) is also shown in Fig. 3.2.

Examination of Fig. 3.2 reveals that the curved portion of the simulator I-V characteristic does not actually follow a constant power curve as expected from the design discussion of Chapter 2. The only possible explanations for this are that either an error was made when zeroing the multiplier offsets (k_1, k_2 and k_3) of (2.1) or that some offset drift occurred between the time the offsets were adjusted to zero and the time the static impedance measurement was made. In either case, the fact that the simulator I-V curves are not constant power curves is because the offset coefficients (k_1, k_2 and k_3) of (2.1) are not all equal to zero. No steps were taken to correct this because the goal here is not to produce simulator I-V characteristics that are constant power curves, but to produce simulator I-V characteristics which are similar to those of the arcjet shown in Fig. 1.2. Comparing Fig. 1.2 with Fig. 3.2 it can be seen that this goal has been adequately accomplished. Also note that the resultant multiplier offset has actually rotated the I-V curves of Fig. 3.2 such that they resemble those of an arcjet more closely than those of a constant power curve would.

The effect of changing the power potentiometer setting (changing v_{ref}) of Fig. 2.3, is demonstrated in Fig. 3.2 as a shifting of the I-V curve towards or away from the origin.
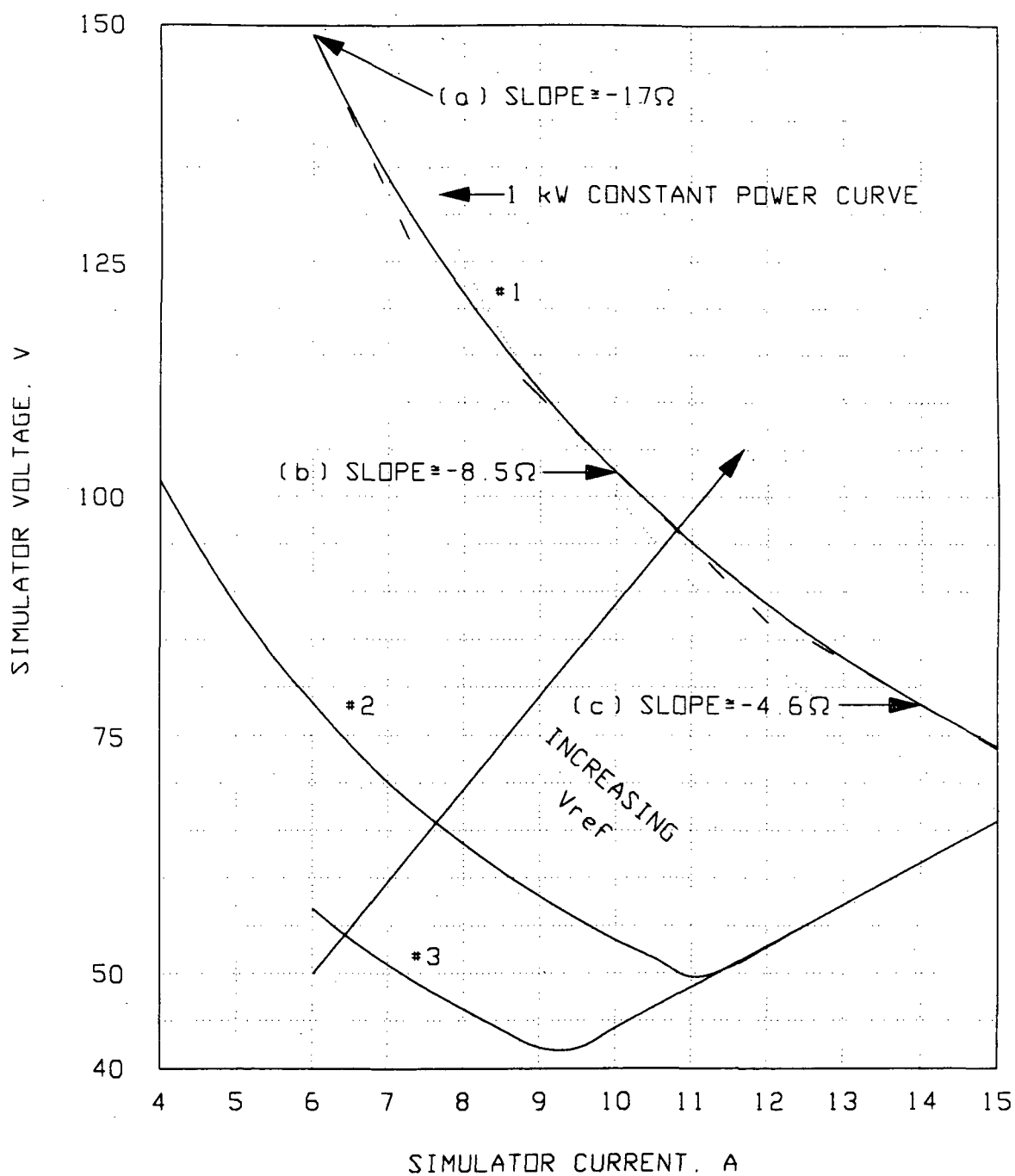
Fig. 3.2 Experimental simulator static Volt/Ampere characteristics for various settings of *Vref*

In addition, the effect of IGBT saturation is also demonstrated as a change from the I-V curve to a straight line having a positive slope of $\approx R_D$.

3.3 DYNAMIC IMPEDANCE

In his paper [4], Hamley has shown that the dynamic impedance of an actual arcjet thruster has a negative real component and no imaginary component for frequencies ranging from 100 Hz up to approximately 50 kHz. Hamley's results can be seen in Fig. 3.3 where the arcjet's upper cutoff frequency (UCF), defined here as the frequency at which the phase differs from its low frequency value by 45 degrees, appears to be approximately 40-50kHz.

The theoretical simulator dynamic impedance can be found by applying a current test source to the simulator final stage, as shown in Fig. 3.4. From Fig. 3.4 it is clear that the dynamic impedance ($\hat{z} = \frac{\hat{v}}{\hat{i}}$) can be found from,

$$\frac{\hat{v} - \hat{v}_c}{R_D} = \hat{i} \qquad (3.1)$$

where from Chapter 2,

$$\hat{v}_c = \hat{v}_a \cdot A_{comp}(s) \cdot A_{fs}(s) = -\left(k_T \cdot I \cdot \hat{v} + k_T \cdot V \cdot \hat{i}\right) \cdot X \qquad (3.2)$$

where,

$$X = A_{comp}(s) \cdot A_{fs}(s) = -\left(\frac{1 + s \cdot R_a \cdot C_a}{s \cdot R_2 \cdot C_a}\right) \cdot \left(\frac{A_{mid}}{1 + \dfrac{s}{\omega_H}}\right) \qquad (3.3)$$

and as in (2.15) and (2.16),

$$A_{mid} = \frac{-g_1 \cdot R_f \cdot R_L}{R_f + R_1 \cdot (1 + g_1 \cdot R_L)}$$

$$\omega_H = \frac{1}{\left(R_1 \| \dfrac{R_f}{(1 + g_1 \cdot R_L)}\right) \cdot (C \cdot (1 + g_1 \cdot R_L))}$$

Plugging (3.2) into (3.1) and solving for the dynamic impedance $\left(\dfrac{\hat{v}}{\hat{i}}\right)$, yields:
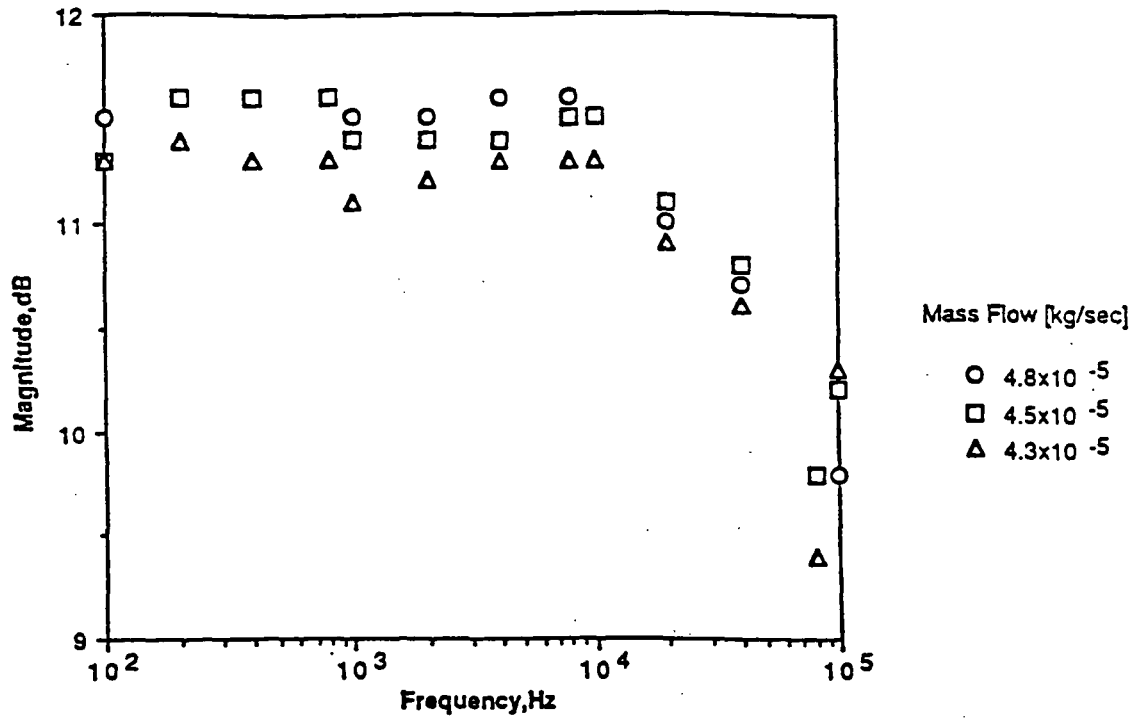
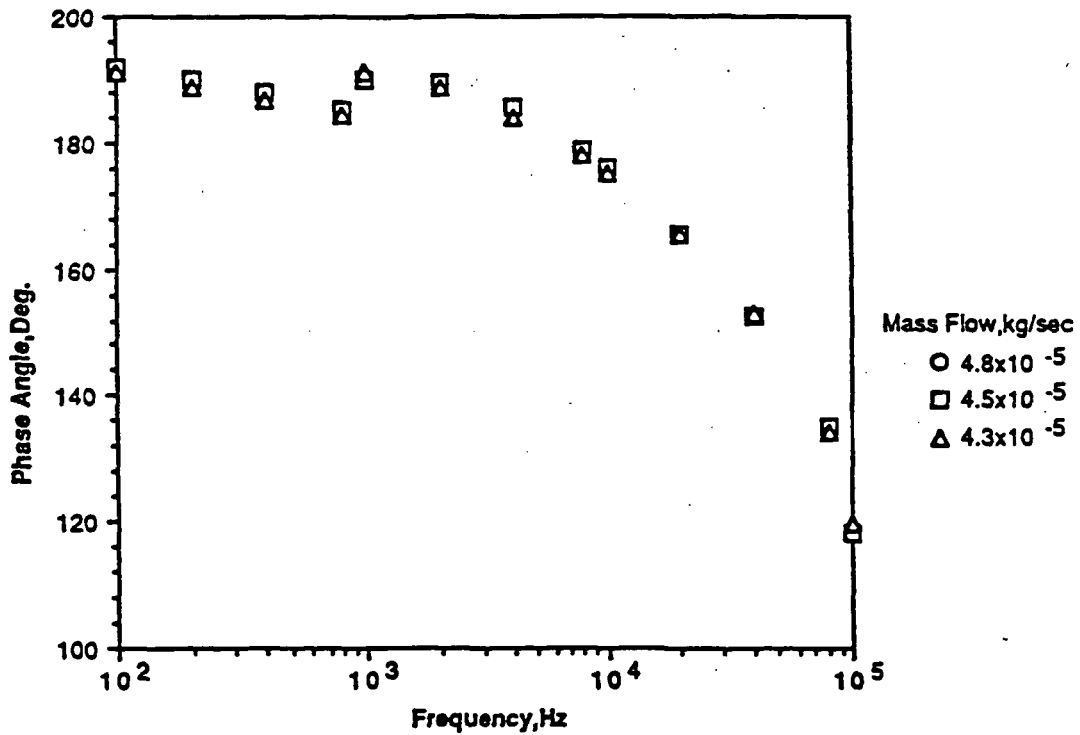Fig. 3.3(a) Dynamic impedance magnitude vs. frequency for varoius flow rates (I=10 A)

Fig. 3.3(b) Dynamic impedance phase angle vs. frequency at various flow rates (I=10 A)
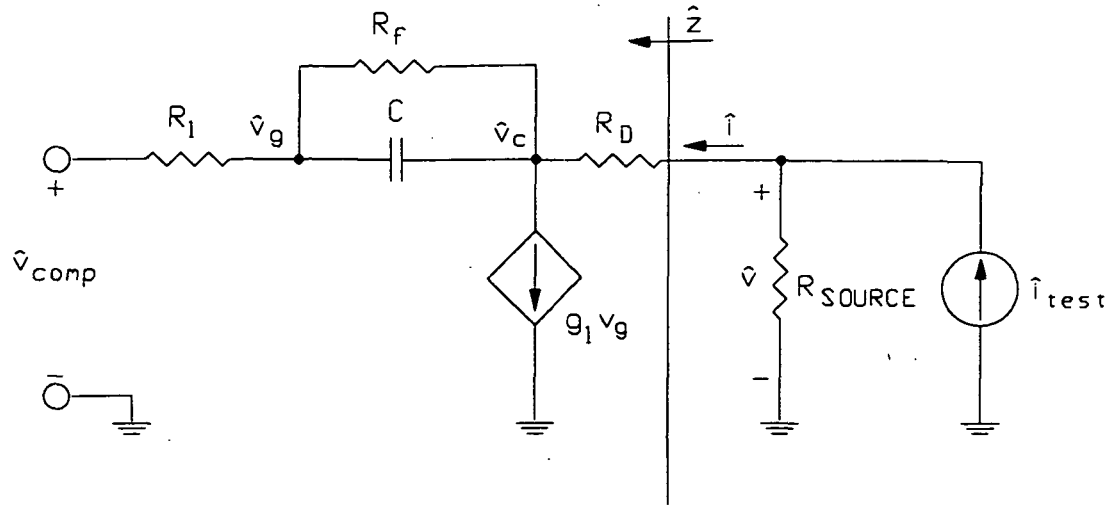
Fig. 3.3 Arcjet dynamic impedance data (Source: [4])

Fig. 3.4 Circuit used to derive the simulator theoretical dynamic impedance

$$\hat{z} = \frac{\hat{v}}{\hat{i}} = \frac{(R_D - k_T \cdot V \cdot X)}{(1 + k_T \cdot I \cdot X)} \qquad (3.4)$$

Substituting for X from (3.3) gives:

$$\hat{z} = \frac{R_D + k_T \cdot V \cdot \left(\dfrac{1 + s \cdot R_a \cdot C_a}{s \cdot R_2 \cdot C_a}\right) \cdot \left(\dfrac{A_{mid}}{1 + \dfrac{s}{\omega_H}}\right)}{1 - k_T \cdot I \cdot \left(\dfrac{1 + s \cdot R_a \cdot C_a}{s \cdot R_2 \cdot C_a}\right) \cdot \left(\dfrac{A_{mid}}{1 + \dfrac{s}{\omega_H}}\right)} \qquad (3.5)$$

If, as discussed in Chapter 2, the compensator zero is made to cancel with the final stage pole, then the dynamic impedance reduces to:

$$\hat{z} = \frac{R_D + \dfrac{k_T \cdot V \cdot A_{mid}}{s \cdot R_2 \cdot C_a}}{1 - \dfrac{k_T \cdot I \cdot A_{mid}}{s \cdot R_2 \cdot C_a}} \qquad (3.6)$$

Rearrangement of (3.6) yields

$$\hat{z} = \frac{R_D \cdot \left(s + \dfrac{k_T \cdot V \cdot A_{mid} \cdot T}{R_D} \right)}{s - k_T \cdot I \cdot A_{mid} \cdot T} \quad where \quad T = \frac{1}{R_2 \cdot C_a} \quad (3.7)$$

where as shown in (2.15) A_{mid} is a negative number. (3.7) can also be written as:

$$\hat{z} = \left(-\frac{V}{I} \right) \cdot \left(\frac{1 - \dfrac{s}{\omega_z}}{1 + \dfrac{s}{\omega_p}} \right) \quad (3.8)$$

where:

$$\omega_z = \left| \frac{A_{mid} \cdot K_T \cdot V \cdot T}{R_D} \right| \quad and \quad \omega_p = \left| A_{mid} \cdot k_T \cdot I \cdot T \right|$$

For low frequencies (3.7) and (3.8) reduce to,

$$\hat{z} \approx -\frac{V}{I} \quad (3.9)$$

which as discussed in Chapter 2, is the expected value of dynamic impedance for a load device which has a constant power I-V characteristic. Thus, for low frequencies the theoretical dynamic impedance of the simulator consist of a negative real component, in agreement with that of an actual arcjet thruster.

Using the HP Dynamic Signal Analyzer (model 3562A) in its synthesis mode [11], plots of the imaginary and real parts of (3.7) vs. frequency were obtained for simulated load currents of 6, 10 and 14 A. The upper cutoff frequency (UCF) was also calculated for each of these operating points and is noted in the upper right corner of each plot (note that the measurement range of the HP 3562A is limited to: 64 μHz - 100kHz). The results, shown in Figs. 3.5, 3.6 and 3.7, are consistent with those obtained from an actual arcjet thruster as given by Hamley's paper and shown in Fig. 3.3 [4].

Finally, using the experimental setup shown in Fig. 3.8 and operating along static I-V characteristic #1 of Fig. 3.2, plots of the imaginary and real parts vs. frequency of the actual simulator dynamic impedance for simulator load currents of 6, 10 and 14 A were
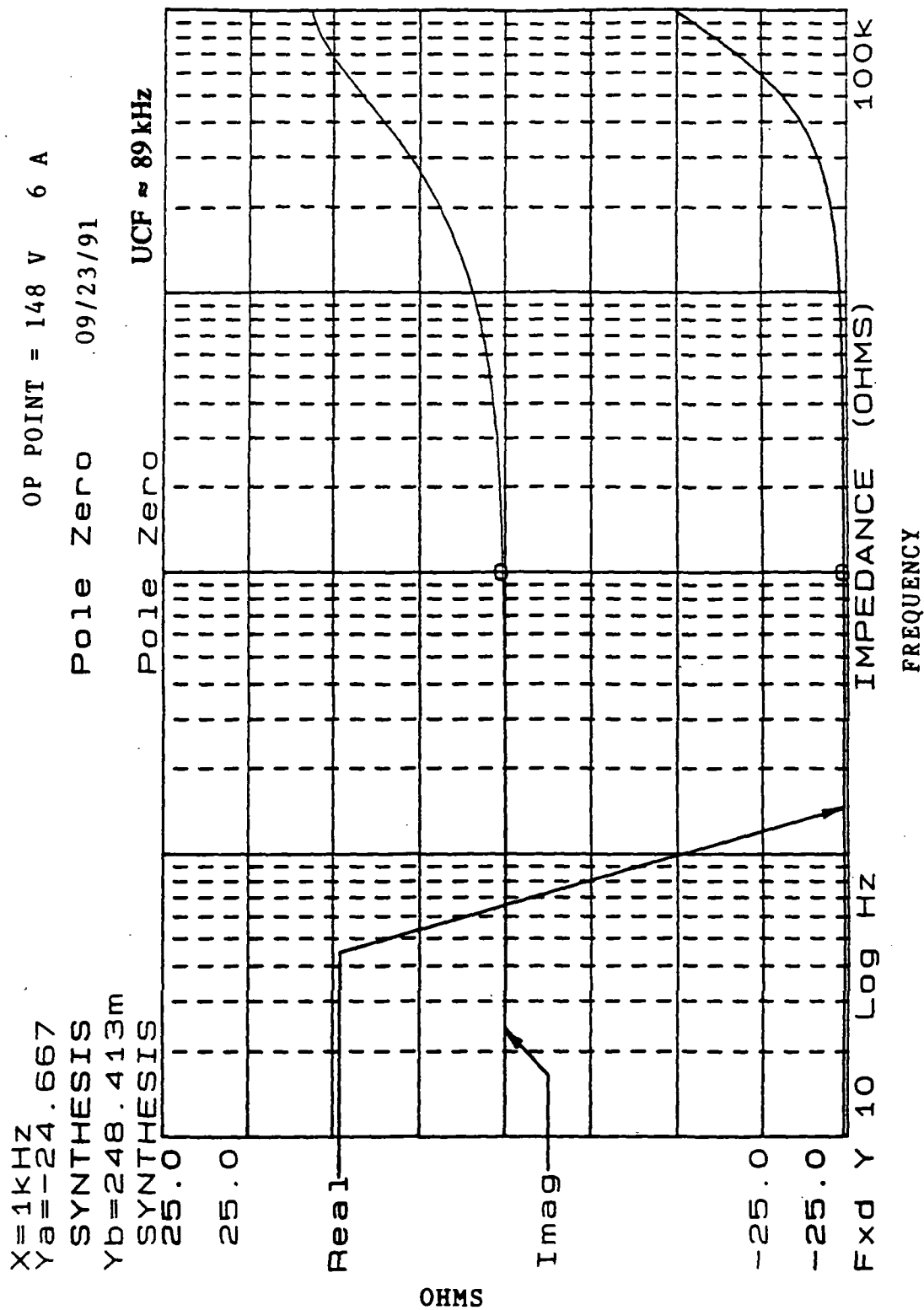
Fig. 3.5 Real and imaginary components of (3.7) vs. frequency for I=6 A and V=148 V
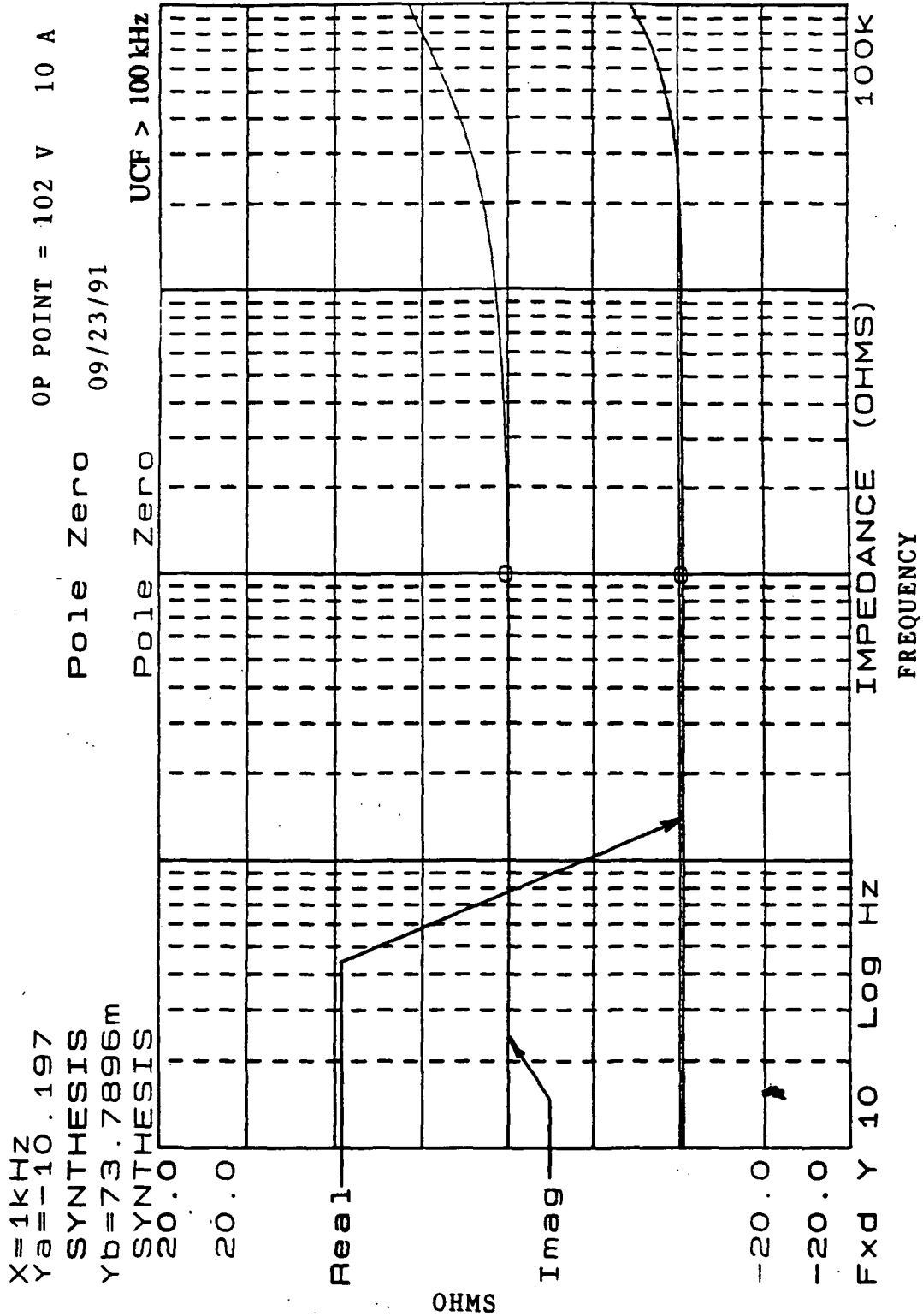
Fig. 3.6 Real and imaginary components of (3.7) vs. frequency for I=10 A and V=102 V
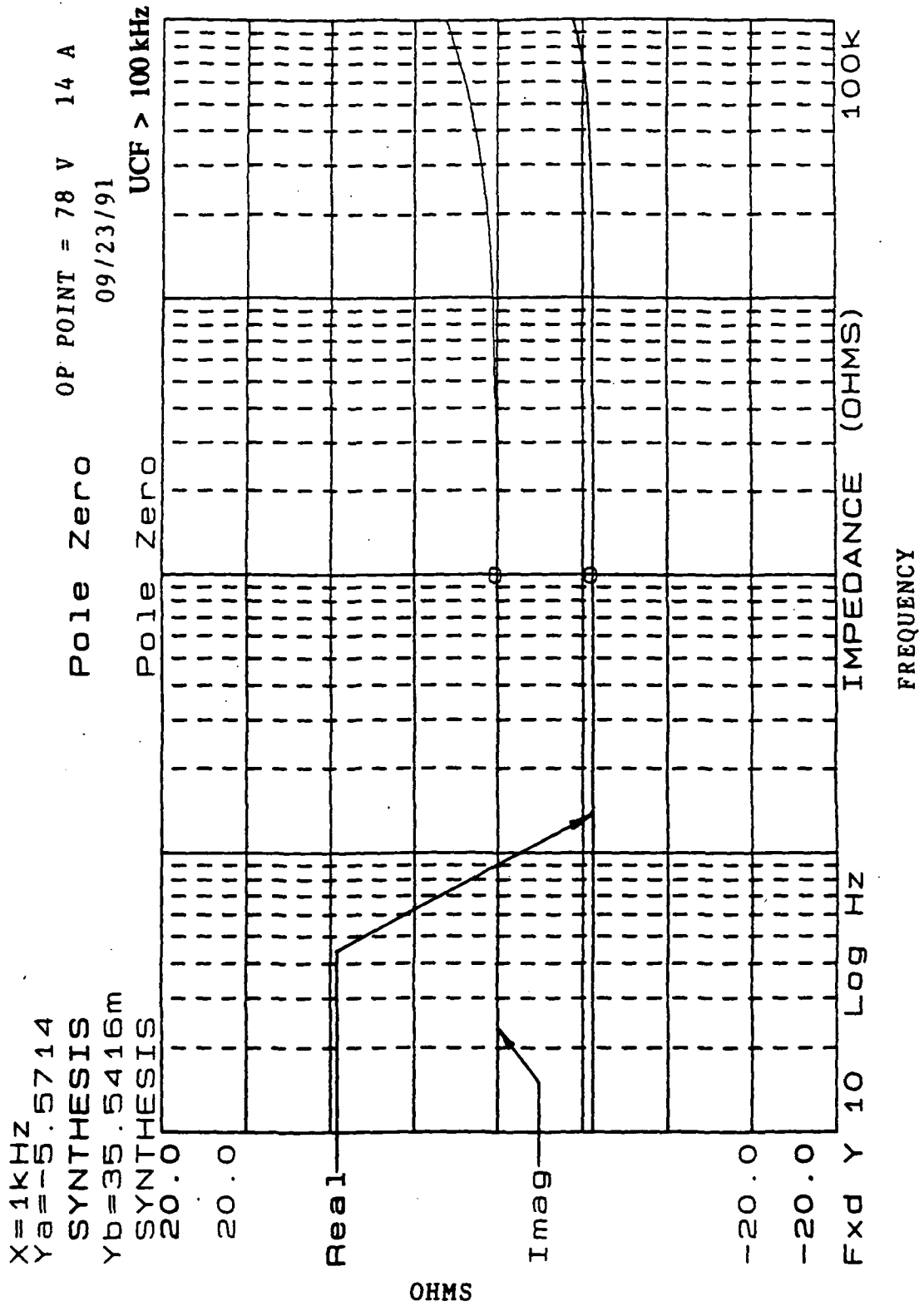
Fig. 3.7 Real and imaginary components of (3.7) vs. frequency for I=14 A and V=78 V
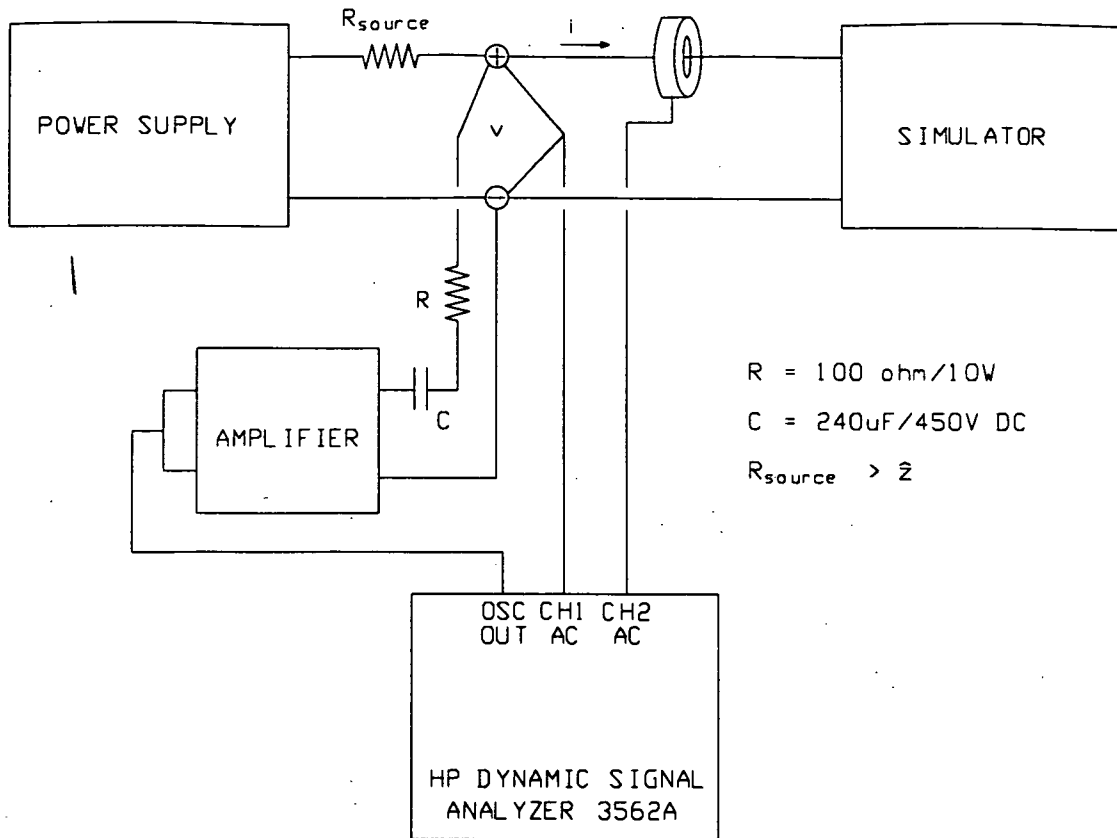
Fig. 3.8 Experimental set-up used to obtain the dynamic impedance of the simulator

obtained. In addition, the simulator upper cutoff frequency for each of these operating points was measured and noted. These results are shown in Figs. 3.9, 3.10 and 3.11.

As previously noted the low frequency simulator dynamic impedance, at a given operating point, is also equivalent to the slope of the tangent to the static I-V curve at that operating point. Thus, comparing the low frequency real part values of Figs. 3.9-3.11 with the slopes of the tangents at points (a), (b), and (c) of Fig. 3.2, shows close agreement between corresponding low frequency dynamic impedance values (Note that the low frequency dynamic impedance values of Fig. 3.5-3.7 and 3.9-3.11 are given by Y_a in the upper left hand corner of each plot). Differences can be attributed to the limited number of sampling points used to construct the static I-V curve, and to the limited degree
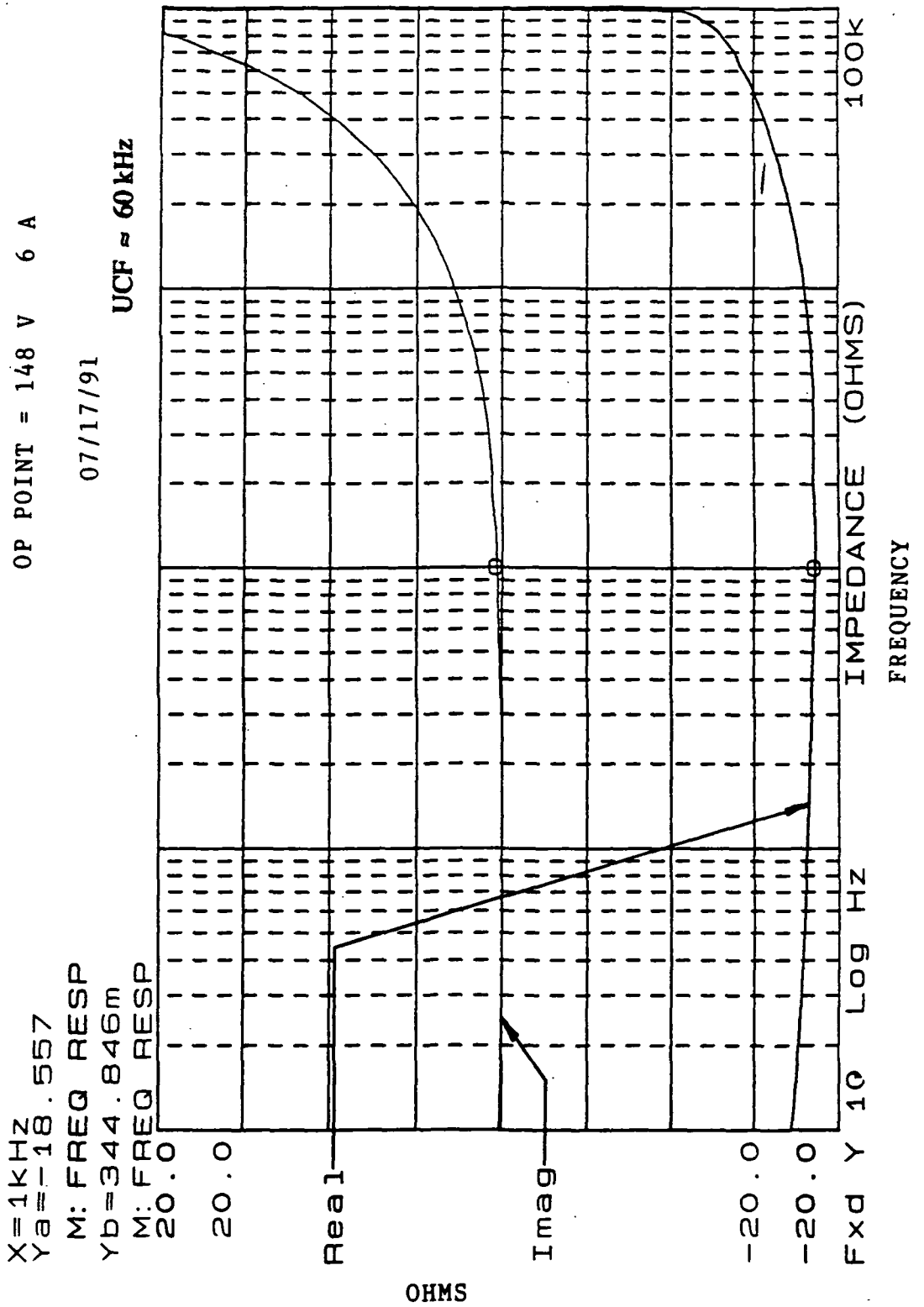
Fig. 3.9 Simulator experimental dynamic impedance components vs. frequency for I=6 A and V=148 V
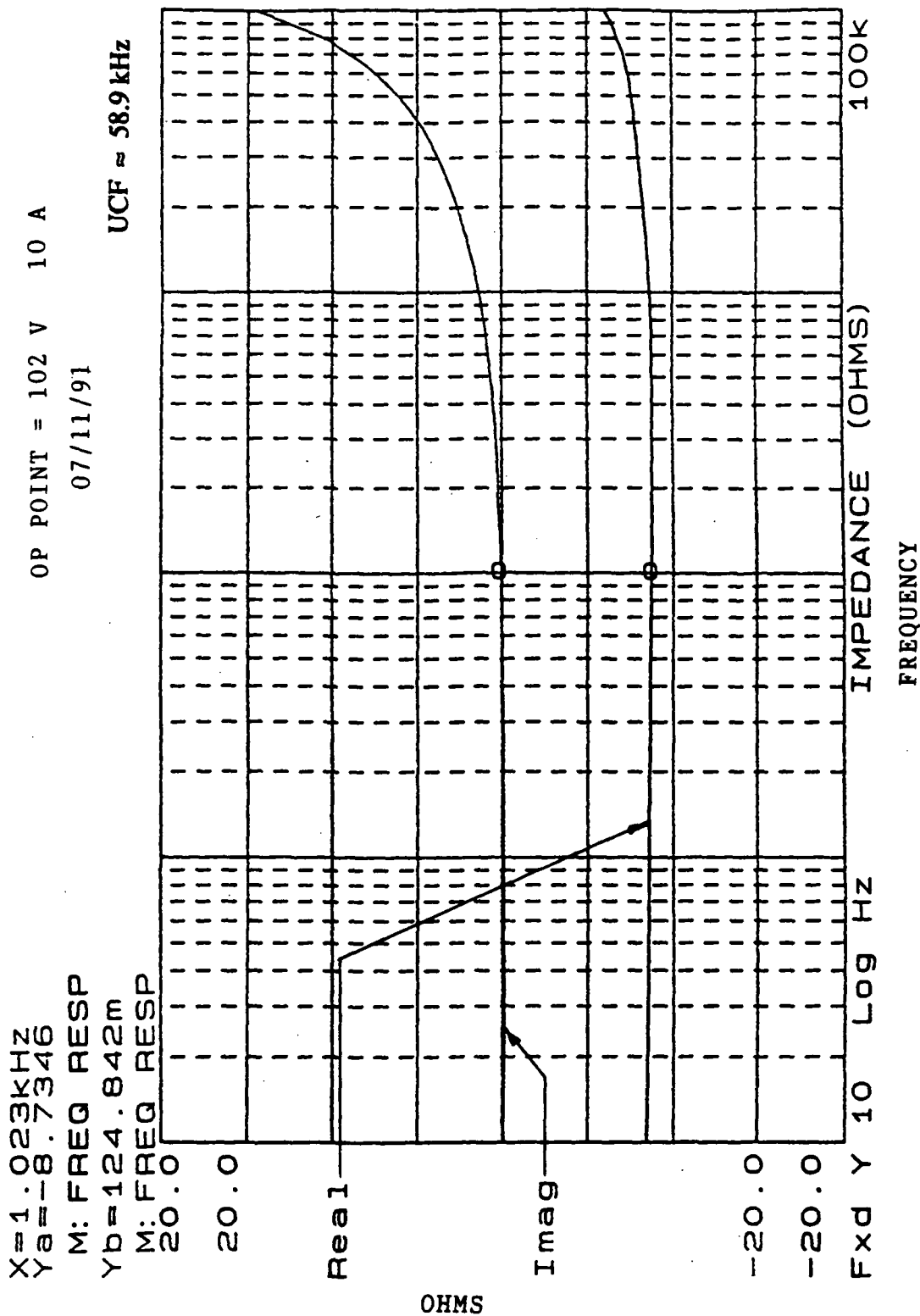
Fig. 3.10 Simulator experimental dynamic impedance components vs. frequency for
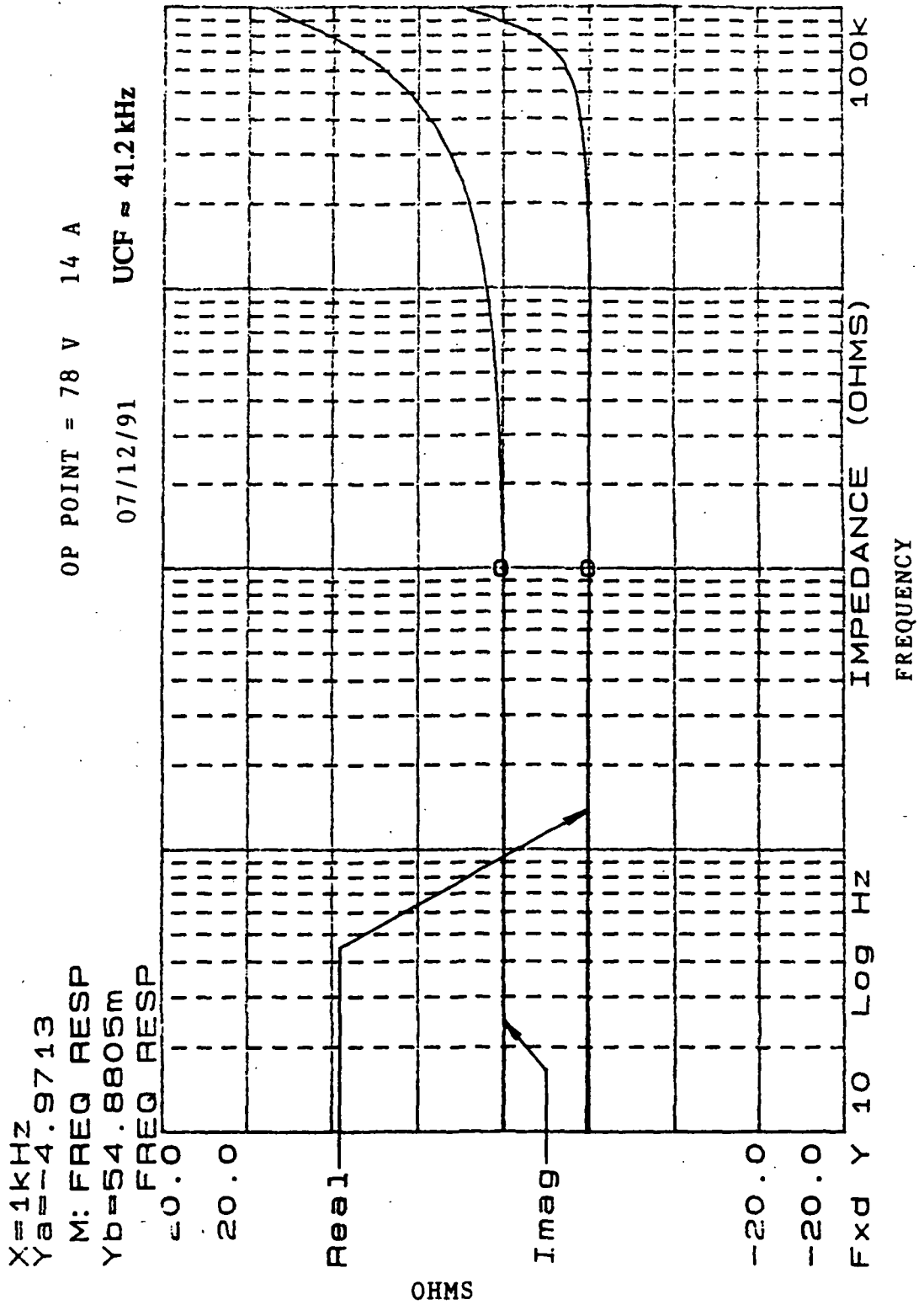I=10 A and V=102 V

Fig. 3.11 Simulator experimental dynamic impedance components vs. frequency for
I=14 A and V=78 V

of accuracy used to construct the tangent at each operating point.

As shown in Table 3.1, there is a slight difference between the theoretical and experimental low frequency dynamic impedance values at each operating point. The reason for this difference is that the theoretical low frequency dynamic impedance value is given by (3.9), which as already mentioned is equivalent to the slope of the tangent to a constant power curve at the operating point (I,V). Whereas, the experimental low frequency dynamic impedance value is given by the slope of the tangent to static I-V curve #1 of Fig. 3.2, at the operating point (I,V). And as discussed in section 3.2, I-V curve #1 of Fig. 3.2 is actually rotated from that of a constant power curve in such a manner that it produces a smaller tangential slope magnitude at a given operating point than a constant power curve would, which verifies the results shown in Table 3.1.

Low Frequency Dynamic Impedance Values			
Operating Point	I=6 A V=148 V	I=10 A V=102 V	I=14 A V=78 V
Theoretical	-24.67 Ω	-10.20 Ω	-5.57 Ω
Experimental	-18.56 Ω	-8.73 Ω	-4.97 Ω

Table 3.1 Comparison of theoretical and experimental simulator dynamic impedances

Overall, the experimental results shown in Figs. 3.9-3.11 are consistent with the synthesis analysis (theoretical results), of Figs. 3.5 - 3.7, and Hamley's results [4]. Thus it can be said that the static and dynamic impedances of the simulator closely resemble those of an actual arcjet thruster. Note that the simulator upper cutoff frequency (≈60kHz) agrees closely with that of the arcjet thruster (≈40-50kHz) for an output current of 10A. The synthesis plots show a higher upper cutoff frequency (≈100kHz) because the synthesis analysis does not take into account any of the simulator's higher order poles and zeroes.

Chapter 4

SIMULATOR PERFORMANCE

4.1 INTRODUCTION

The purpose of this chapter is to examine simulator performance. This was accomplished by comparing the results obtained from testing the simulator with a current-mode-controlled (CMC) converter, with a load-current-regulating outer control loop designed for 1 kW arcjet applications, with those obtained by testing an arcjet thruster with the same converter. The thruster testing was performed at the NASA Lewis Research Center using a NASA 1 kW arcjet thruster. For the test set-up, shown in Fig. 4.1, the CMC converter was adjusted for a constant DC output current of 10 A. The
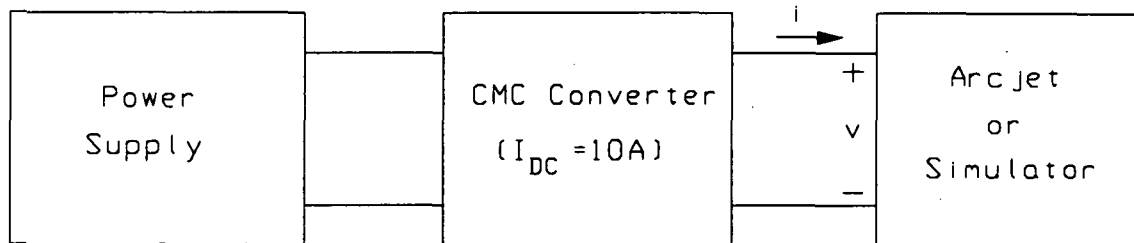
Fig. 4.1 Experimental set-up used for testing with a CMC converter

CMC converter used for this testing is shown in Fig. 4.2. This converter has been described in detail elsewhere [12]. The ignition circuit referenced in Fig. 4.2 is shown in Fig. 4.3. This ignition circuit was developed following the guidelines set forth in [13]. The purpose of the ignition circuit is to provide a high voltage pulse between the anode and cathode of the arcjet thruster to ignite the arc.
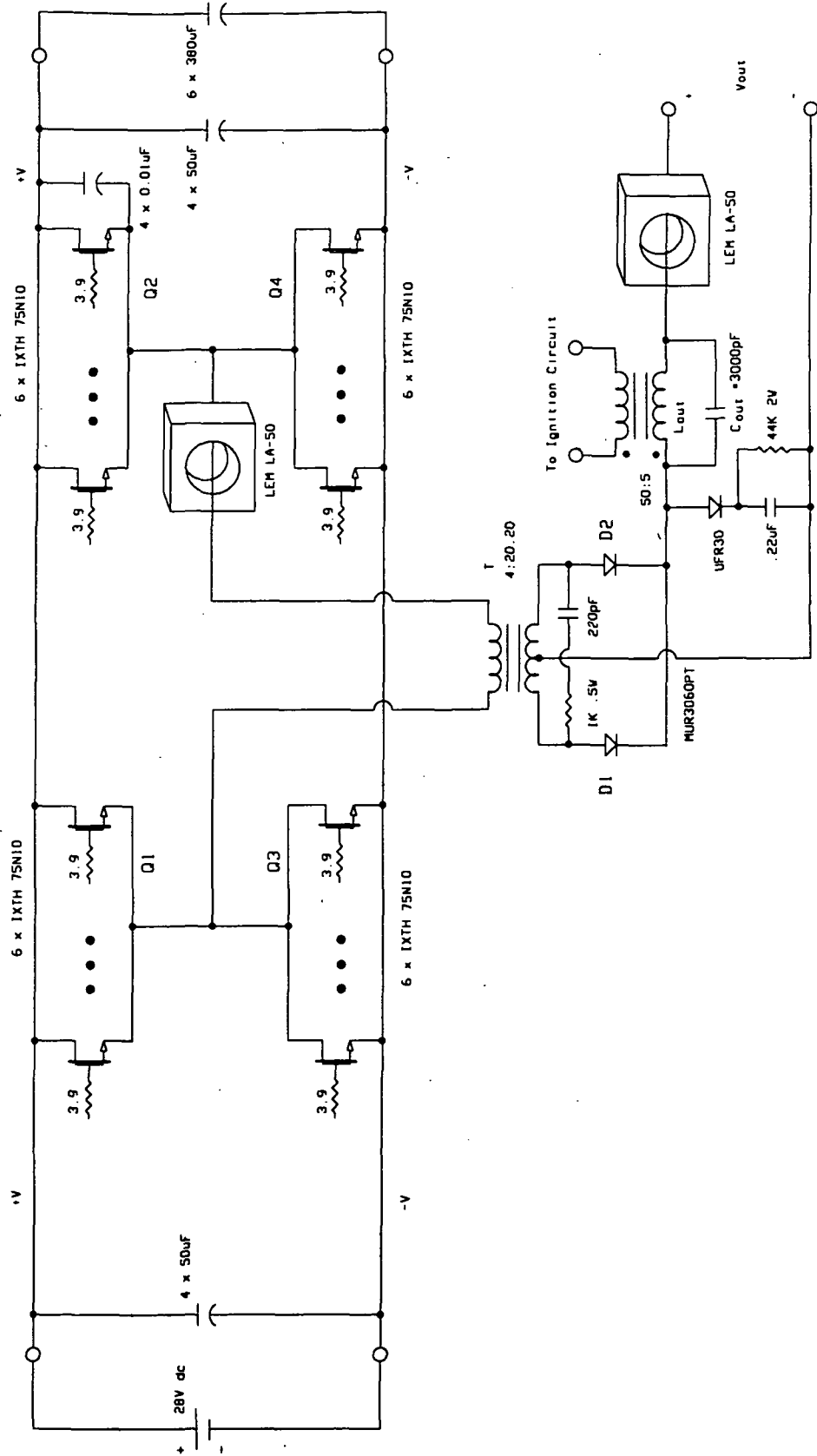
47

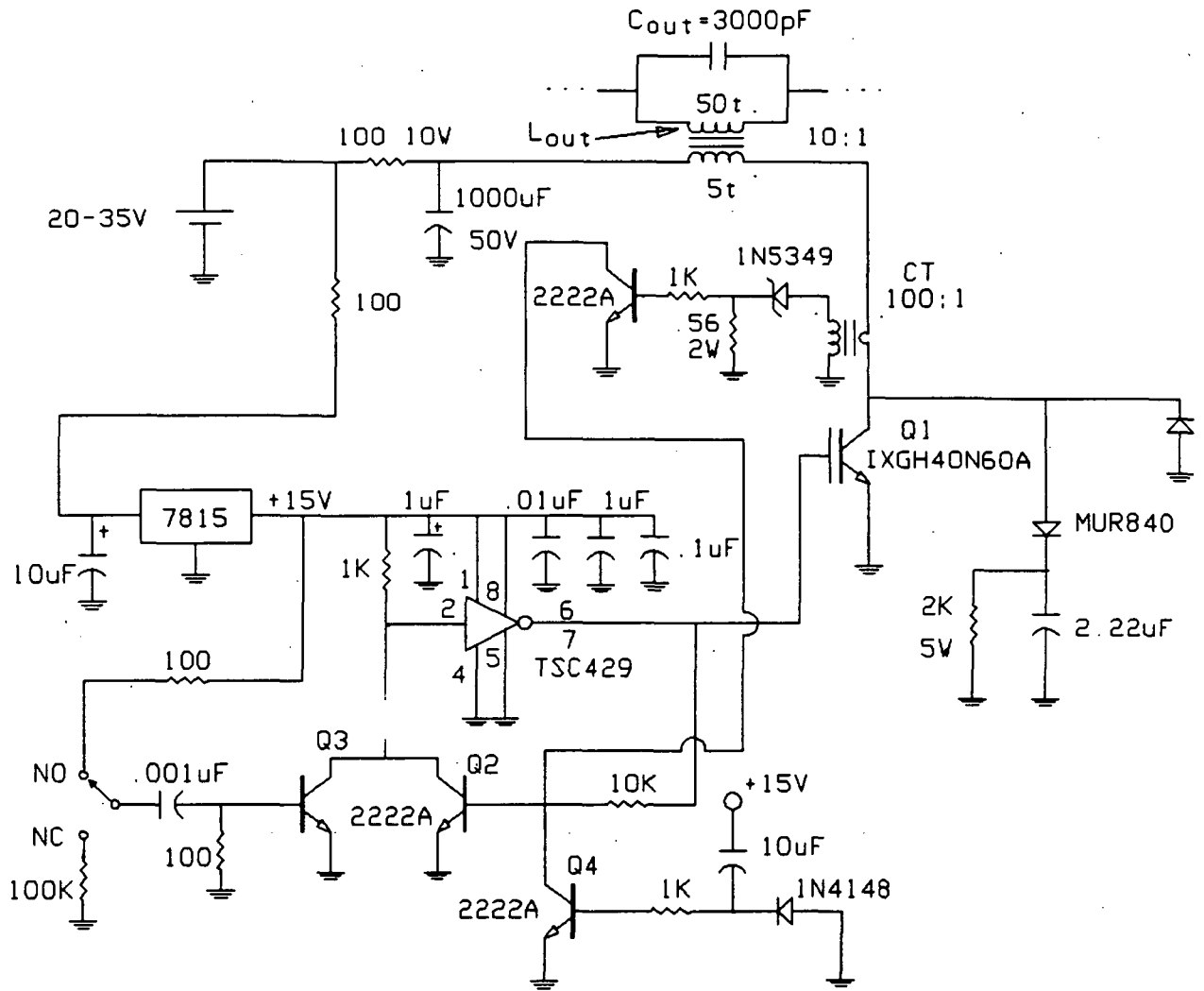Fig. 4.2 The CMC converter used in the experimental set-up of Fig. 4.1 (Source: [12])

Fig. 4.3 The ignition circuit referenced in Fig 4.2

4.2 STEADY STATE OUTPUT RIPPLE

The CMC converter of Fig. 4.2 was initially designed to have an output inductance (L_{out}) of 384 µH. However, to ensure a wide enough ignition pulse to ignite the arc, the converter was also tested with an output inductance of 2 mH. Therefore the steady state output ripple results will be given for both values of output inductance.

4.2.1 Steady State Output Ripple with $L_{out} = 384$ µH

The steady state output ripple characteristics of an arcjet thruster tested with the CMC converter of Fig. 4.1 ($L_{out} = 384$ µH) are shown in Fig. 4.4(a), while those of the simulator tested with the same converter are shown in Fig. 4.4(b). The simulator results of Fig. 4.4(b) were obtained by adjusting the power potentiometer of the simulator (shown in Fig. 2.3) so that the converter DC output voltage was equal to that of Fig. 4.4(a), which is approximately 90 V.

Observation of Fig. 4.4(b) reveals that the simulator is indeed performing as expected, producing output ripple characteristics which clearly indicate a negative simulator dynamic impedance (the change in voltage to the change in current ratio is negative for a given time period), as expected from the discussion of Chapter 3.

Comparison of Figs. 4.4(a) and (b) reveals similarities to the extent that they both have a negative dynamic impedance and they both exhibit similar ringing characteristics. The causes of ringing will be discussed in section 4.2.2. The figures are different to the extent that they appear to have unequal dynamic impedances, and the ringing is more damped in the simulator results of Fig. 4.4(b) than it is in the arcjet results of Fig. 4.4(a). Calculating the dynamic impedance from the change in voltage and current data shown for each figure, yields:

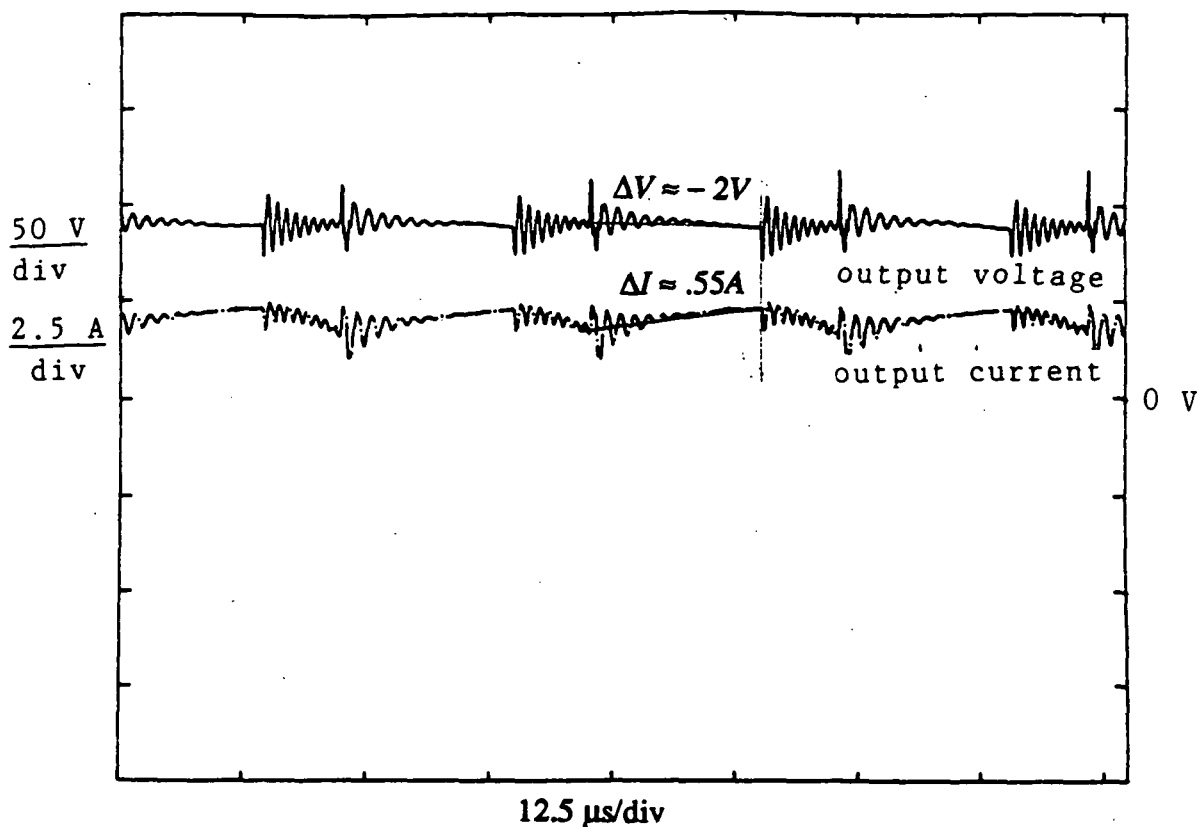$$\hat{z} = \frac{\Delta V}{\Delta I} \approx -3.6\Omega \quad \text{for} \quad Fig.4.4(a)$$

$\Delta V \approx - 2V$

$\Delta I \approx .55A$

output voltage

output current

0 V

50 V / div

2.5 A / div

12.5 µs/div

Fig. 4.4(a) Arcjet steady state output ripple characteristics for $L_{out} = 384$ µH

11401 Digitizing Oscilloscope   09-25-1991

ΔV•7.65V

output voltage

OV

ΔI•1 18A

output current

OA

50V /div

2.5A /div

I0uS/div
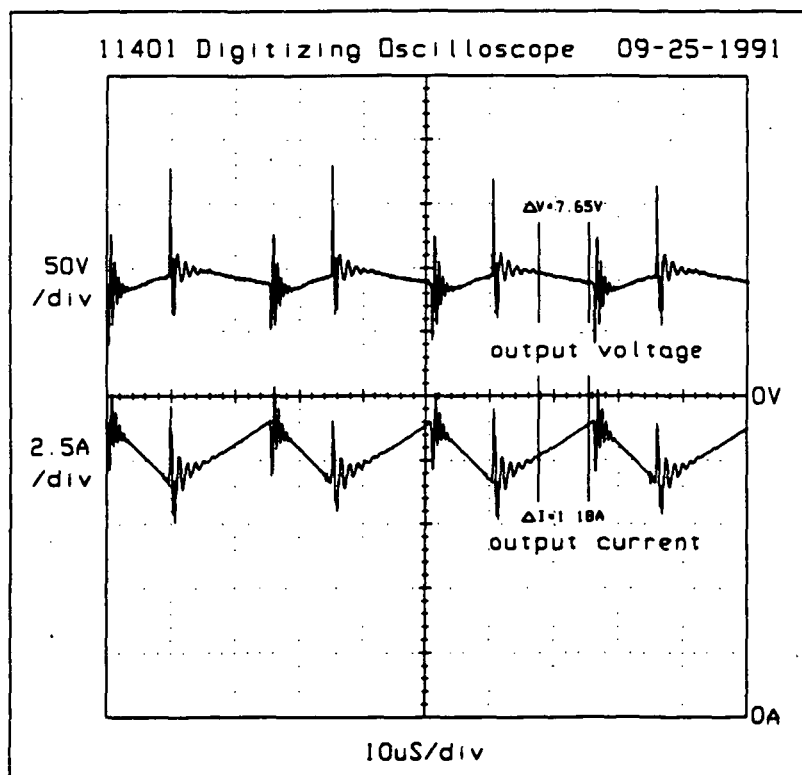
Fig. 4.4(b) Simulator steady state output ripple characteristics for $L_{out} = 384$ µH

$$\hat{z} = \frac{\Delta V}{\Delta I} \approx -6.5\Omega \quad \text{for} \quad Fig.4.4(b)$$

Thus, the simulator has a higher value of dynamic impedance than the arcjet. Comparing the slopes of the tangents to the I-V curves of Fig. 1.2 with those of Fig. 3.2, for a given current, shows that this was an expected result.

The circuit responsible for the output ringing can be simplified to that of Fig. 4.5, where L represents the converter stray and/or leakage inductance involved, C_{out} represents the ignition capacitor of the converter, r_d represents the dynamic impedance of the simulator, and R_{loss} represents the total losses of the resonant circuit of Fig. 4.5.
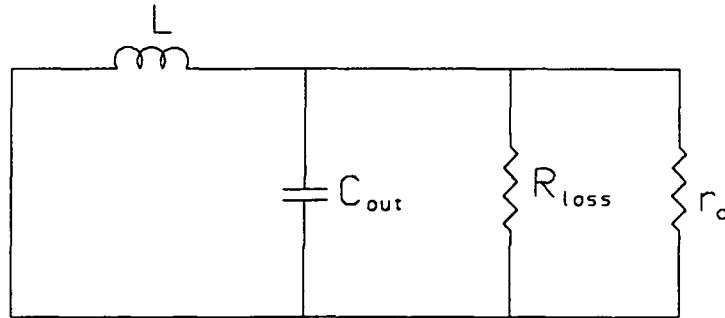

Fig. 4.5 Simplified output ringing circuit

If $R_{loss} < |r_d|$ (usually the case for Fig. 4.5) and R_{eq} is defined as the parallel combination of r_d and R_{loss}, that is,

$$R_{eq} = \frac{r_d R_{loss}}{r_d + R_{loss}}$$

and remembering that r_d is a negative number, it becomes apparent that higher magnitudes of r_d will give lower values of R_{eq} resulting in more damping of the output ringing. Therefore, the fact that Figs. 4.4(a) and (b) have unequal damping can be attributed to their unequal dynamic impedances, and as expected the figure with the higher magnitude of r_d (Fig. 4.4(b)) has the greater damping.

Later (in Chapter 5), it will be shown how to change the dynamic impedance of the simulator so that it more closely resembles that of the arcjet thruster. For now, it is simply noted that the simulator and thruster produce similar output ripple characteristics when tested with a CMC converter having an output inductance of 384 μH.

4.2.2 Investigation of Output Ringing

A plot of the CMC converter transformer primary current (when tested with the simulator) is shown in Fig. 4.6. During the time interval t_a shown in Fig. 4.6, the appropriate pair of bridge transistors (Q1 & Q4 or Q2 & Q3) along with the appropriate rectifier diode (D1 or D2) of Fig. 4.2, are conducting. Therefore, for the time interval t_a, the incremental converter circuit of Fig. 4.7 is in effect.

Examination of Fig. 4.7 reveals that the ringing during time interval t_a, of Fig. 4.6, is caused mainly by the primary to secondary leakage inductance of the transformer, referred to the secondary, acting in conjunction with the 3000 pF ignition capacitor (C_{out}).

A plot of the CMC converter transformer secondary current (when tested with the simulator) is shown in Fig. 4.8. During the time interval t_b shown in Fig. 4.8, the appropriate pair of bridge transistors (Q1 & Q3 or Q2 & Q4) and both rectifier diodes (D1 & D2) of Fig. 4.2, are conducting. Therefore, for the time interval t_b, the incremental converter circuit of Fig. 4.9 is in effect.

Examination of Fig. 4.9 reveals that both the transformer primary and secondary windings are directly shorted. Therefore the ringing during time interval t_b, of Fig. 4.8, is caused mainly by the secondary to secondary leakage inductance plus the stray inductance of the secondary circuit, acting in conjunction with the 3000 pF ignition capacitor (C_{out}). This conclusion is supported by the fact that there is no ringing in the transformer primary
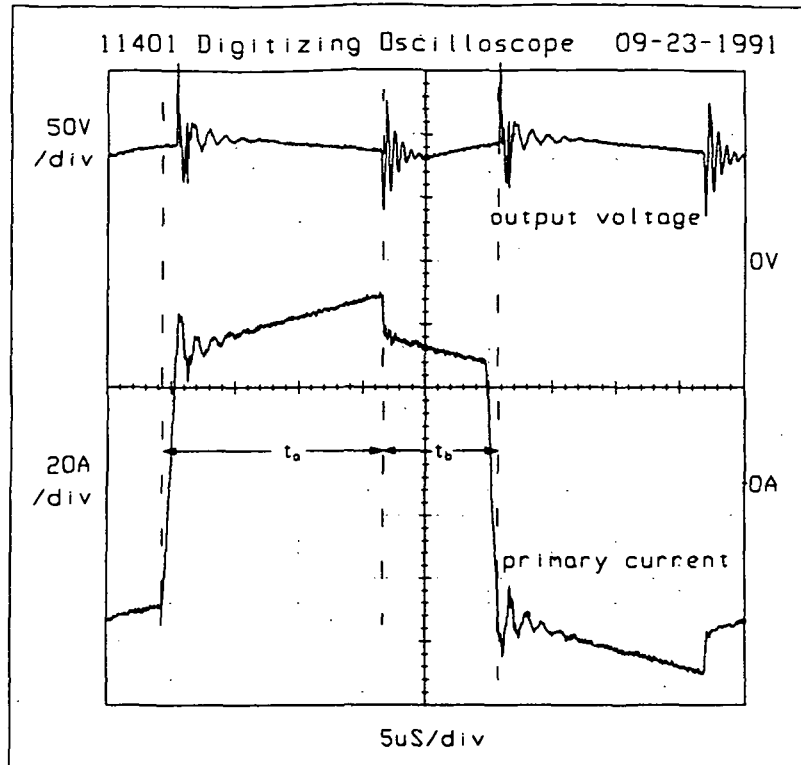
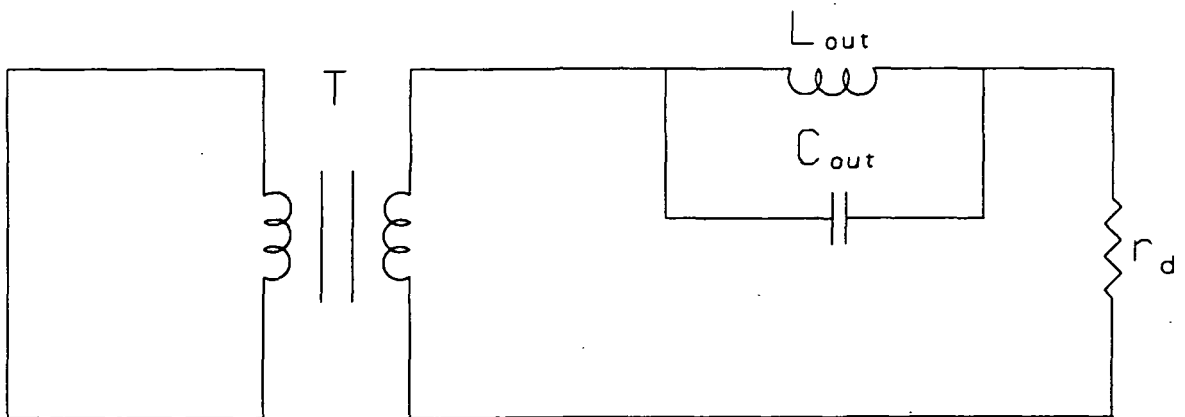Fig. 4.6 CMC converter transformer primary current and output voltage ripple

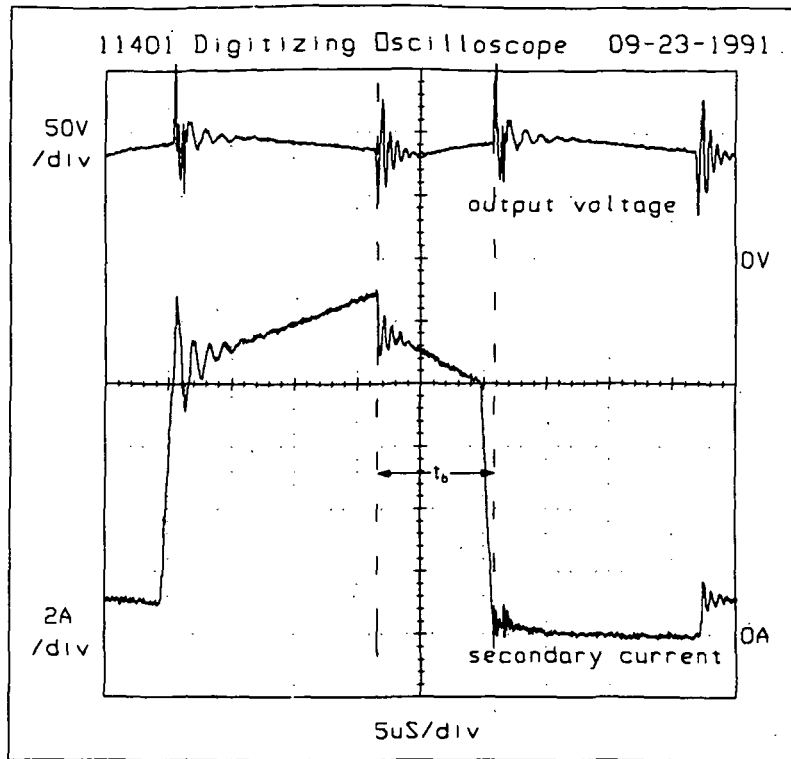Fig. 4.7 Incremental converter circuit for time interval t_a

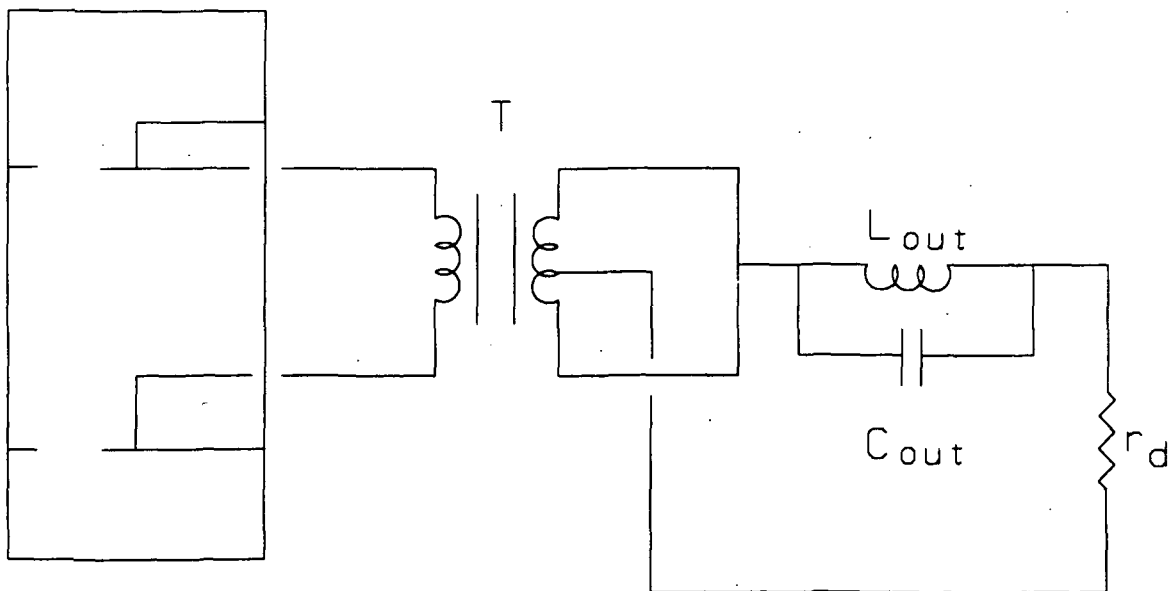Fig. 4.8 CMC converter transformer secondary current and output voltage ripple

Fig. 4.9 Incremental converter circuit for time interval t_b

current of Fig. 4.6 during the time interval t_b.

The ringing during time interval t_b has a higher frequency than that of time interval t_a. This comes as no surprise since the secondary to secondary leakage inductance plus the stray inductance of the secondary circuit is expected to be much less than the primary to secondary leakage inductance of the transformer referred to the secondary, and the ringing frequency is determined from:

$$\omega = \frac{1}{\sqrt{L\,C}}$$

4.2.3 Steady State Output Ripple with $L_{out} = 2$ mH

The steady state output ripple characteristics of an arcjet thruster tested with the CMC converter of Fig. 4.2 ($L_{out} = 2$ mH) are shown in Fig. 4.10(a), while those of the simulator tested with the same converter are shown in Fig. 4.10(b). In this case, the simulator results were obtained by setting the power potentiometer of the simulator to obtain a converter DC output voltage equal to that of Fig. 4.10(a), which is approximately 99 V.

As expected, the results of Figs. 4.10(a) and (b) are very similar to those of Figs. 4.4(a) and (b). The only difference between the two sets of figures is a smaller ripple amplitude for Figs. 4.10(a) and (b). This is to be expected since the converter output inductance (L_{out}) is significantly larger for these two figures than it is for Figs. 4.4(a) and (b).

All other aspects of Figs. 4.10(a) and (b) are the same as discussed in section 4.2.1 with Figs. 4.4(a) and (b) replaced everywhere by Figs. 4.10(a) and (b), respectively.
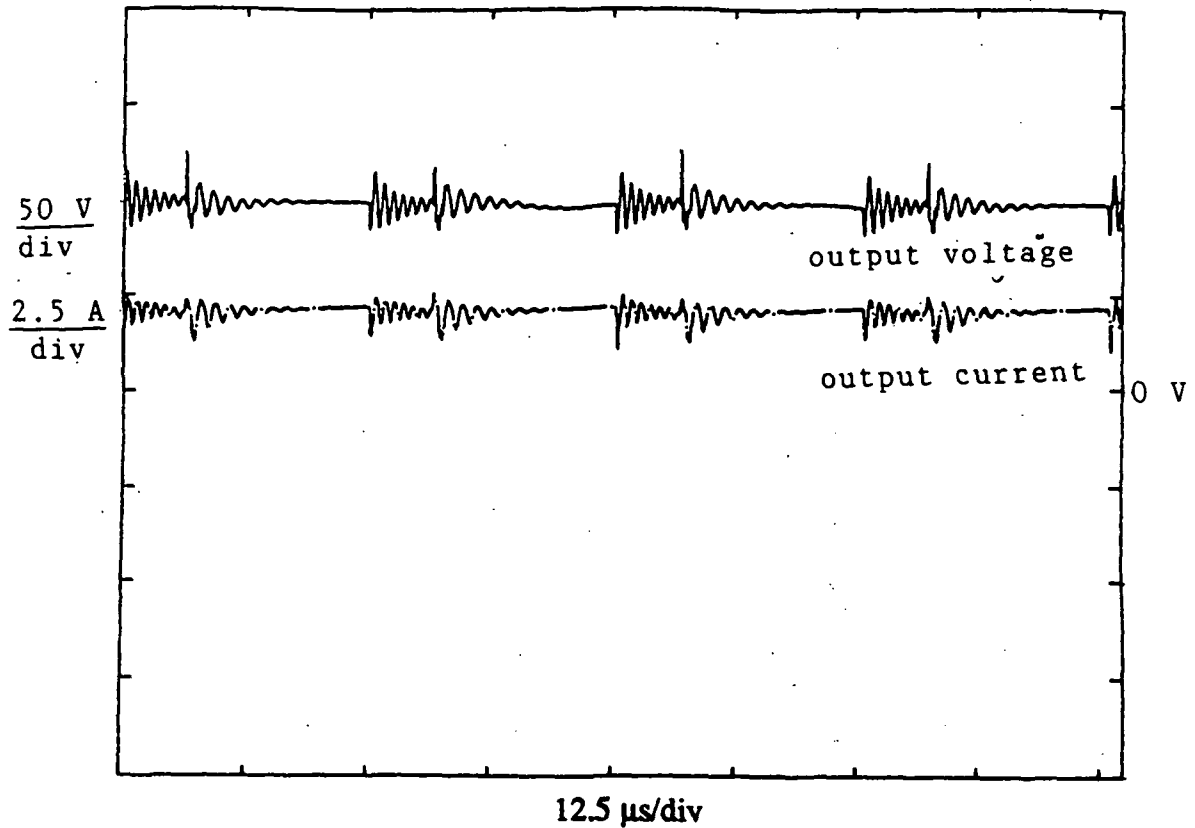
$$50 \text{ V} \over \text{div}$$

$$2.5 \text{ A} \over \text{div}$$

output voltage

output current

0 V

12.5 μs/div

Fig. 4.10(a) Arcjet steady state output ripple characteristics for $L_{out} = 2$ mH

11401 Digitizing Oscilloscope   09-25-1991

50V /div

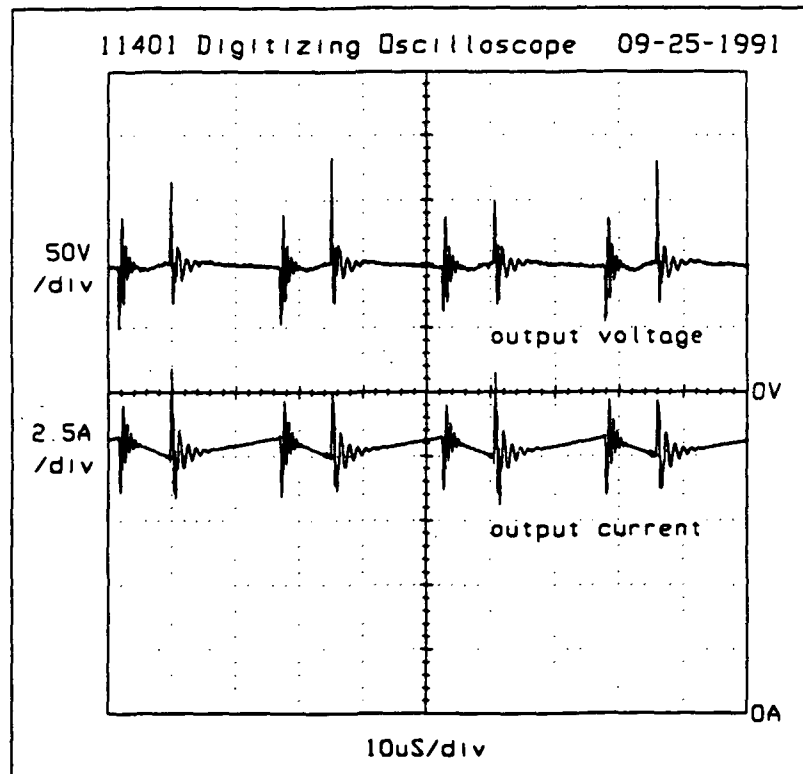output voltage

0V

2.5A /div

output current

0A

10uS/div

Fig. 4.10(b) Simulator steady state output ripple characteristics for $L_{out} = 2$ mH

4.5 LARGE SIGNAL TRANSIENT RESPONSE WITH $L_{out} = 2$ mH

The large signal transient response of an arcjet thruster tested with the CMC converter ($L_{out} = 2$ mH) is shown in Fig. 4.11(a), while that of the simulator tested with the same converter is shown in Fig. 4.11(b). These measurements were taken by injecting a pulse waveform into the control circuit of the converter, as shown in Fig. 4.12. The pulse magnitude was set to the maximum allowable value which did not cause simulator or thruster turn-off.

It is apparent that the current and voltage waveforms of the arcjet shown in Fig. 4.11(a), closely resemble those of the simulator shown in Fig. 4.11(b). The slight differences are believed to be caused by the unequal dynamic impedances of the simulator and arcjet. Finally, as expected for a negative dynamic impedance, the current pulse goes negative for a corresponding positive pulse in voltage.

Further examination of Figs. 4.11(a) and (b) reveals evidence of underdamped ringing on the current and voltage pulse waveforms. This underdamped ringing indicates the presence of a complex conjugate pole pair in the system (the converter and its load) transfer function, which is located in the left half s-plane, fairly close to the $j\omega$-axis. Therefore, the bandwidth and phase margin of the system are relatively small, resulting in a marginally stable system. This occurs because the converter loop gain was originally compensated by using a resistive load bank in place of the simulator (before the simulator was designed). This is demonstrated in Fig. 4.13, where the large signal transient response of a resistive load bank tested with the CMC converter, for the same conditions as Figs. 4.11(a) and (b), is shown. Examination of this figure reveals that the system is more than adequately compensated for a resistive load.

Thus, to increase system stability, the converter loop gain should be compensated when the converter is operating with the actual load it was designed for. Hence, another
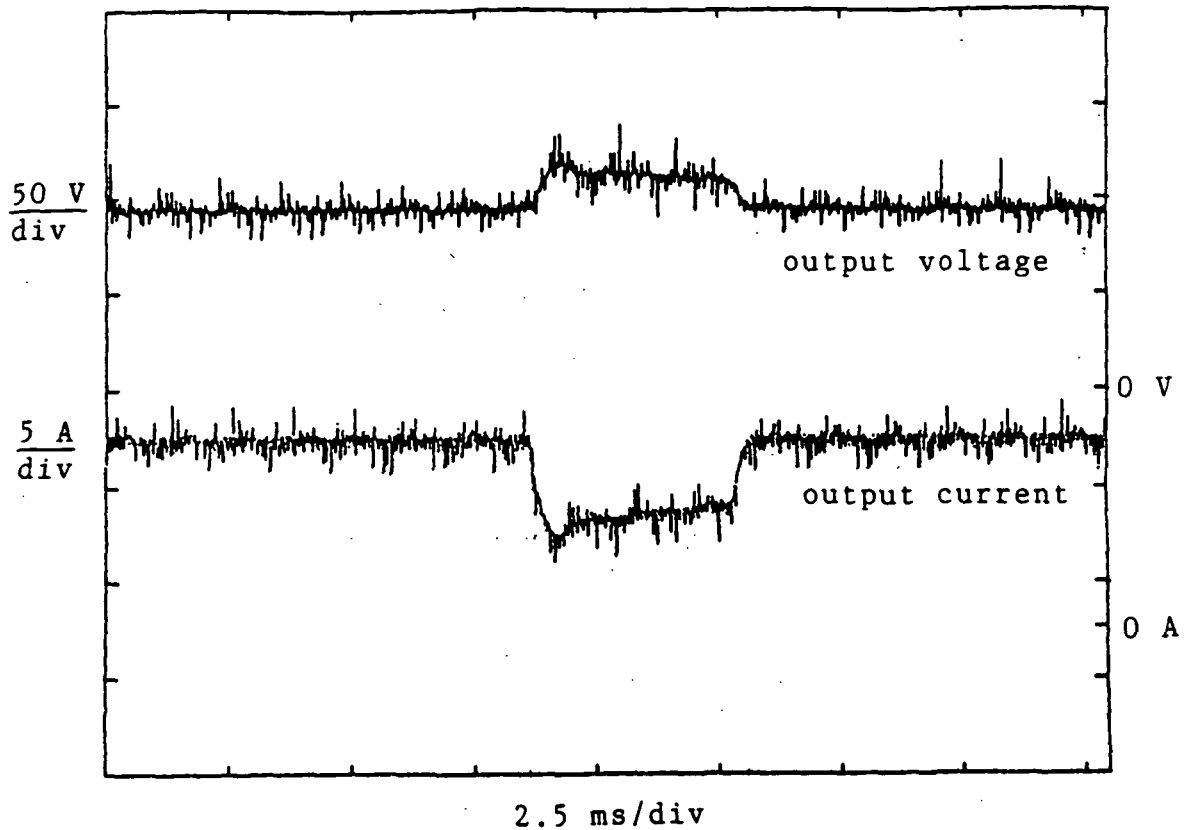
$$\frac{50\ V}{div}$$

output voltage

0 V

$$\frac{5\ A}{div}$$

output current

0 A

2.5 ms/div

Fig. 4.11(a) Arcjet large signal transient response for $L_{out} = 2$ *mH*

11401 Digitizing Oscilloscope   09-23-1991

50V /div

output voltage

0V

5A /div

ouput current

0A

10V /div

pulse reference

2nS/div
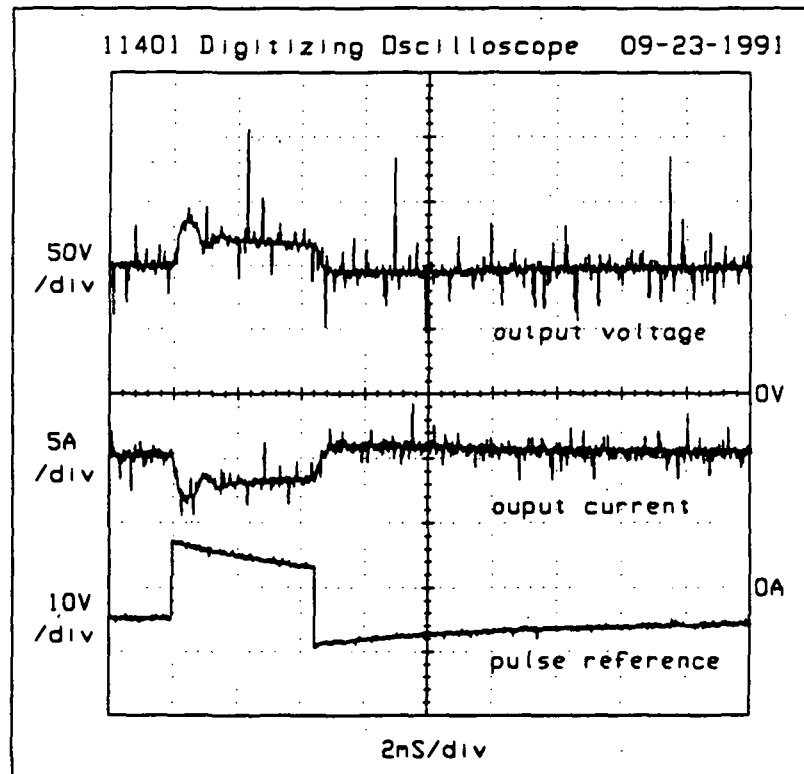
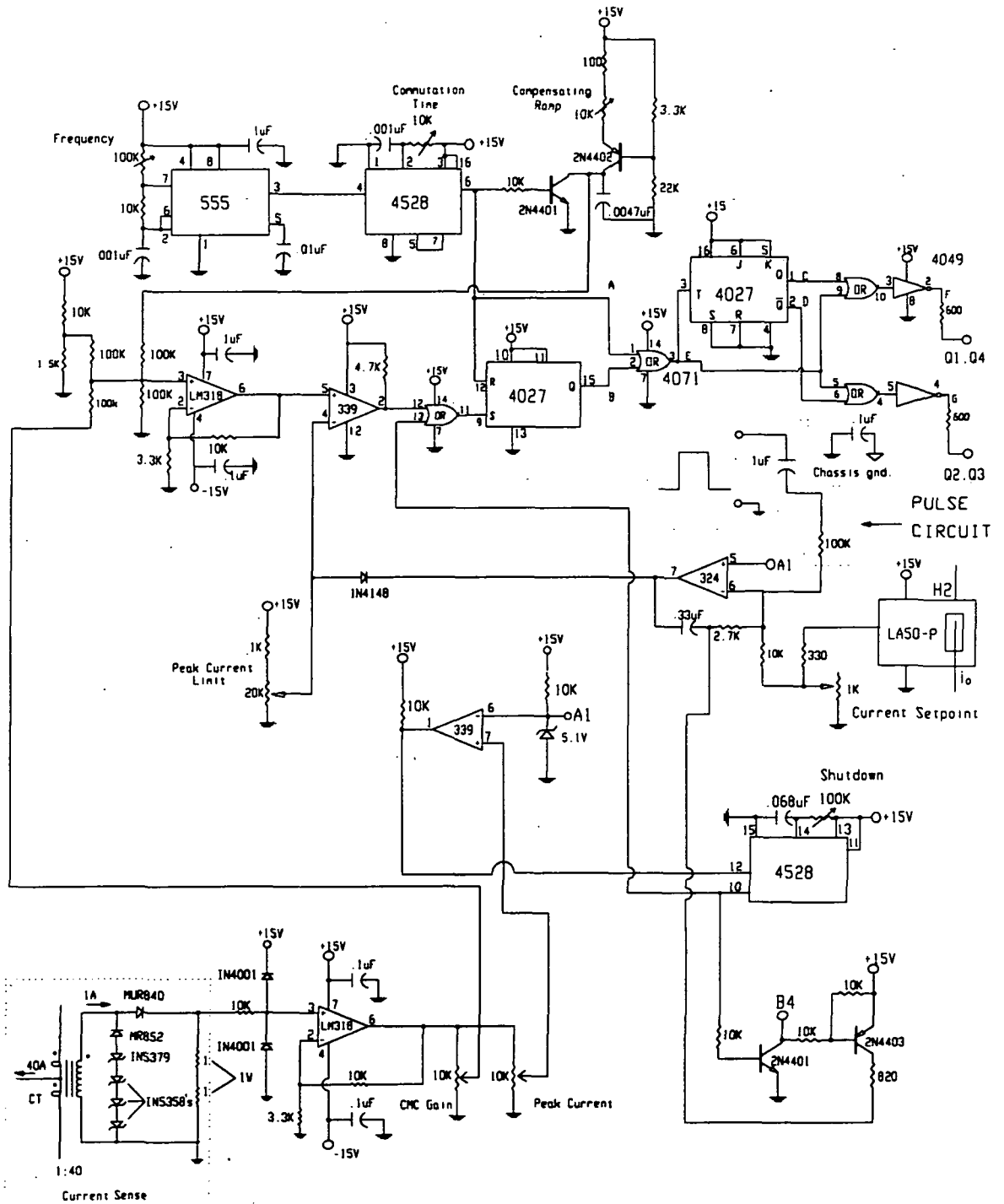Fig. 4.11(b) Simulator large signal transient response for $L_{out} = 2$ *mH*
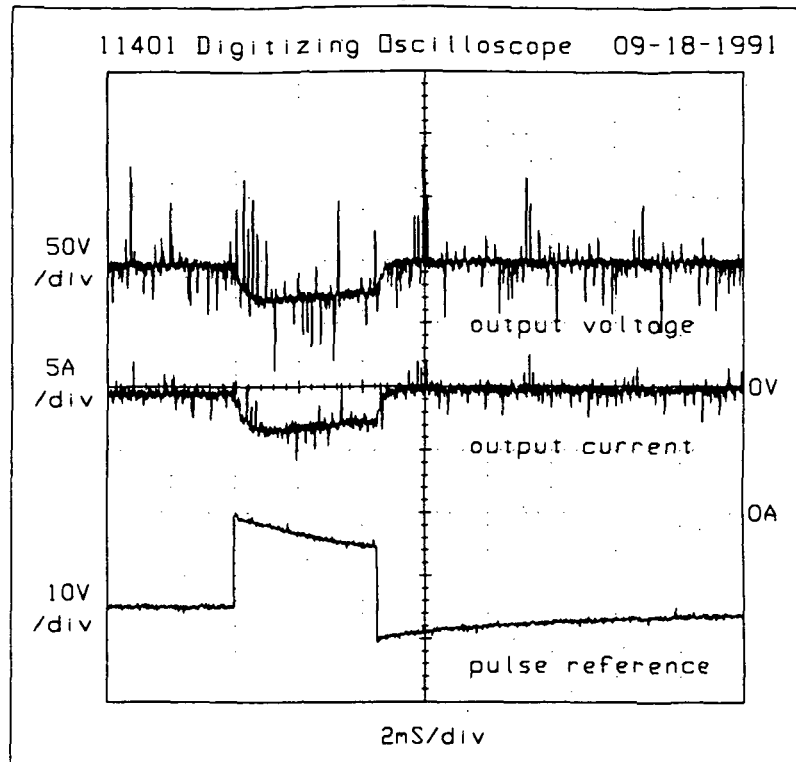
Fig. 4.12 CMC converter control and pulse injection circuitry

Fig. 4.13 Resistive load large signal transient response for $L_{out} = 2$ mH

useful application of the simulator arises in compensating the converter for use with an actual arcjet thruster.

4.6 LARGE SIGNAL TRANSIENT RESPONSE WITH $L_{out} = 384$ μH

The large signal transient response of the simulator tested with the CMC converter ($L_{out} = 384$ μH) is shown in Fig. 4.14. Unfortunately, no corresponding data was taken with the arcjet thruster.

A comparison of Figs. 4.14 and 4.11(b) reveals that the system is much more stable with an output inductance of 384 μH than one of 2 mH. It is known that the CMC converter loop gain is dependent upon the value of output inductance used [14]. Therefore, the converter should be compensated for the final value of output inductance
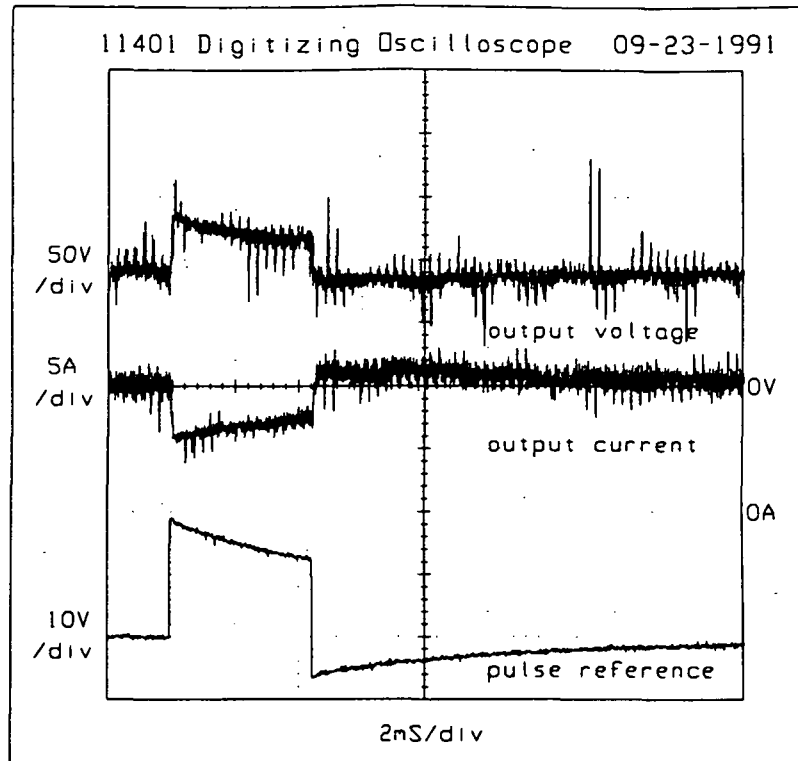
Fig. 4.14 Simulator large signal transient response for $L_{out} = 384$ μH

used.

With the exception of more ripple in Fig. 4.14 than in Fig. 4.11(b), the two figures are similar in all other aspects.

4.7 SIMULATOR EXTINCTION TRANSIENT

The simulator extinction transient was obtained by increasing the magnitude of the pulse waveform injected into the control circuit of Fig. 4.12 until simulator extinction was achieved. Using the Tektronix 11401 Digitizing Oscilloscope in the single trigger mode [9], the output voltage and current waveforms of Fig. 4.15 were recorded.

Fig. 4.15 shows that after the pulse occurs the simulator current and voltage approach a new equilibrium point. However, the new equilibrium point turns out to be
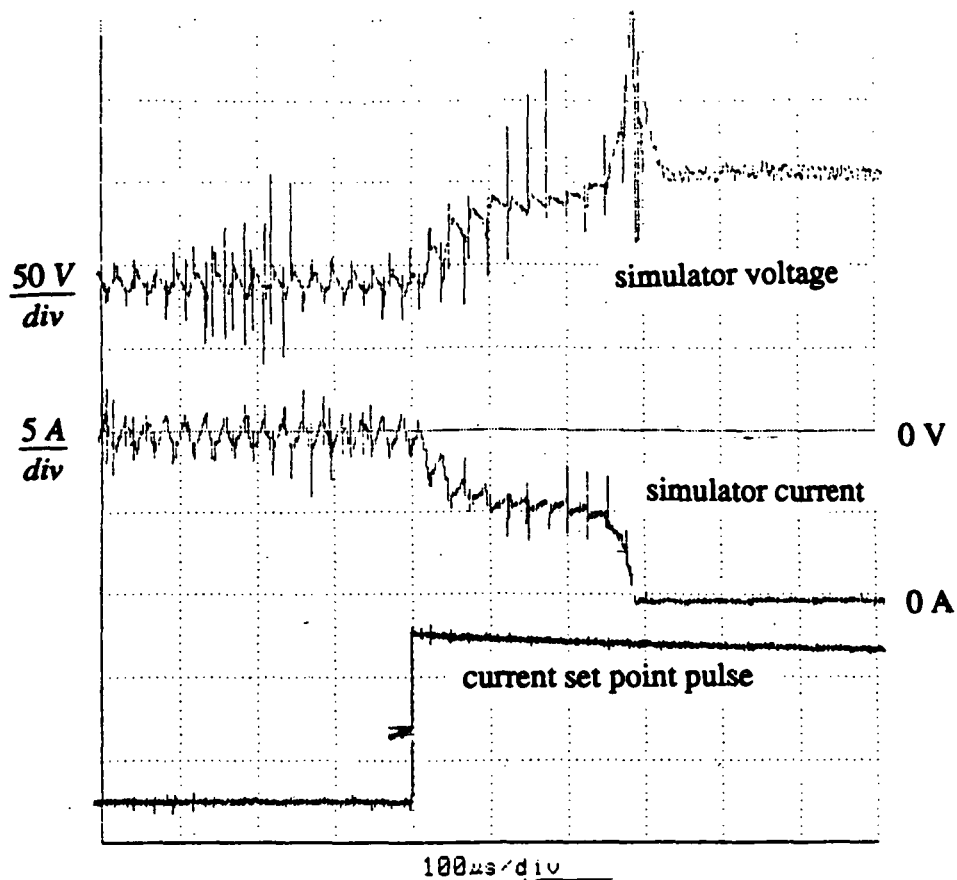
Fig. 4.15 Output voltage and current during simulator extinction

unstable and the simulator's current goes to zero and its voltage to the CMC converters open circuit value. Thus, the operating point jumps from I-V characteristic #2 to I-V characteristic #1 of Fig. 2.14. The large spike in the simulator voltage is caused by the rapid change in the current through L_{out} as the simulator current goes to zero.

Overall, the simulator extinction response seems to accurately predict the arc extinction response of an actual arcjet thruster.

Chapter 5

SUMMARY FOR PART I

5.1 DYNAMIC IMPEDANCE ADJUSTMENTS

As suggested in Chapter 4, another issue to be considered is how to make the dynamic impedance of the simulator adjustable, so that it can be made to more closely resemble that of an arcjet thruster. As mentioned in Chapter 2, the dynamic impedance of the simulator is equal to the slope of the tangent to the static I-V characteristic at a given operating point. Thus, by adjusting the static I-V curves the simulator dynamic impedance can be changed.

A simple way of doing this is by connecting a voltage feedback network to the positive terminal of the PI compensator op amp shown in Fig. 2.3. This network is shown in Fig. 5.1 where previously existing components are shown in dotted lines, and R1 and R5 represent the power potentiometer of Fig. 2.3.
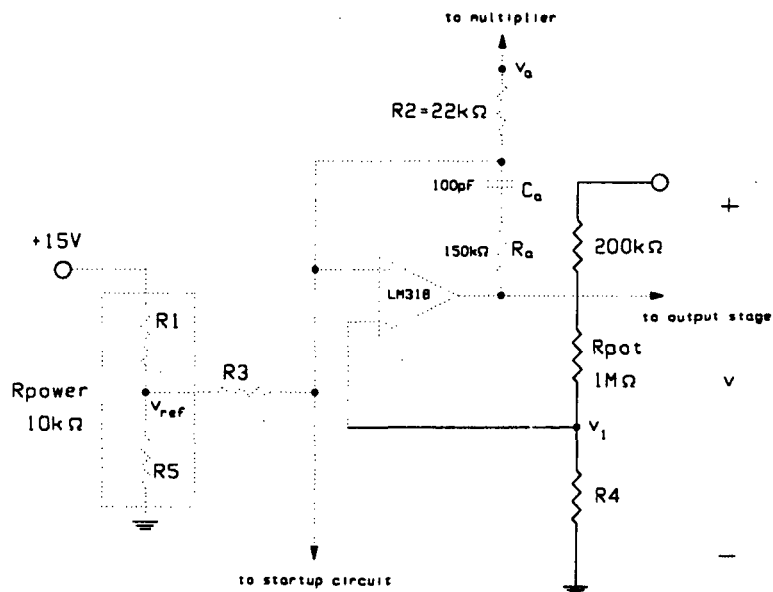

Fig. 5.1   Voltage feedback network used to adjust the simulator dynamic impedance

As stated in Chapter 2, for large signal, steady state operation, the compensation capacitor (C_a) of Fig. 5.1 will block current flow through its path. Thus, the large signal, steady state operation of Fig. 5.1 will be determined by,

$$\frac{v_{ref} - v_1}{R_3} = \frac{v_1 - v_a}{R_2} \qquad (5.1)$$

where v_1 is given by:

$$v_1 = v \cdot \frac{R_4}{R_{pot} + 200 \cdot 10^3 + R_4} \qquad (5.2)$$

Rearranging (5.1) yields:

$$v_{ref} = \left(1 + \frac{R_3}{R_2}\right) \cdot v_1 - \frac{R_3}{R_2} \cdot v_a \qquad (5.3)$$

Recalling from Chapter 2 that $v_a = -k_T \cdot i \cdot v$ (assuming that k_1, k_2 and k_3 of (2.1) are all zero) and that $R_3 = R_2$ (see Fig. 2.3), (5.3) can be reduced to:

$$v_{ref} = 2 \cdot v_1 + k_T \cdot i \cdot v \qquad (5.4)$$

Substituting (5.2) into (5.4) yields:

$$v_{ref} = \frac{2 \cdot R_4}{R_{pot} + 200 \cdot 10^3 + R_4} \cdot v + k_T \cdot i \cdot v \qquad (5.5)$$

Thus, the constant power I-V curves produced by (2.2a) are being altered by the addition of a term proportional to the simulator voltage (v), hence the term voltage feedback network for the circuit of Fig. 5.1.

By using the existing value of R3 (22 kΩ), setting R4 to 4.7 kΩ, and adjusting R_{pot} to 1 MΩ, in Fig. 5.1, static I-V characteristic (c), shown in Fig. 5.2 (where VF = Voltage Feedback), was obtained. For comparison, the static I-V characteristic of an arcjet (the middle curve of Fig. 1.2) and the previous I-V characteristic of the simulator without voltage feedback (curve #1 of Fig. 3.2) are shown in Fig. 5.2 as curves (a) and (b), respectively. Using the values of R3 and R4 mentioned above, and reducing R_{pot} yields
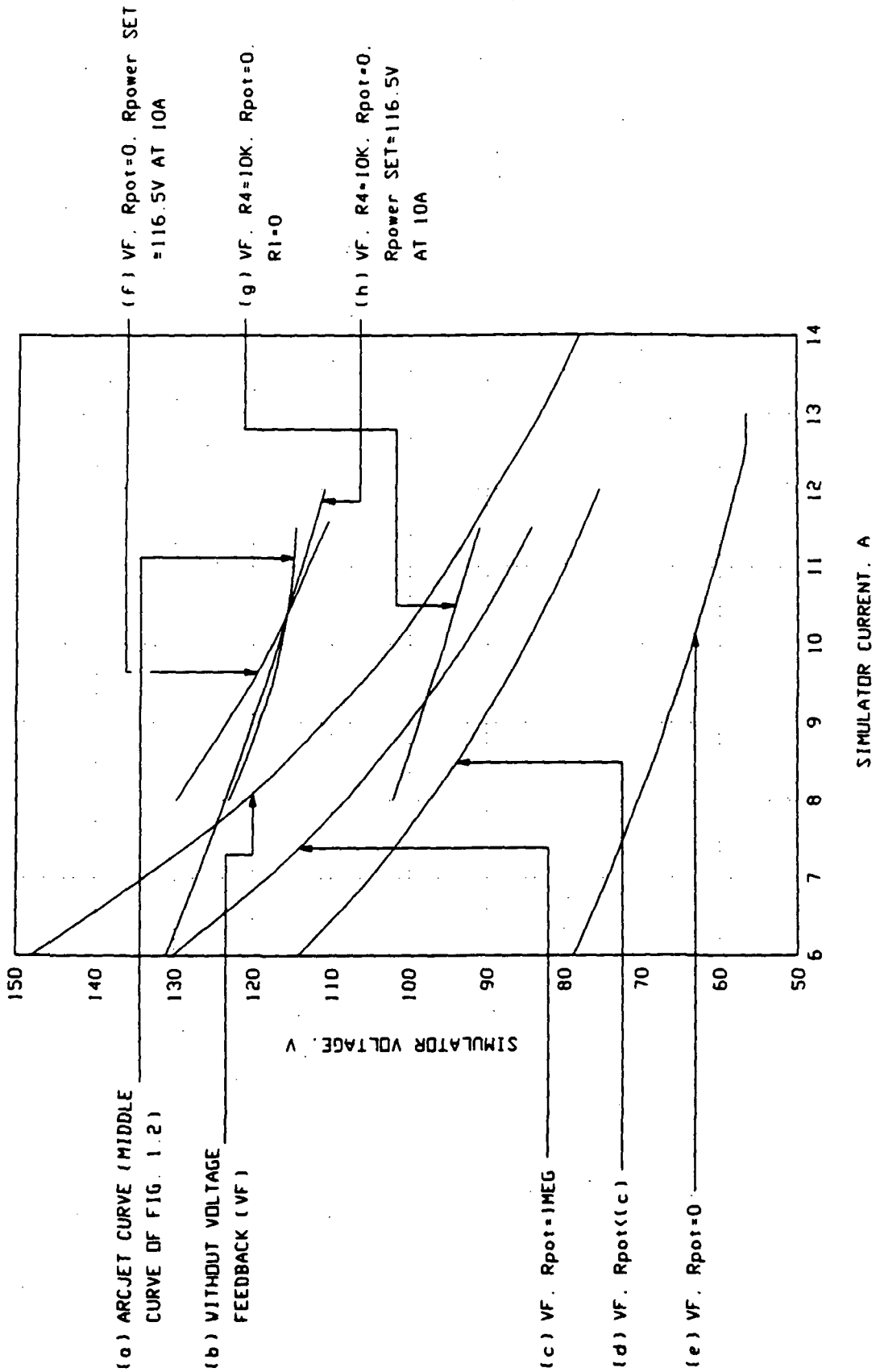
Fig. 5.2 Static I-V characteristics obtained using the voltage feedback network of Fig. 5.1

IV curve (d) of Fig. 5.2. Reducing R_{pot} to zero yields I-V curve (e).

Comparing Fig. 5.2 curves (a), (b) and (e) reveals that indeed the dynamic impedance of the simulator is being adjusted closer to that of the arcjet. However, curve (e) needs to be shifted away from the origin in order to achieve similar operating points as the arcjet curve (a). As discussed in Chapter 2 and demonstrated in Chapter 3, this can be accomplished by adjusting the power potentiometer of Fig. 2.3. Adjusting this potentiometer for an operating point of 116.2 V at 10 A (the approximate arcjet voltage of curve (a) at 10 A) results in I-V curve (f) of Fig. 5.2.

Comparing curves (a), (b) and (f) of Fig. 5.2 reveals that the simulator dynamic impedance has been decreased, but is still greater than that of the arcjet. These reductions have occured as the positive terminal voltage of the LM318, of Fig. 5.1, has been steadily increased by reducing R_{pot} towards zero. Thus, further dynamic impedance reductions can be made by increasing R4 and again adjusting R_{pot} towards zero. Changing R4 to 10 $k\Omega$, adjusting R_{pot} to zero and adjusting the power potentiometer (R_{power}) to its maximum value (such that R1=0 in Fig. 5.1) yields I-V curve (g) of Fig. 5.2. Examination of this curve reveals that it has a dynamic impedance very close to that of the arcjet curve (a). However, curve (g) must be shifted away from the origin to achieve similar operating points as (a), and the power potentiometer (R_{power}) is already set to its maximum value. However, by changing R3 to 10 $k\Omega$ the range of R_{power} can be extended. Thus, by adjusting R_{power} for an operating point of 116.8 V at 10 A, curve (h) of Fig. 5.2 was obtained.

Comparing curves (a) and (h) of Fig. 5.2 reveals close agreement between the I-V characteristics (and therefore the dynamic impedance) of the arcjet and simulator, especially in the range of 8 - 10.5 A.

Note that by letting,

$$k_3 = \frac{2 \cdot R_4}{R_{pot} + 200 \cdot 10^3 + R_4}$$

(5.5) can be rearranged to yield:

$$v = \frac{v_{ref}}{k_3 + k_T \cdot i} \qquad (5.6)$$

which is the same as (2.1b) (repeated here for convenience) with $k_1 = k_2 = 0$:

$$v = f_S(i) = \frac{v_{ref} - k_1 - k_2 \cdot i}{k_3 + k_T \cdot i} \qquad (5.7)$$

Thus, the same results achieved by the voltage feedback network of Fig. 5.1 could also be achieved by manipulating the multiplier offset potentiometers so that k_3 of (2.1b) is varied while $k_1 = k_2 = 0$. This could be accomplished by varying the I offset pot of Fig. 2.3.

If in addition to k_3, k_1 and k_2 are also varied (by varying the P and V offset pots of Fig. 2.3), the degree of freedom available in matching the simulator I-V characteristics to those of the arcjet will increase. However, since this will involve the adjustment of three potentiometers it is suggested that a curve tracer be employed to give a continuous trace of the simulator static I-V characteristic as each pot is varied, so that the best approximation to the desired I-V curve can be rapidly found.

5.2 OTHER APPLICATIONS

One application of interest is in the area of welding power supply testing. As illustrated in Fig. 2.15, the I-V characteristic of a welding arc is similar to that of the simulator shown in Fig. 2.14.

Using the techniques of the previous section along with a change in R_D of Fig. 2.3, the simulator static I-V curve can be made to closely resemble that of a given welding arc.

In this way the simulator could be used as a load when testing welding power supplies .

Another possible application of interest concerns the simulation of switching converters in solar power systems testing (such as the case discussed in [15]). When a switching converter is in regulation the current will decrease (increase) for a corresponding increase (decrease) in voltage such that its output power remains constant. Thus, while in regulation the switching converter follows a constant power I-V characteristic. When the switching converter voltage gets sufficiently low the converter will drop out of regulation and behave as a resistive load. Thus, as given in [15], the I-V characteristics of a regulated switching converter are as shown in Fig. 5.3.
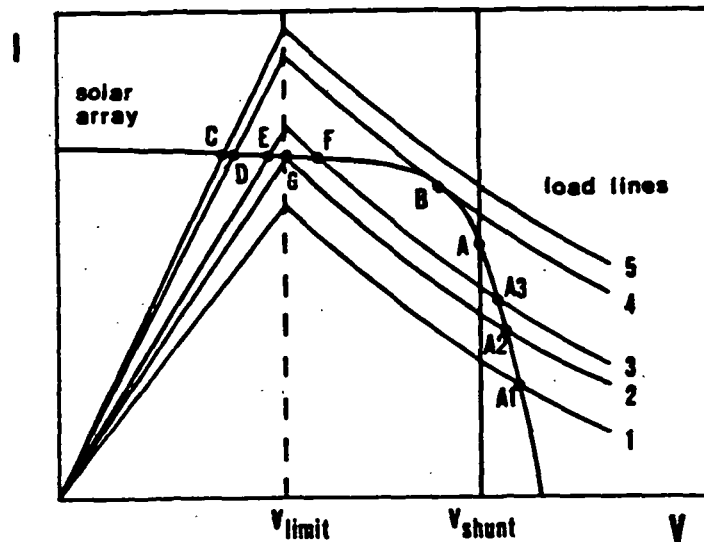

Fig. 5.3 I-V characteristics of a regulated switching converter (load lines 1-5)
(Source: [15])

It has already been shown that the simulator can reproduce the constant power portion of the I-V characteristic shown in Fig. 5.3. By changing the sign of the multiplier (switching the current sense leads on the emitter resistor) and of the DC voltage applied to the power potentiometer of Fig. 2.3, the straight line portion of the simulator I-V

characteristic shown in Fig. 2.14 can be made to resemble that of the switching converter shown in Fig. 5.3

By using the techniques of section 5.1 and the appropriate value of R_D, the simulator I-V characteristic can be made to closely resemble the input characteristic of a switching converter having a constant load. Thus, in this way the simulator could be used to simulate actual switching converters when testing solar power systems.

In short, the simulator has possible applications in any situation where the load current increases (decreases) with decreasing (increasing) voltage.

5.3 SIMULATOR LIMITATIONS

As shown in Figs. 3.9-3.11 the simulator upper cutoff frequency is limited to approximately 40-60 kHz depending on operating point. (Remember that the upper cutoff frequency has been defined in this study as the frequency at which the phase of the dynamic impedance varies from its low frequency value by 45 degrees.) The limited arcjet data obtained from [4] suggests that the arcjet also has an upper cutoff frequency of approximately 40-60 kHz. Therefore, it appears that the upper cutoff frequency of the simulator is comparable to that of the arcjet. However more arcjet data should be obtained before this result is verified. For most applications the simulator upper cutoff frequency should be large enough to include the source ripple frequency, which for this case is 40 kHz.

Due to a lack of mathematical equations describing arcjet behavior and a lack of sufficient arcjet experimental data to compare with simulator results, the extent to which the simulator matches the large signal dynamics of an actual arcjet remains relatively unknown.

The ignition pulse created by the ignition circuit of Fig. 4.3 will be in the range of 1-2 kV. Therefore, the ignition circuit and simulator were not tested together as such testing would require very high voltage simulator devices. Thus, the simulator should not be used for ignition circuit testing.

5.4 CONCLUSION

The simulator as developed herein has been shown to produce I-V characteristics which closely resemble those of an arcjet thruster, thereby demonstrating its ability to be used as a load device in determining the stability of converters designed for arcjet applications. In addition, the simulator has been shown to be a fairly accurate predictor of actual arcjet performance. Since the system (the converter and its load) loop gain has been shown to be dependent on the type of load used, another useful application of the simulator arises in compensating the converter for use with an actual arcjet thruster. It has also been shown that the simulator can be constructed in the laboratory using relatively inexpensive power electronic components.

The stability of various arcjet supply arrangements has been demonstrated by proving that the internal resistance of the arcjet supply converter must be greater in magnitude than the dynamic resistance of the simulator to achieve a stable, non-zero current, operating point.

The static and dynamic impedances of the simulator were shown to agree closely with results obtained from an actual arcjet thruster. In addition, simulator performance was determined by testing the simulator with a current mode controlled (CMC) converter and comparing the results with those of an arcjet tested on the same converter. The data obtained showed close agreement between simulator and thruster performance.

Methods of varying the simulator dynamic impedance so that it would more

closely resemble that of an arcjet thruster, or some other device, have also been discussed. Finally, it has been shown that the simulator may have applications in other areas, such as in testing power supplies for welding or for the simulation of switching converters in testing solar power systems.

PART II

ARCJET IGNITION CIRCUIT DEVELOPMENT

Chapter 6

INTRODUCTION

Fig. 6.1 shows the 1kW converter power circuit which was developed in [12]. The gate drivers, gate drive current booster, current mode controller (CMC), diagonal to phase-shift conversion logic, and CMC Hall effect current sensor are shown in Figs. 6.2-6.6, respectively. All of this circuitry was developed as part of the study described in [12], and the circuit details are described in that reference. The ignition circuit is shown in Fig. 6.7, and its theory of operation is described in the next chapter.
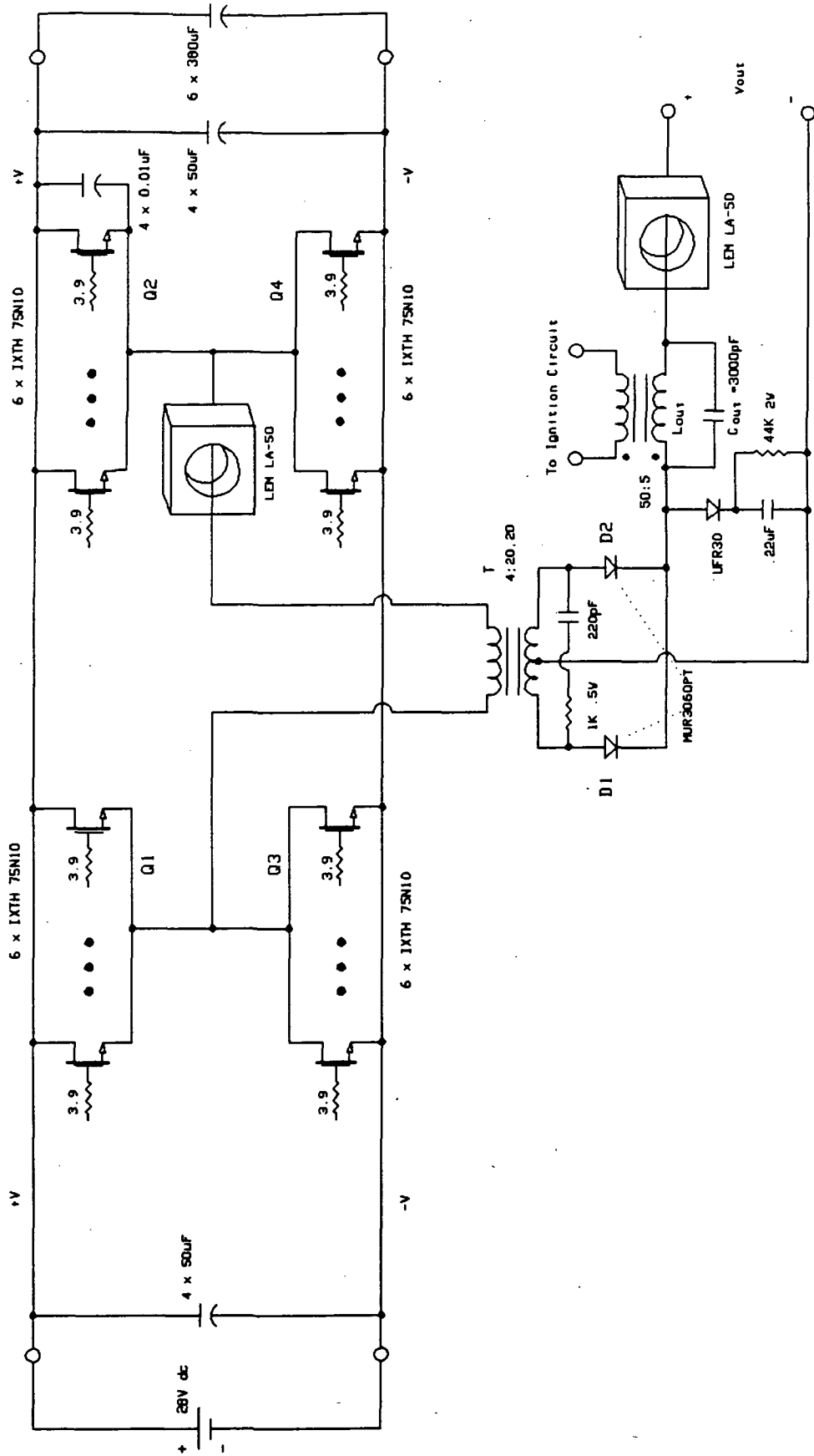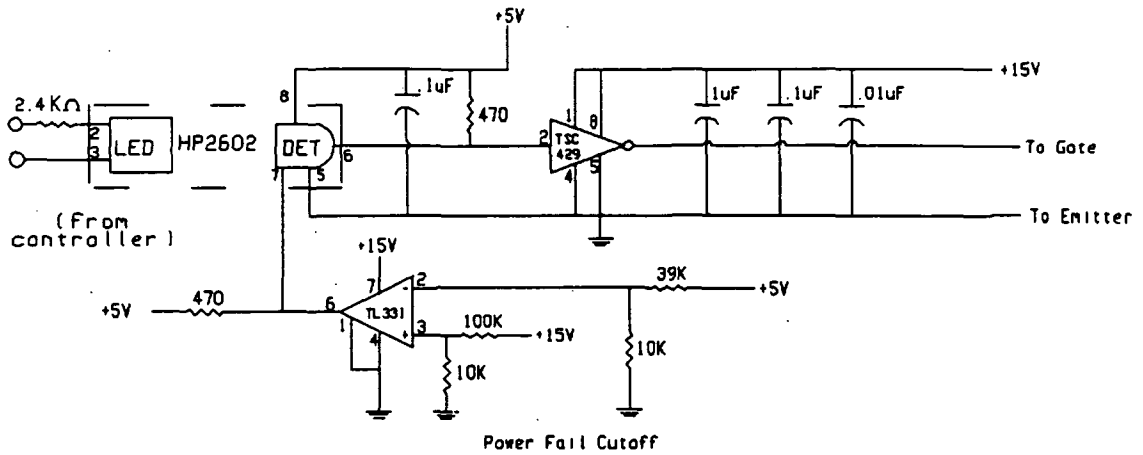
Fig. 6.1 1-KW converter power circuit
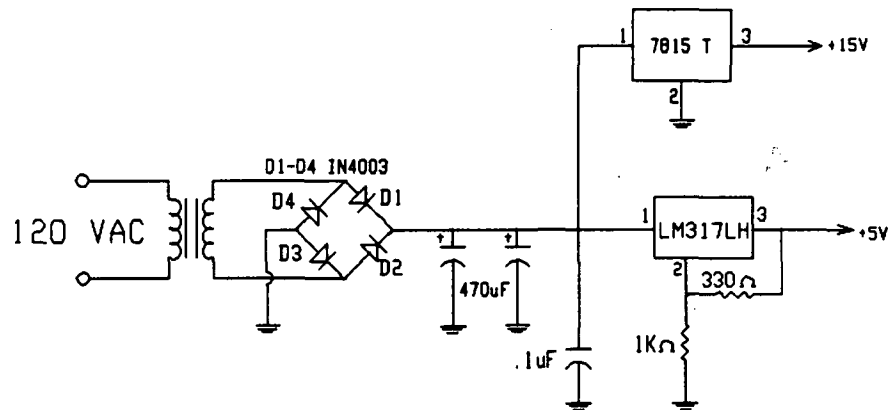
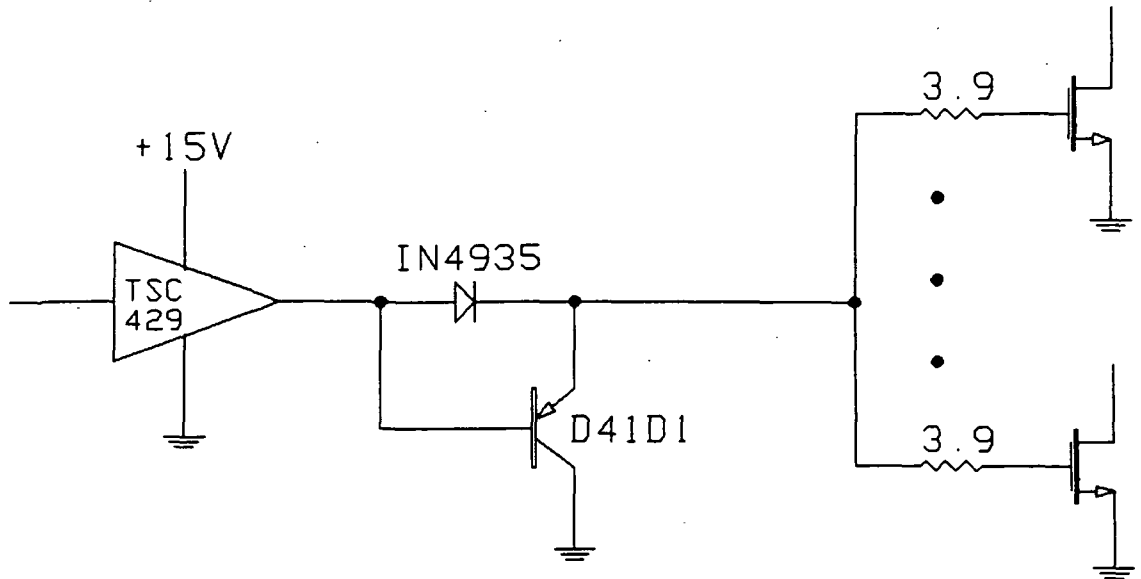Fig. 6.2. Isolated gate drive circuit with power-fall cutoff.
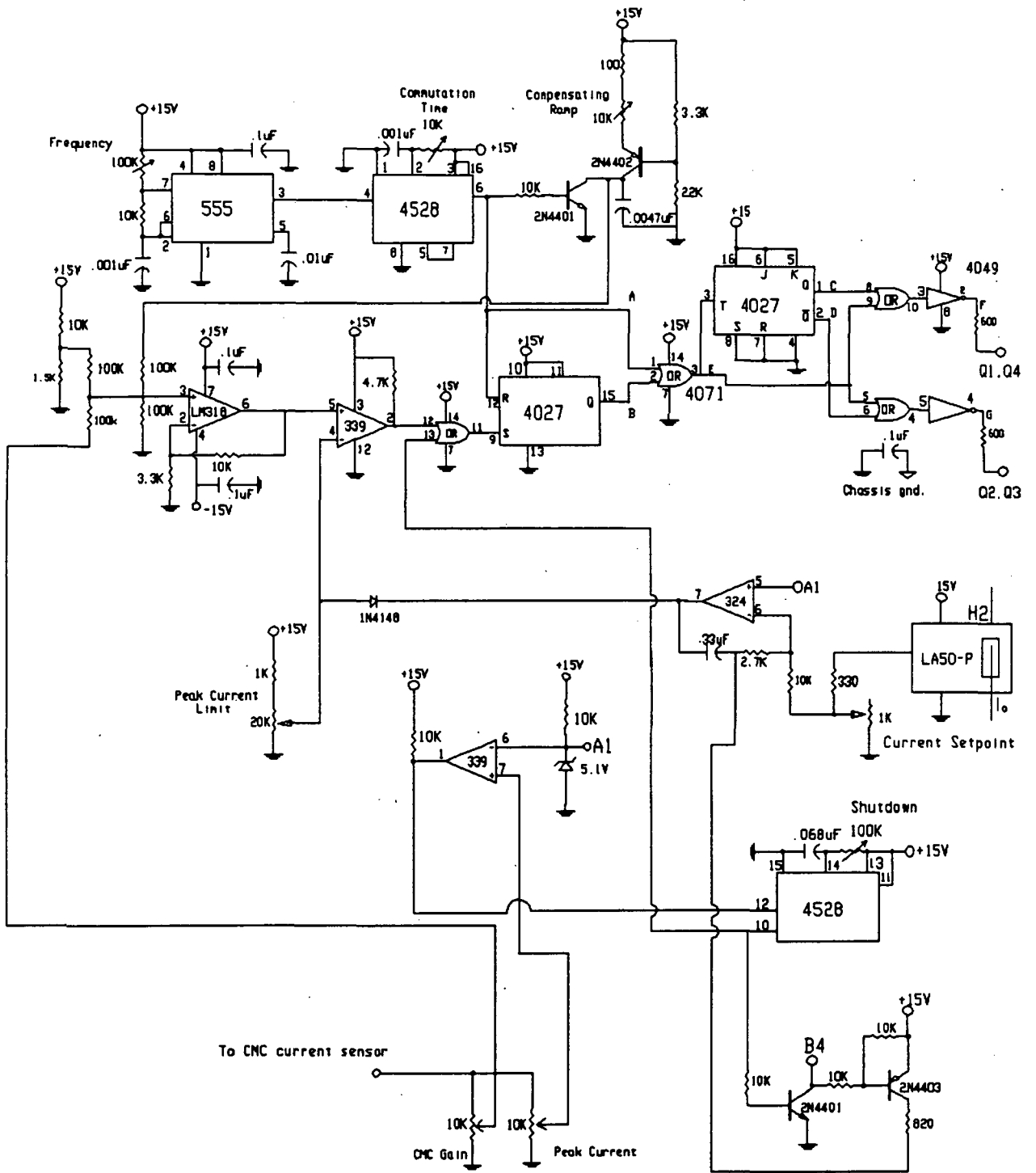
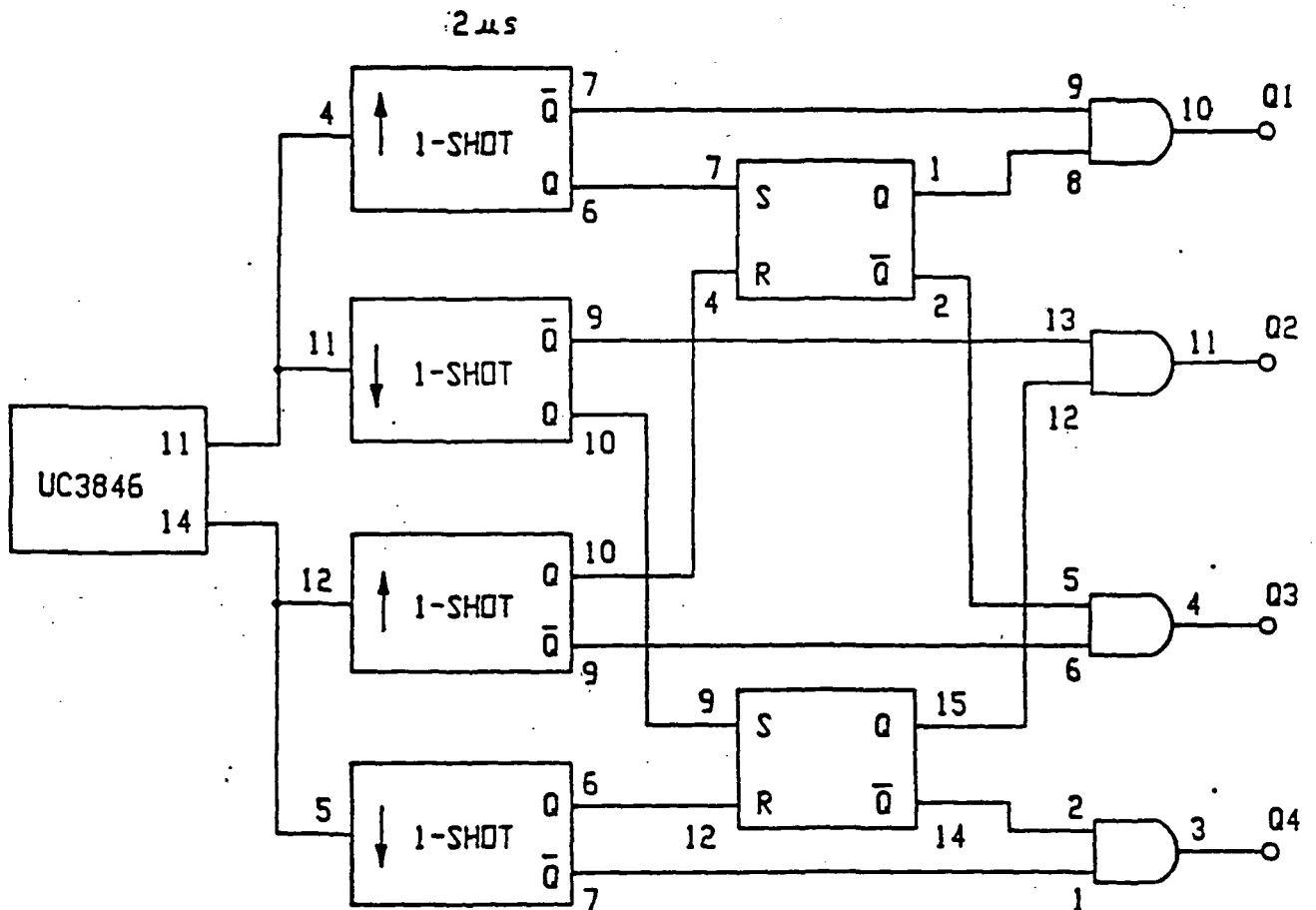Fig. 6.3 Gate drive current booster.

Fig. 6.4 Current Mode Controller

Fig. 6.5 Logic for converting diagonal gating waveforms
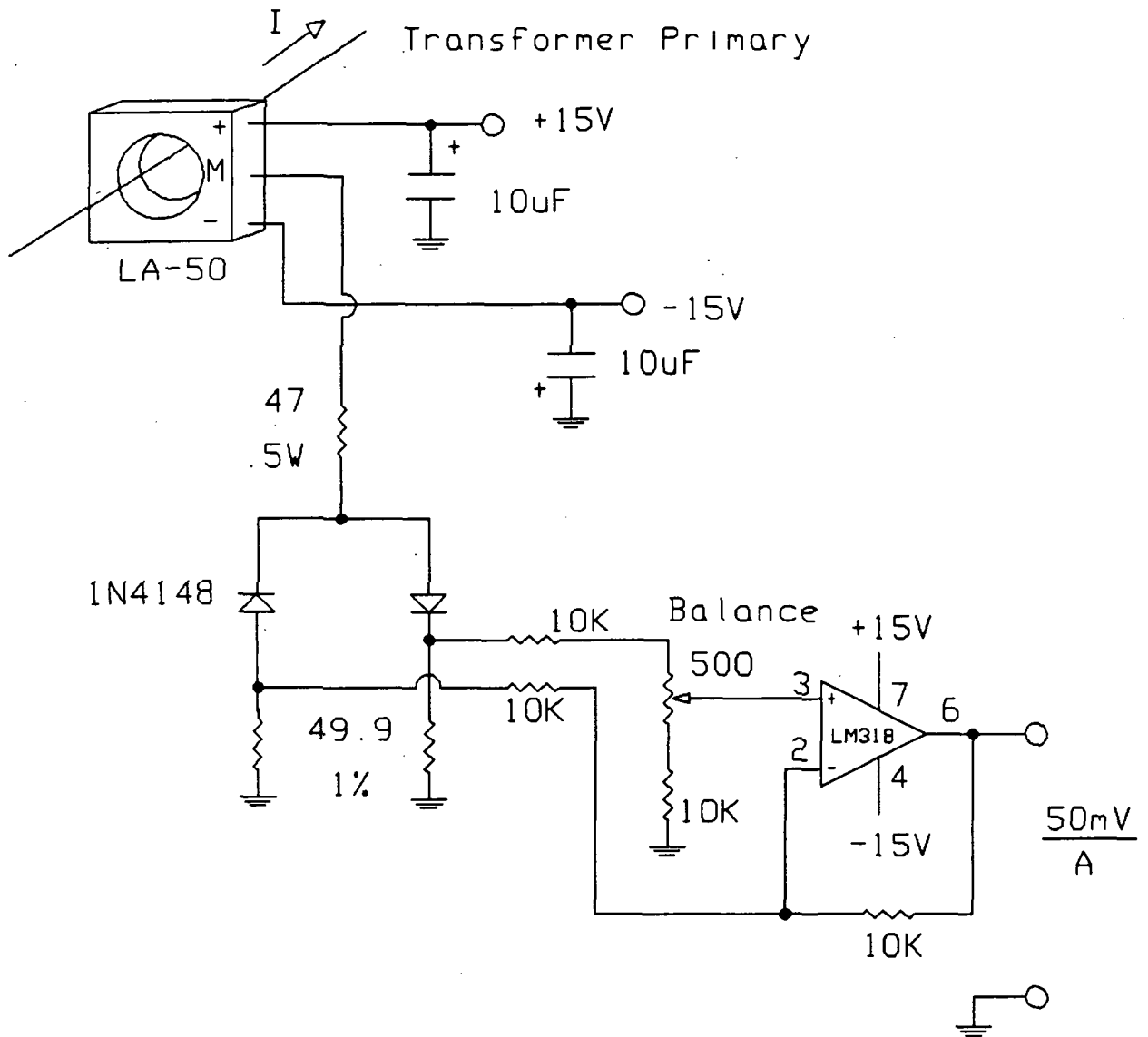to phase-shift gating waveforms.

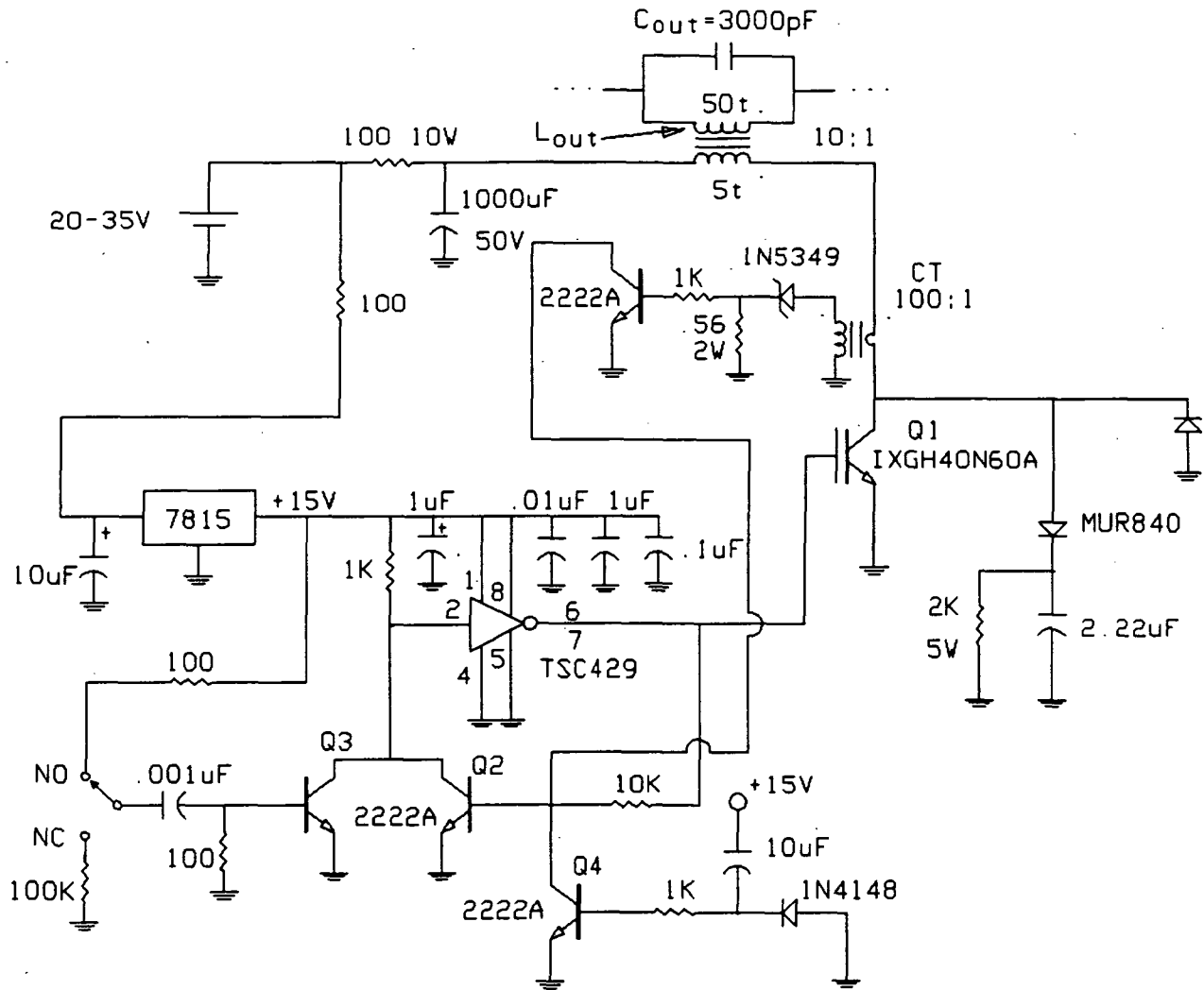Fig. 6.6   CMC sensor using a Hall-device dc current sensor.

$C_{out} = 3000pF$

50t.

L_{out}

10:1

100 10V

5t

20-35V

1000uF

50V

1N5349

CT
100:1

2222A   1K

56
2W

Q1
IXGH40N60A

7815   +15V   1uF   .01uF 1uF

.1uF

MUR840

10uF

1K

1
2   8

6
7

.1uF

TSC429
5

2K

5V

2.22uF

100

NO

.001uF

Q3

Q2

10K

+15V

NC

2222A

10uF

100K

100

Q4

2222A   1K

1N4148

Fig. 6.7 Ignition circuit.

Chapter 7

THEORY OF OPERATION FOR IGNITION CIRCUIT

This arcjet ignition circuit is shown in Fig. 6.7. This circuit is designed to operate from the primary input voltage to the arcjet converter, in the range of 20-35 V, and provide a consistent ignition pulse to the arcjet. The converter output inductor is provided with a closely-coupled extra winding through which energy is introduced to this inductor to form the ignition pulse. When an ignition command is received by the control portion of the circuit, the IGBT is turned on, allowing the current in the extra inductor winding to ramp up to a predetermined set point, at which time the IGBT is turned off. This begins an interval in which the inductor primary voltage rises resonantly to the breakdown voltage of the arcjet. Assuming enough energy is initially stored in the inductor, an initial current is established in the arcjet corresponding to an arc voltage below the open-circuit voltage of the arcjet converter. This permits the current in the inductor to rise to the point at which the converter current-regulation loop takes control of the converter. The circuit of Fig. 6.7 is similar to that of [13] in most respects, and was derived from it.

The control portion of the ignition circuit uses a TSC 429 gate-driver to gate Q1, the IGBT. This gate driver is made self-latching by the addition of Q2. An "off" state for this latch is assured upon power-up by Q4 and its associated circuitry. An ignition pulse is manually triggered by the NO/NC push button shown, together with Q3. An externally-commanded ignition pulse could be coupled in through an opto-isolator at this point.

An ignition command sets Q1's latching gate driver, allowing the current in the extra winding on inductor L_{out} to ramp up at a rate determined by the primary input voltage. This ramping current is sensed by the current transformer and Q5, and when it reaches its set point the gate driver is reset by Q5. Because a current set

point is used instead of a fixed inductor-charging time, a consistent amount o

energy is stored in the inductor regardless of varying supply voltage. Upon tur

off of Q1, the inductor voltage rises sinusoidally, the resonance being determined b

the 2.22 µF capacitor in parallel with the IGBT and the 3000 pF on the inductor mai

winding. When break over of the arcjet occurs at the angular time "Θ" at the natura

resonant frequency, an initial current equal to the charging-current set point time

cos Θ , reflected through the inductor turns ratio, is established in the arcjet. (It i

generally found that cos Θ is close to one for practical purposes in this design.) It i

then expected that the arcjet supply converter will establish an appropriat

operating point for the arcjet before the energy stored in the inductor is dissipated.

The open-circuit voltage produced by the ignition circuit is equal to its se

point current multiplied by the characteristic resistance of the resonant circui

approximately 3.4 kV with a 2-mH output inductor. Should ignition fail to occur, th

diode in anti-parallel with Q1 allows the return of the stored energy to the 1000 µF

supply capacitor, and reset of the ignition circuit.

The method used here is to initially ignite the arc with a high voltage puls

and then sustain the steady state arc with a current source. This process can b

explained as follows. The simplified power circuit is shown in Fig. 7.1. S is initiall

closed, and i_1 ramps up to some value I_1, at which time S is opened. The reflecte

value of I_1 is I_p, which is the initial value of i_L. The equivalent circuit for this perio

is shown in Fig. 7.2, and waveforms for v_o and i_L with no arc are shown in Fig. 7.3. A

v_o increases, the voltage across the arc gap travels along the vertical axis from O to l

in Fig. 7.4 until ignition occurs at $v_o = V_I$. As the arc is established, i_o begins to flow

and the operating point moves to the v_o vs. i_o curve for the arc at some point B. N

attempt is made to model the exact behavior of v_o vs. i_o during ignition, but v_o wil

quickly decrease as the energy stored in L_o is dissipated by the arc. Thus th

operating point will move down the v_o vs. i_o curve as vo decreases. The curren

regulated converter now has a 100% duty cycle since i_o has not yet reached the I_o reg

regulation value. After the operating point passes point C, the converter will remain

at 100% duty because $i_o < I_o$ reg As io continues to increase beyond point C, v_o will

continue to decrease as the output operating point moves down the arc curve. The

voltage difference, $v_s - v_o$, appears across L_o. I_o reg represents the regulated current

value that is controlled by the current feedback loop. Because of the delay caused by

the response time of this loop, io proceeds past Io reg at point D and on to Io max

which is the absolute open loop limit fixed by the controller. When io reaches Io max

at point E, the converter begins to operate in the PWM mode to limit $i_o = I_o$ max. As the

current control loop begins to respond, the duty cycle will decrease to reduce $i_o = I_o$

reg, and the steady state operating point will move back to D.

The simplified circuit in Fig. 7.5 provides an explanation as to why a current

regulated supply should be used instead of a voltage regulated supply. As seen from

Fig. 7.4, at least over part of its operating range, the arc can be approximately

modelled by a nonlinear $R_{(io)}$ and va(i_o) in series. Therefore vo will drop as io

increases. If voltage regulation is used, the equivalent source resistance, R_1, is quite

small and $R_1 - R_{a(io)} < 0$, which is an unstable condition. If current regulation is used,

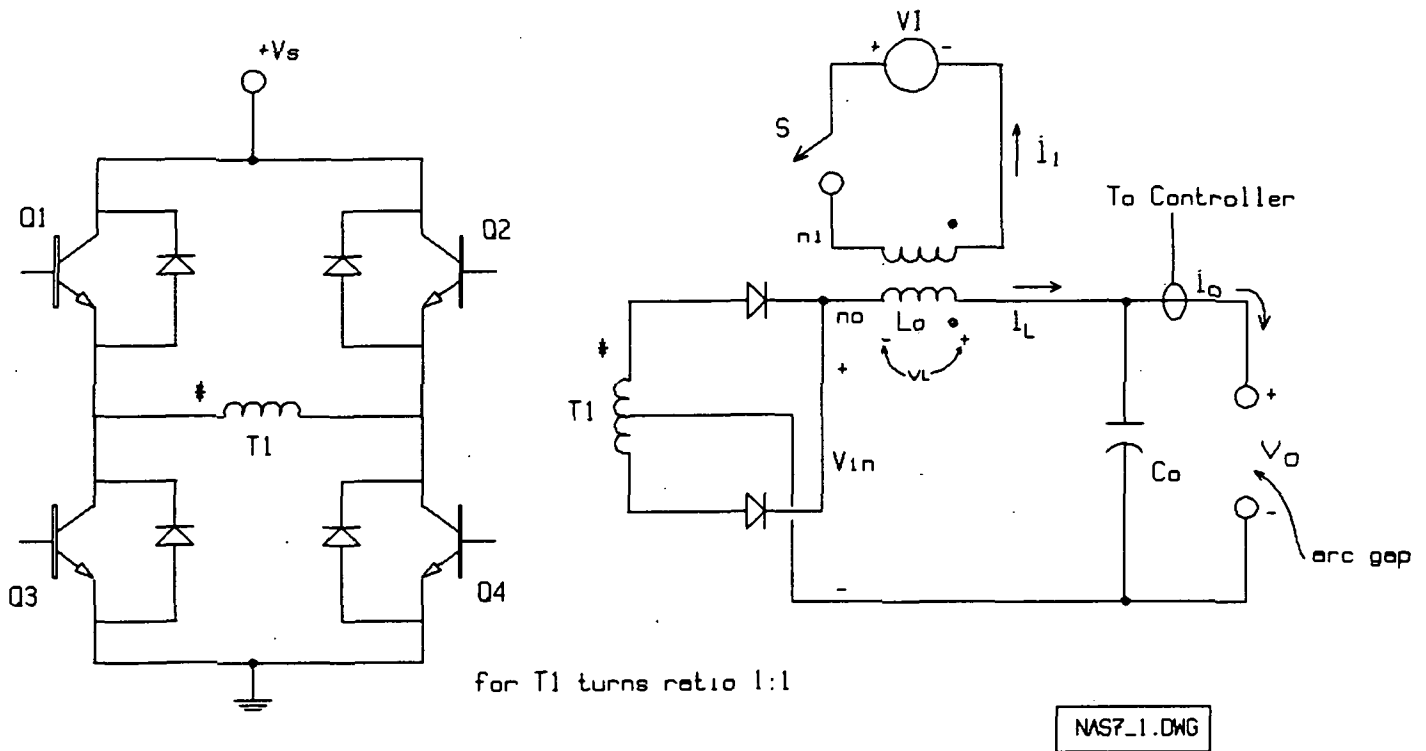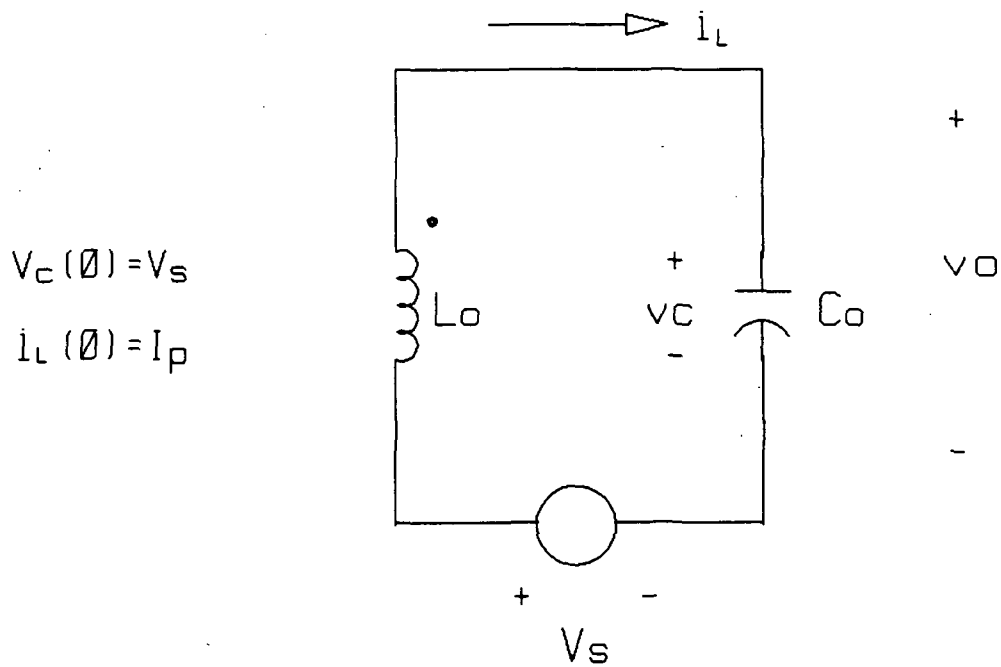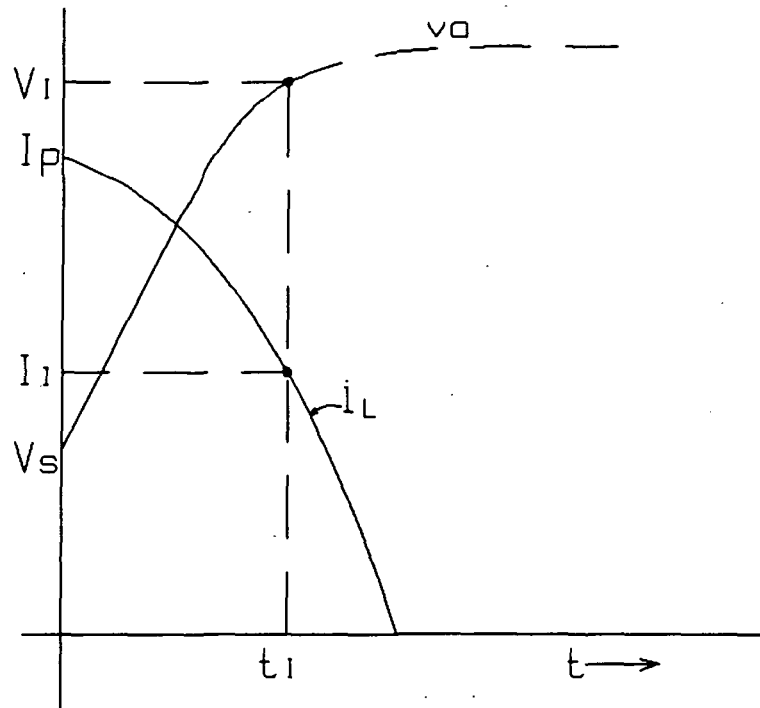R1 is very large and $R_1 - R_a$ (io) > 0, which provides stability.

for T1 turns ratio 1:1

NAS7_1.DWG

Fig. 7.1. Simplified power circuit

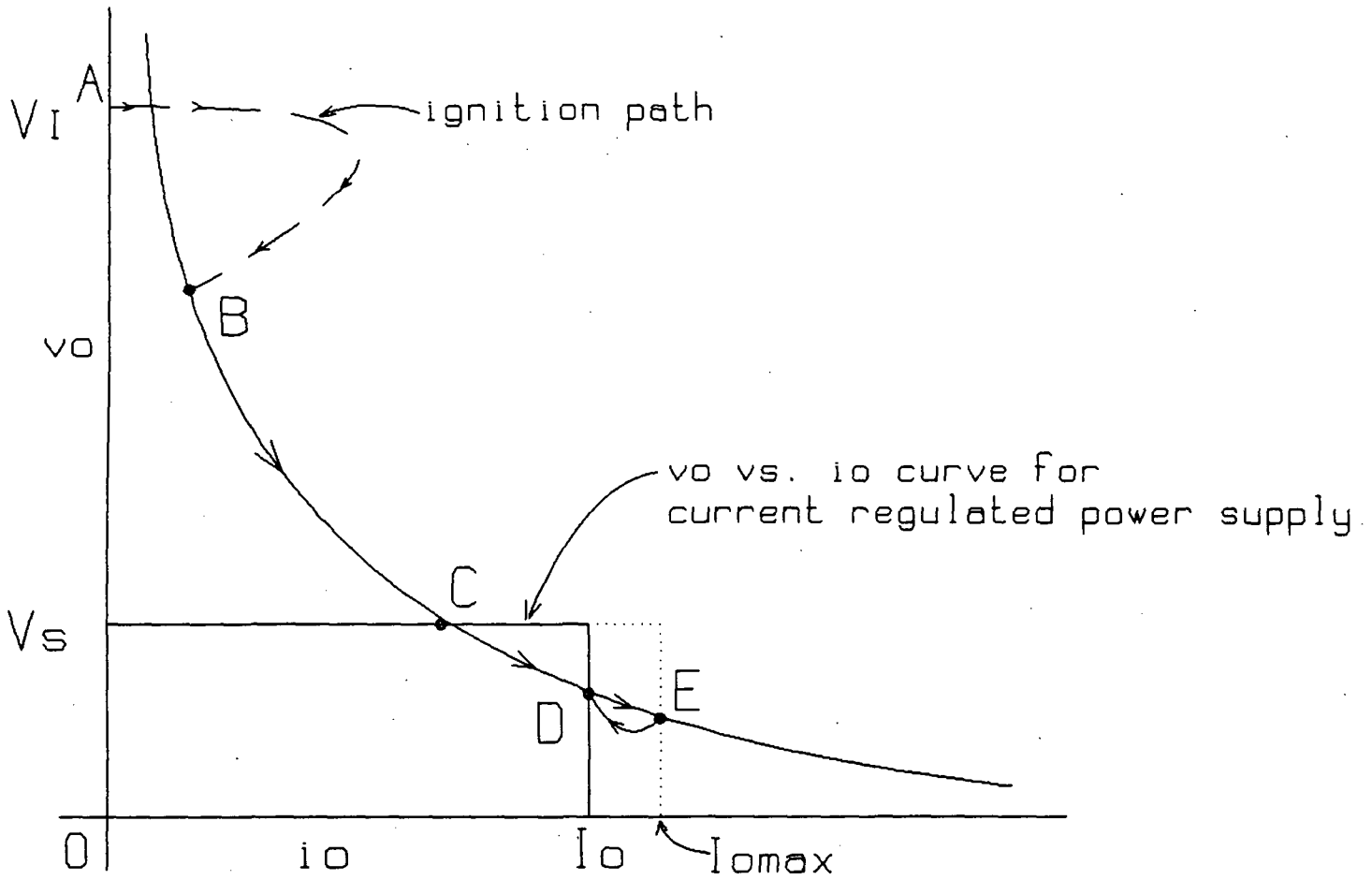Fig. 7.2. Equivalent circuit after S
open ๐ t=Ø and before ignition.

NAS7_3.DWG

for $0 \leq t \leq t_I$

$$V_o = V_s + I_p \sqrt{\frac{L_o}{C_o}} \ \sin wt \ , \quad w = \frac{1}{\sqrt{L_o C_o}}$$
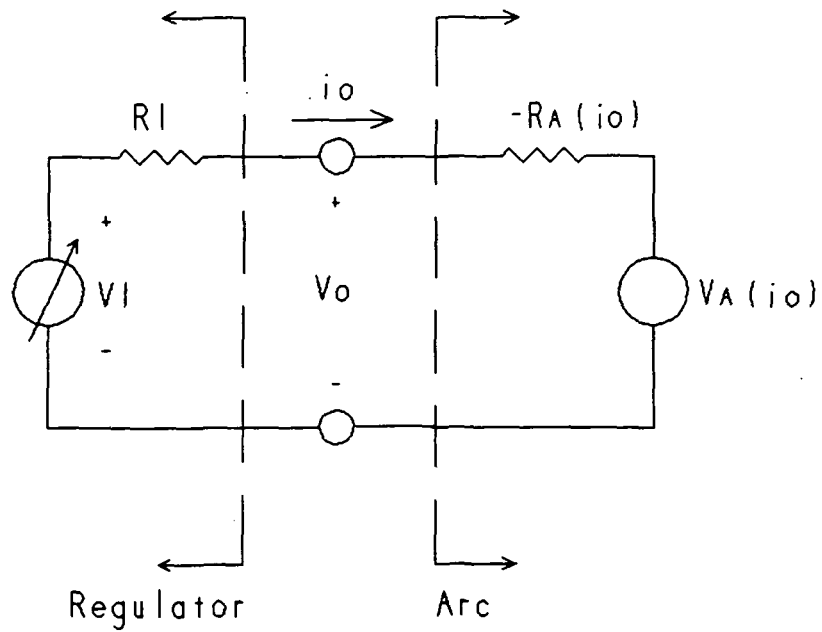
$$i_L = I_p \cos wt$$

V_I , I_I = voltage and current at ignition point.

Fig. 7.3. V_o and i_L without arc.

Fig. 7.4. Simplified characteristic curves for arcjet and power supply.

Fig. 7.5. Simplified equivalent circuit for regulator and arc.

Chapter 8

EXPERIMENTAL RESULTS

To verify the operation of the converter and ignition circuits, a series of tests were performed at the NASA Lewis Research Center where the power supply was operated with an arcjet load.

Fig. 8.1 shows the open circuit ignition pulse without the 100 V. output and with $Lo = 2mH$. Fig. 8.2 shows the pulse under the same conditions but with the arcjet. An expanded view is shown in Fig. 8.3.

Fig. 8.4 shows v_o and i_o at ignition with the peak current limit set at about 40A. Fig. 8.5 shows these same waveforms but with an expanded voltage scale. This peak value of 40A. was judged to be excessive and raised some concern about damage to the arcjet nozzle. Therefore, the peak current limiter setting was lowered, and Figs. 8.6 and 8.7 show the results for peak limits of about 12.5A. and 21 A., respectively. Fig. 8.8 shows the steady state ripple in v_o and i_o, while Fig. 8.9 shows the response of v_o and i_o to a step change in the current reference voltage.

In an effort to save weight, it would be advantageous to reduce the size of the output filter choke, but there is some concern that ignition may not occur if the choke is too small. This concern is based on the fact that a smaller choke will sustain the ignition pulse for a shorter period of time. To investigate the behavior with a smaller choke, a series of tests were performed using a 384 μH choke in place of the original value of 2mH. The resulting waveforms are shown in Figs. 8.10-8.12. Fig. 8.10 shows that the ignition pulse is now in excess of 4kV, and ignition occurs in about 1.25 μs. Fig. 8.2 indicates that with the 2 mH choke ignition occurred at about 1.5 kV and within about 3.75 μs. Both chokes appeared to be satisfactory since the arc was ignited numerous times with each choke, and no ignition failures were observed. Fig. 8.11 shows the output voltage and current ripple. The output voltage and current

after ignition with I limit $\approx$ 25 A. peak are shown in Fig. 8.12. The peak values of v_0 and i_0 in Fig. 8.12 are considerably lower than those in Fig. 8.10 since the limited sampling rate of the digital storage oscilloscope apparently missed the peak values when used on the longer time scale.
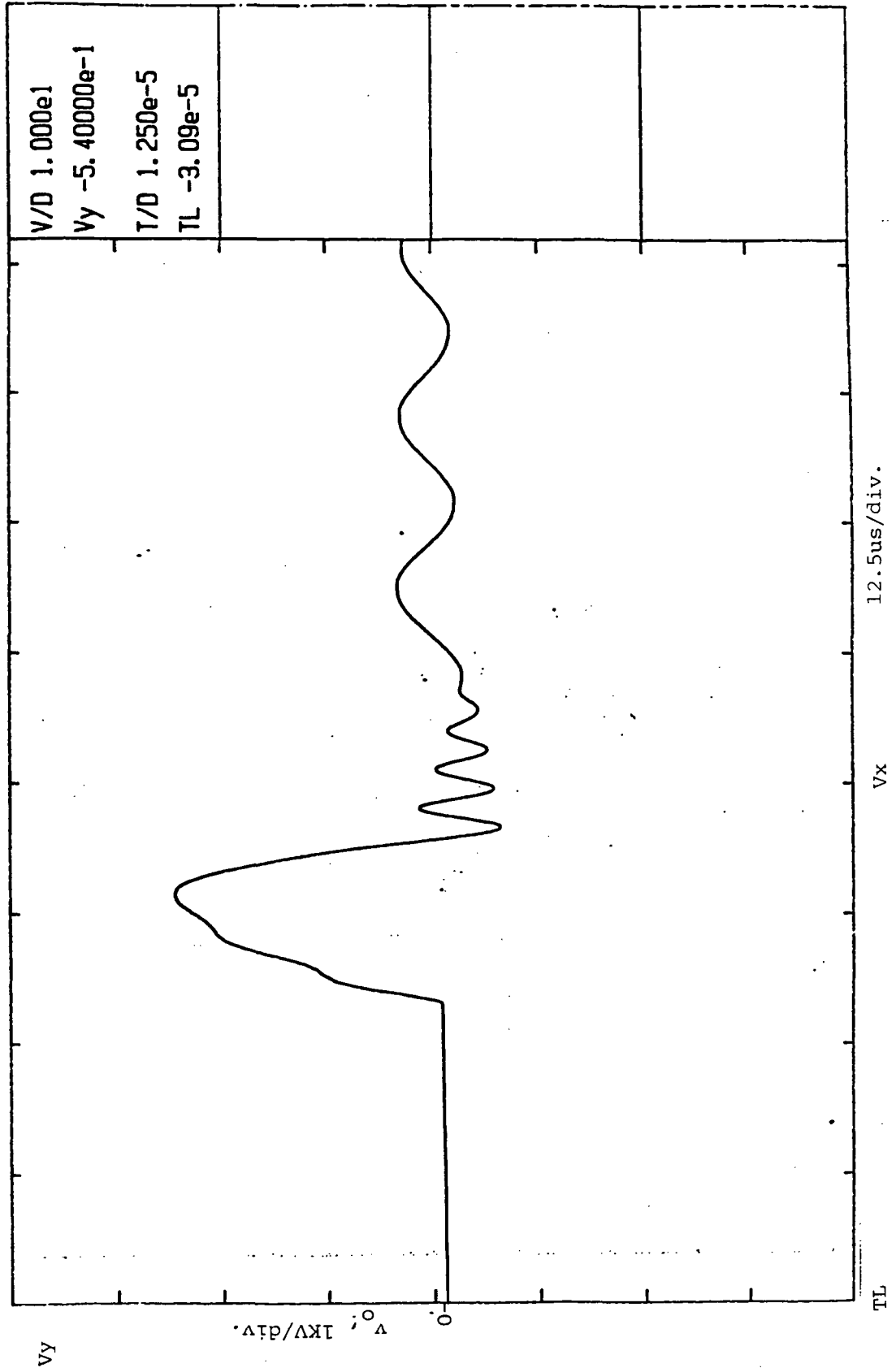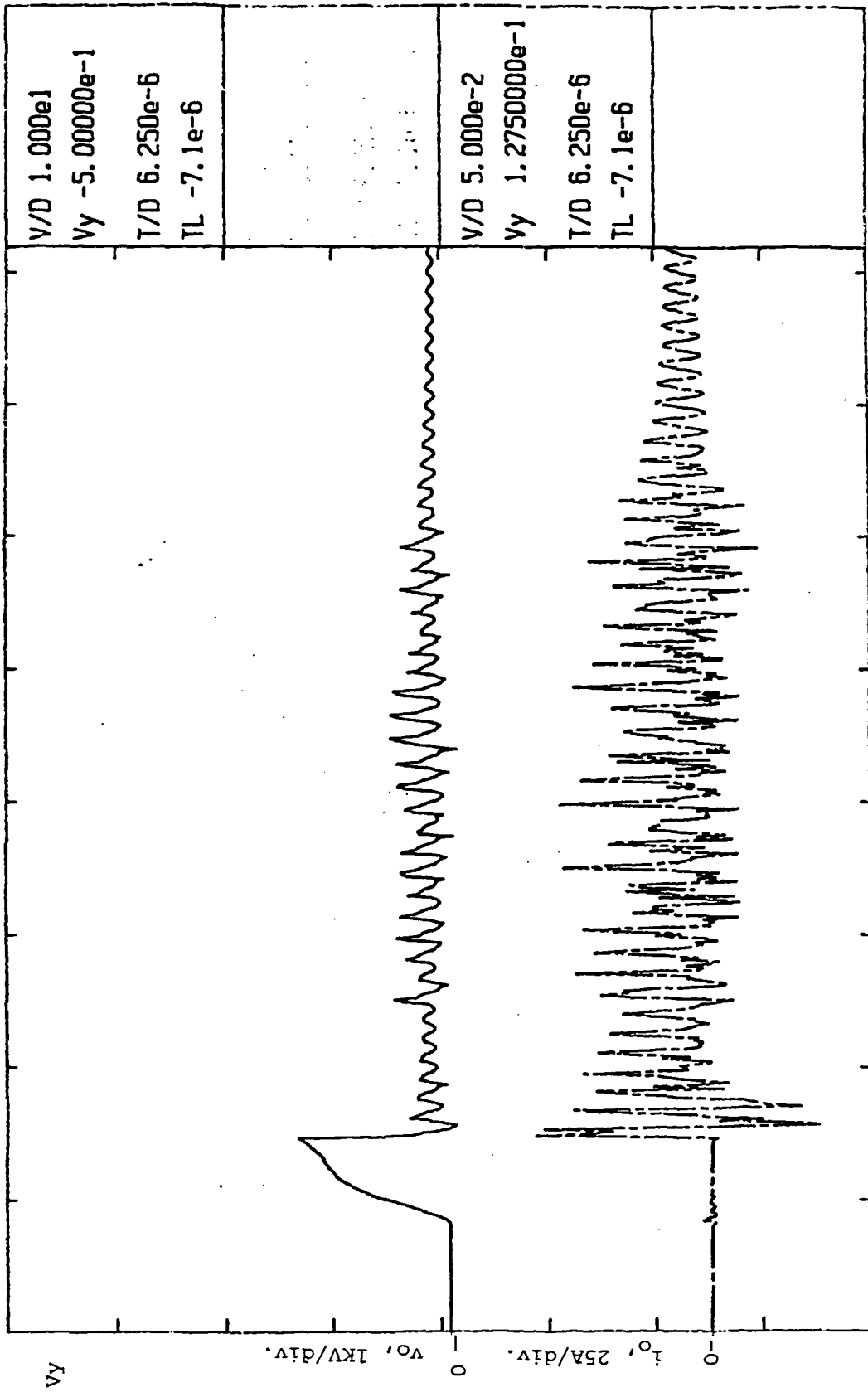
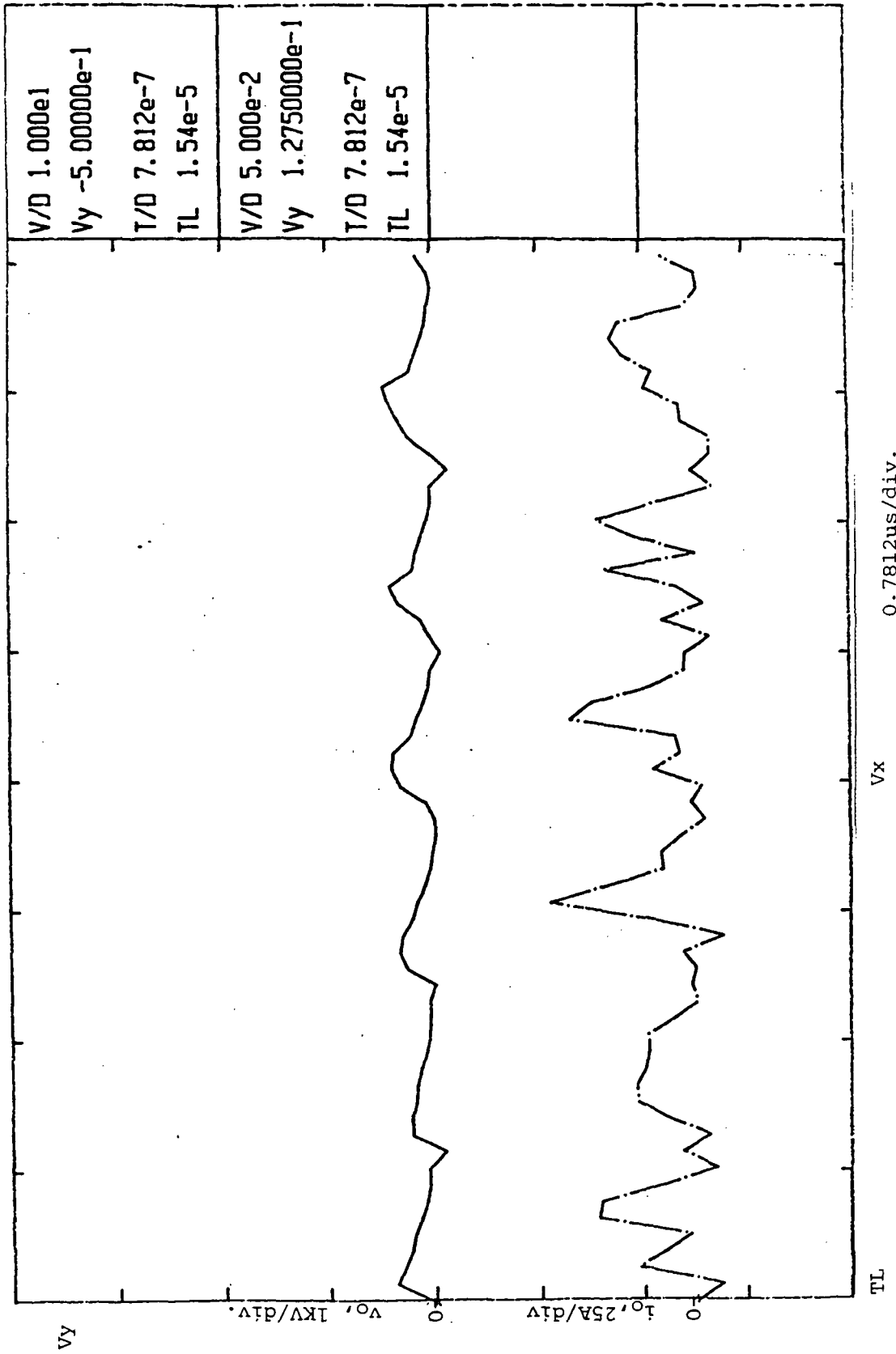Fig. 8.1. Ignition pulse without arcjet and 100Vdc turned off (Lo = 2 mH).

| V/D 1.000e1 |
| Vy -5.00000e-1 |
| T/D 6.250e-6 |
| TL -7.1e-6 |

| V/D 5.000e-2 |
| Vy 1.2750000e-1 |
| T/D 6.250e-6 |
| TL -7.1e-6 |

Vy

Vo, 1KV/div.

io, 25A/div.

Vx   6.25us/div.

TL

Fig. 8.2. Ignition pulse with arcjet, but 100Vdc turned off.

Fig. 8.3. Expanded view of Fig. 8.2, 15.4us after initial pulse.

| V/D 1.000e1 |
| Vy -4.00000e-1 |
| T/D 5.00e-4 |
| TL -2.555e-4 |
| V/D 5.000e-2 |
| Vy 1.2770000e-1 |
| T/D 5.00e-4 |
| TL -2.555e-4 |

v_o, 1KV/div.

i_o, 25 A/div.

Vy

0

Vx   500us/div.

TL
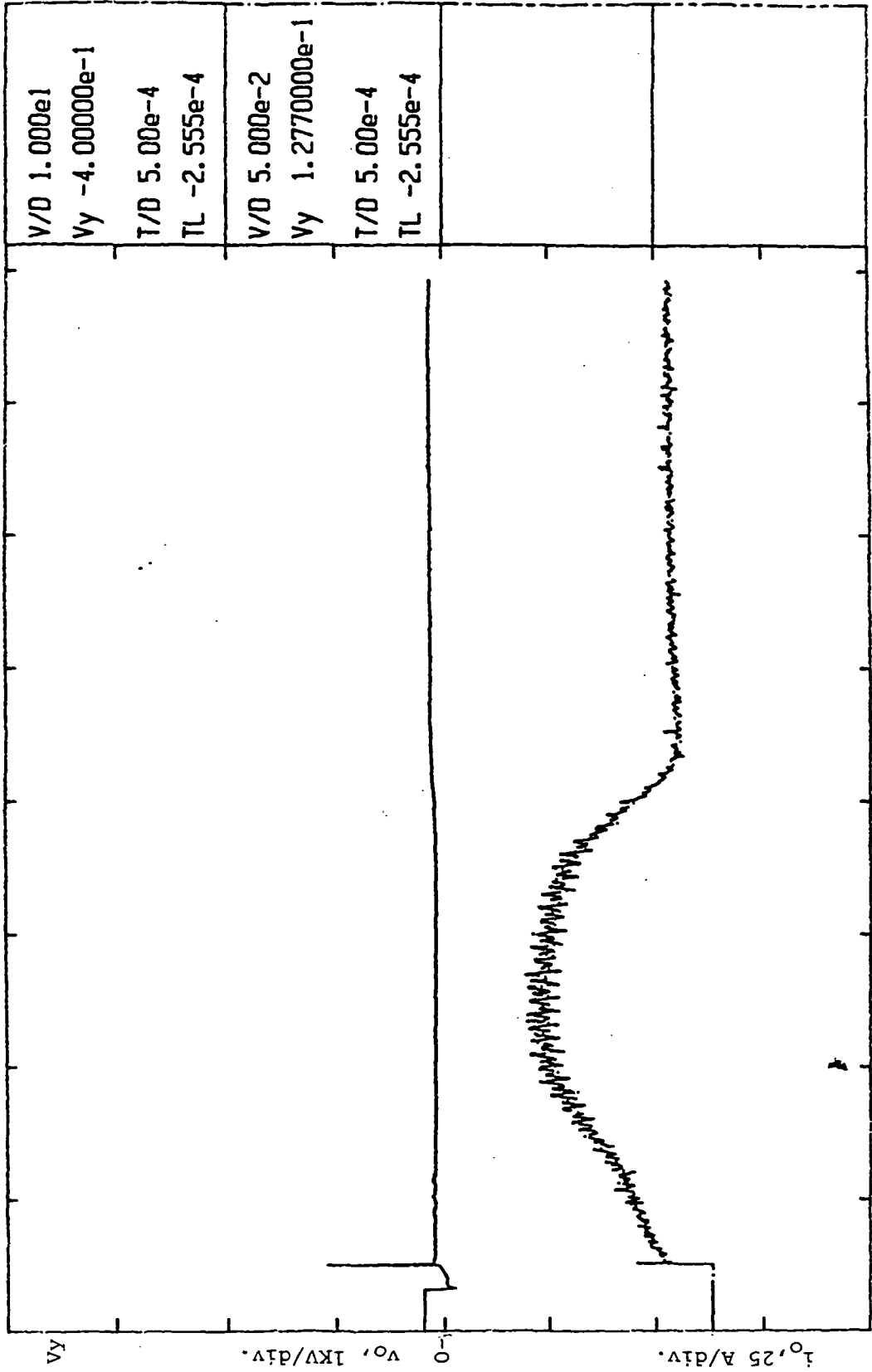
Fig. 8.4. vo and io at ignition with $I_{limit} \cong 40$ A. peak.

C-2

V/D 5.000e-1	V/D 5.000e-2
Vy -1.50000e-2	Vy 1.2780000e-1
T/D 5.00e-4	T/D 5.00e-4
TL -2.555e-4	TL -2.555e-4

Vy

v_o, 50V/div.

i_o, 25A/div.
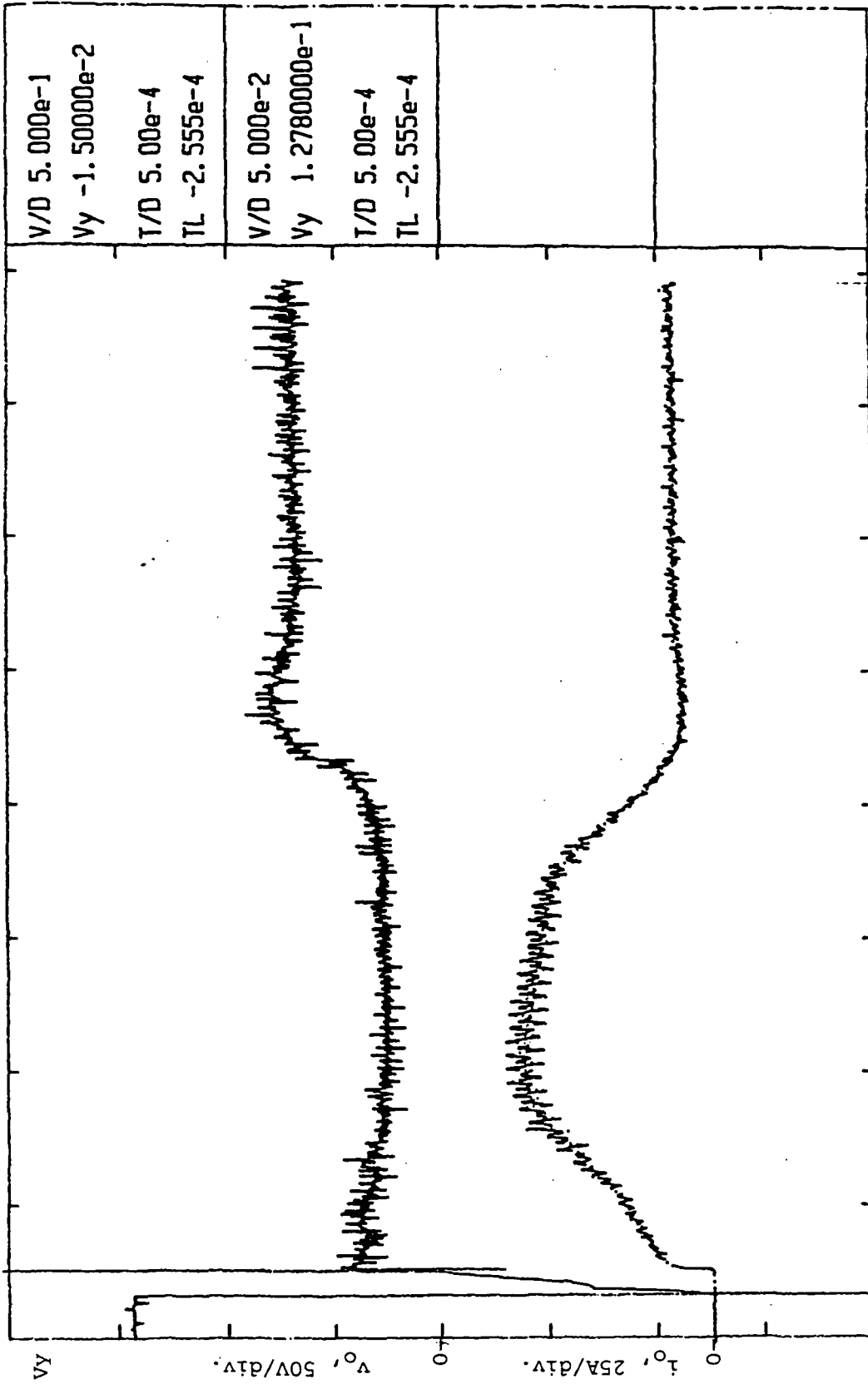
Vx

500us/div.

TL

Fig. 8.5. Same as Fig. 8.4 but with expanded voltage scale.

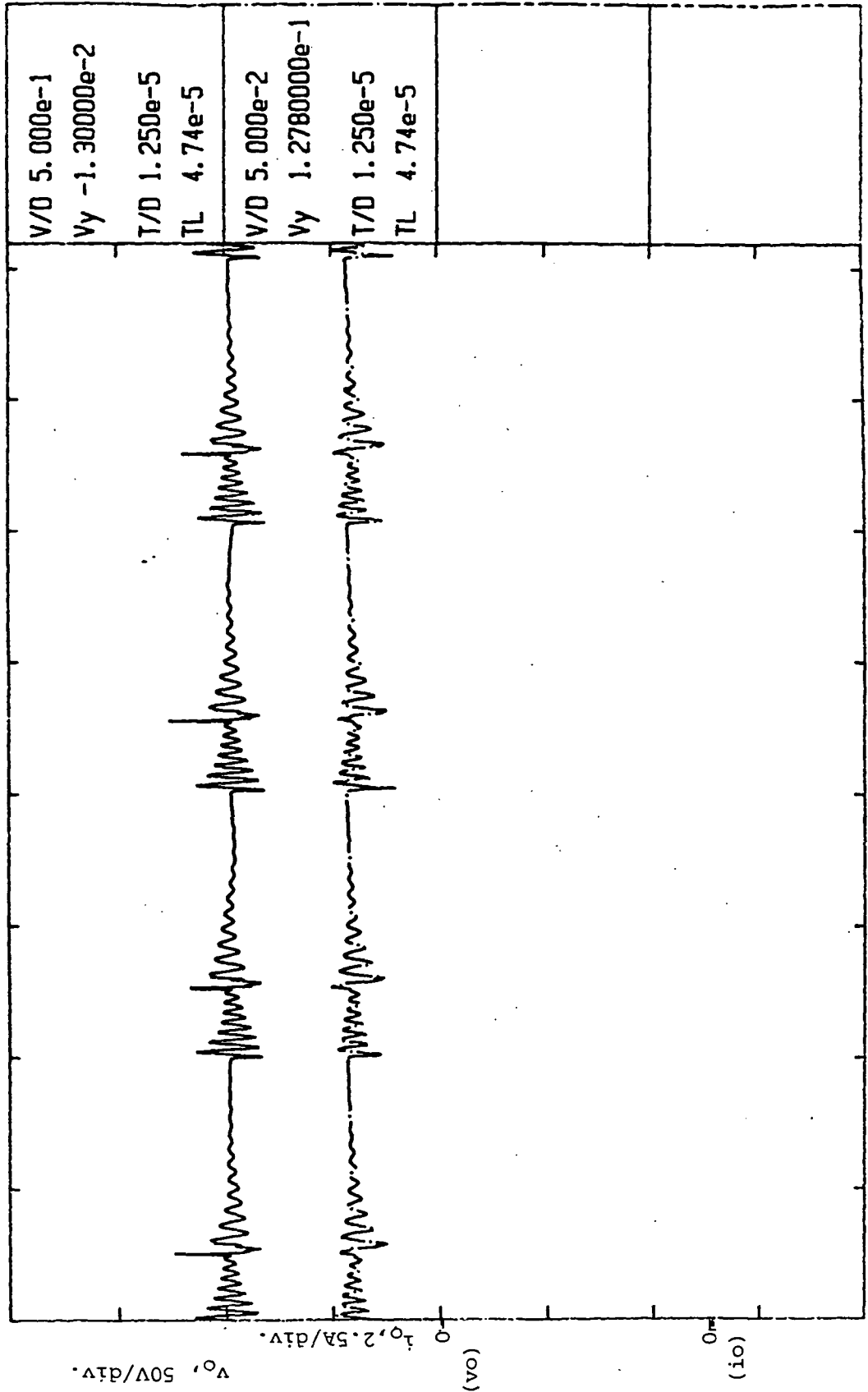|			
V/D 5.000e-1	T/D 5.00e-4	V/D 5.000e-2	T/D 5.00e-4
Vy -1.40000e-2	TL -2.555e-4	Vy 1.2780000e-1	TL -2.555e-4

Vy

v_o, 50V/div.

i_o, 25A/div.

Vx

500us/div.

TL
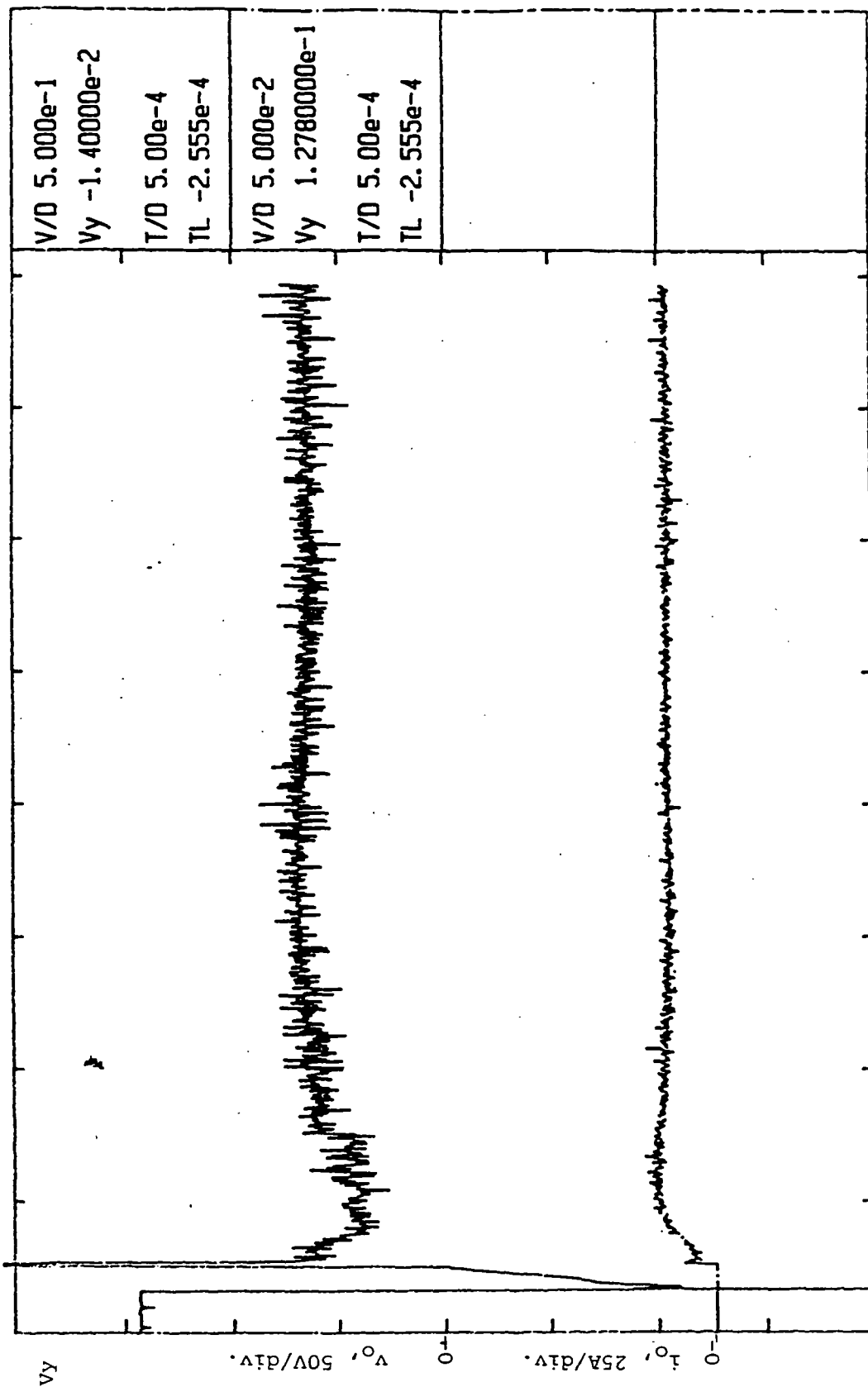
Fig.8.6. vo and io at ignition with $I_{limit} \cong 12.5A$. peak.
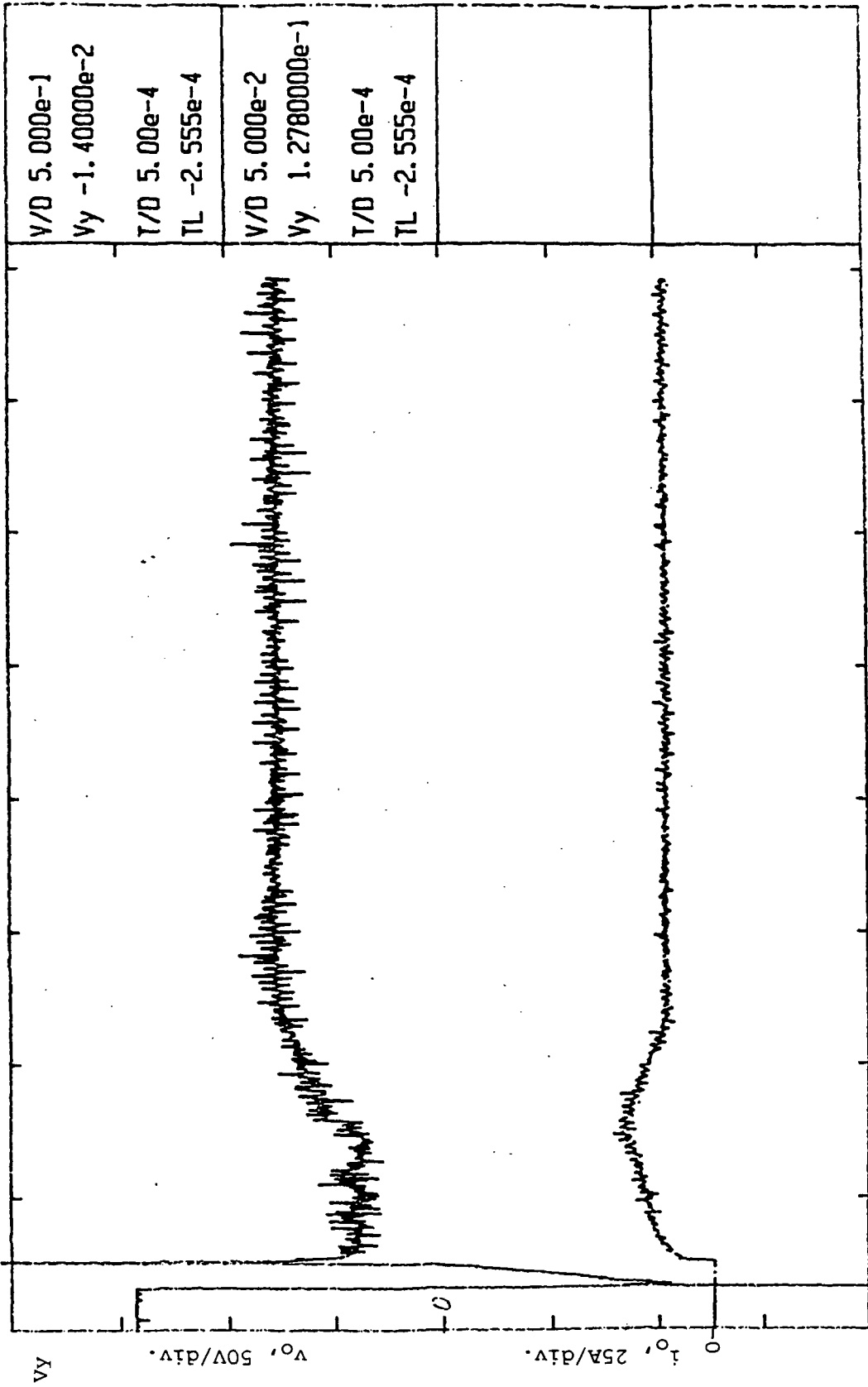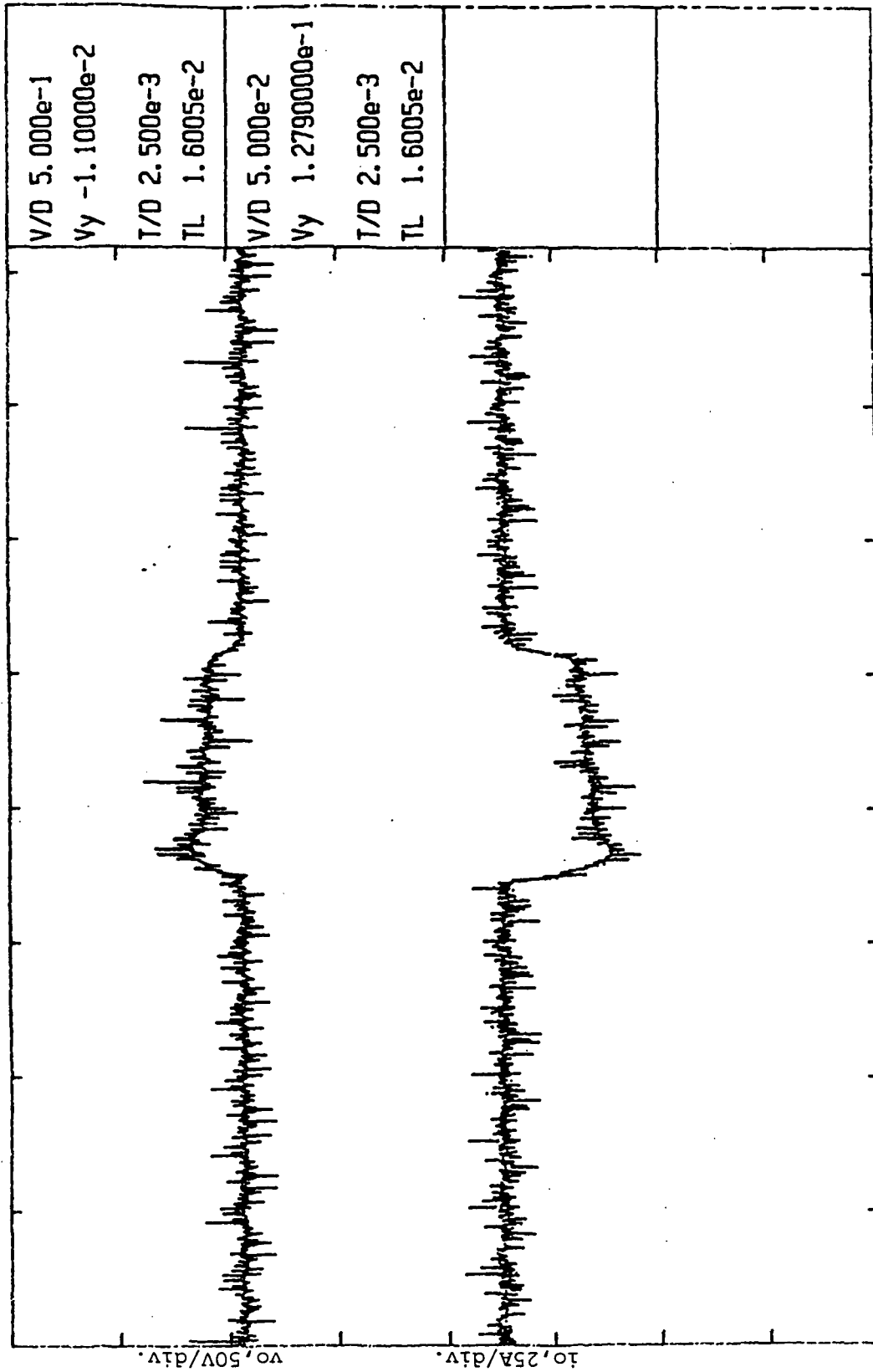
Fig. 8.7. vo and io at ignition with Ilimit ≅ 21 A. peak

Fig. 8.8. Steady state vo and io (output voltage and current ripple).

V/D	5.000e-1	
Vy	-1.10000e-2	
T/D	2.500e-3	
TL	1.6005e-2	
V/D	5.000e-2	
Vy	1.2790000e-1	
T/D	2.500e-3	
TL	1.6005e-2	

vo,50V/div.

io,25A/div.

Vx

2.5m.s./div.

TL

Fig. 8.9. Response of vo and io to a step change in the current reference.

V/D 1.000e1
Vy -3.00000e-1
T/D 3.125e-6
TL -3.9e-6

V/D 5.000e-2
Vy 1.2800000e-1
T/D 3.125e-6
TL -3.9e-6

3.125us/div.

Vx
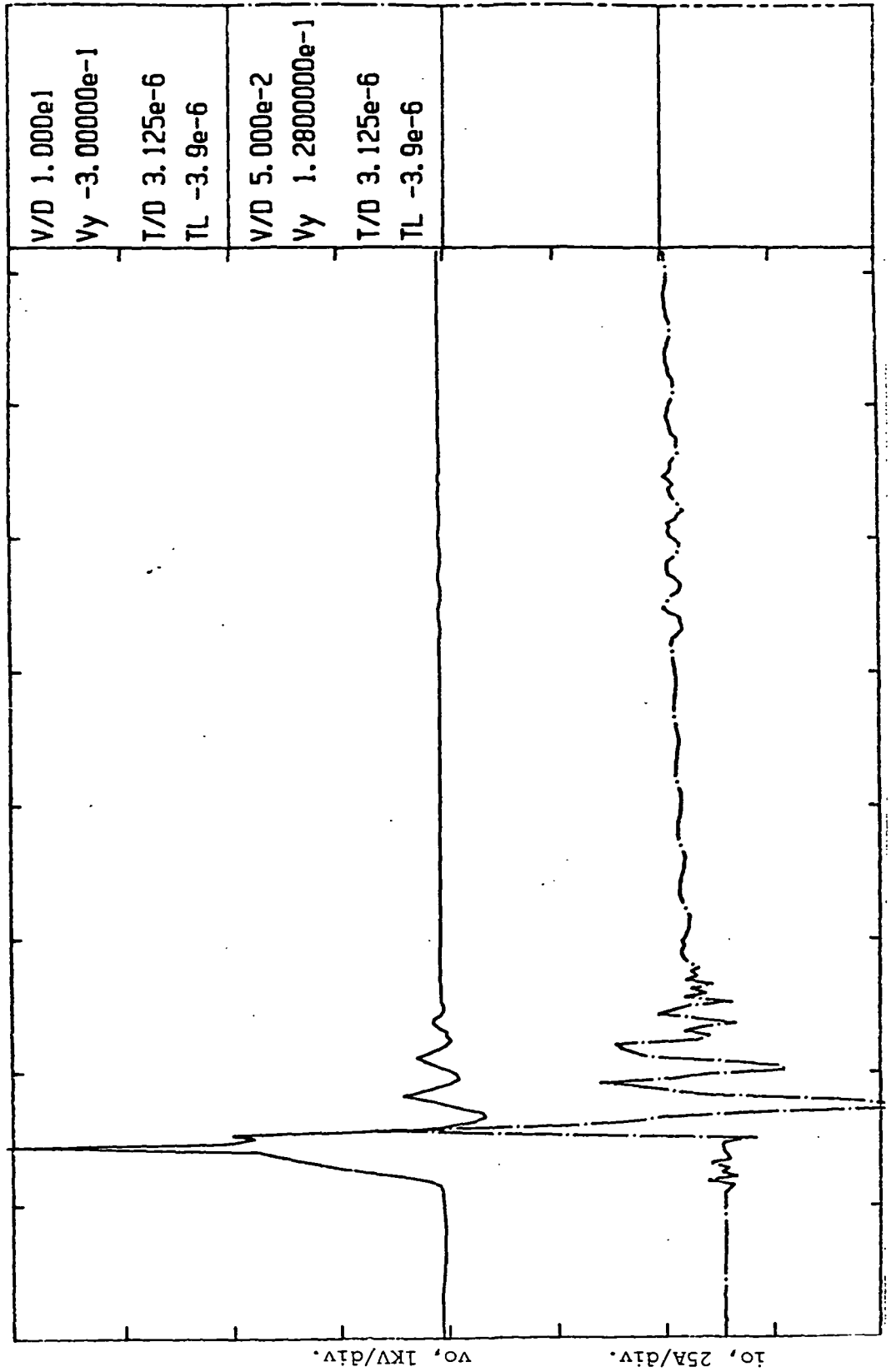
TL

Vo, 1KV/div.

Io, 25A/div.
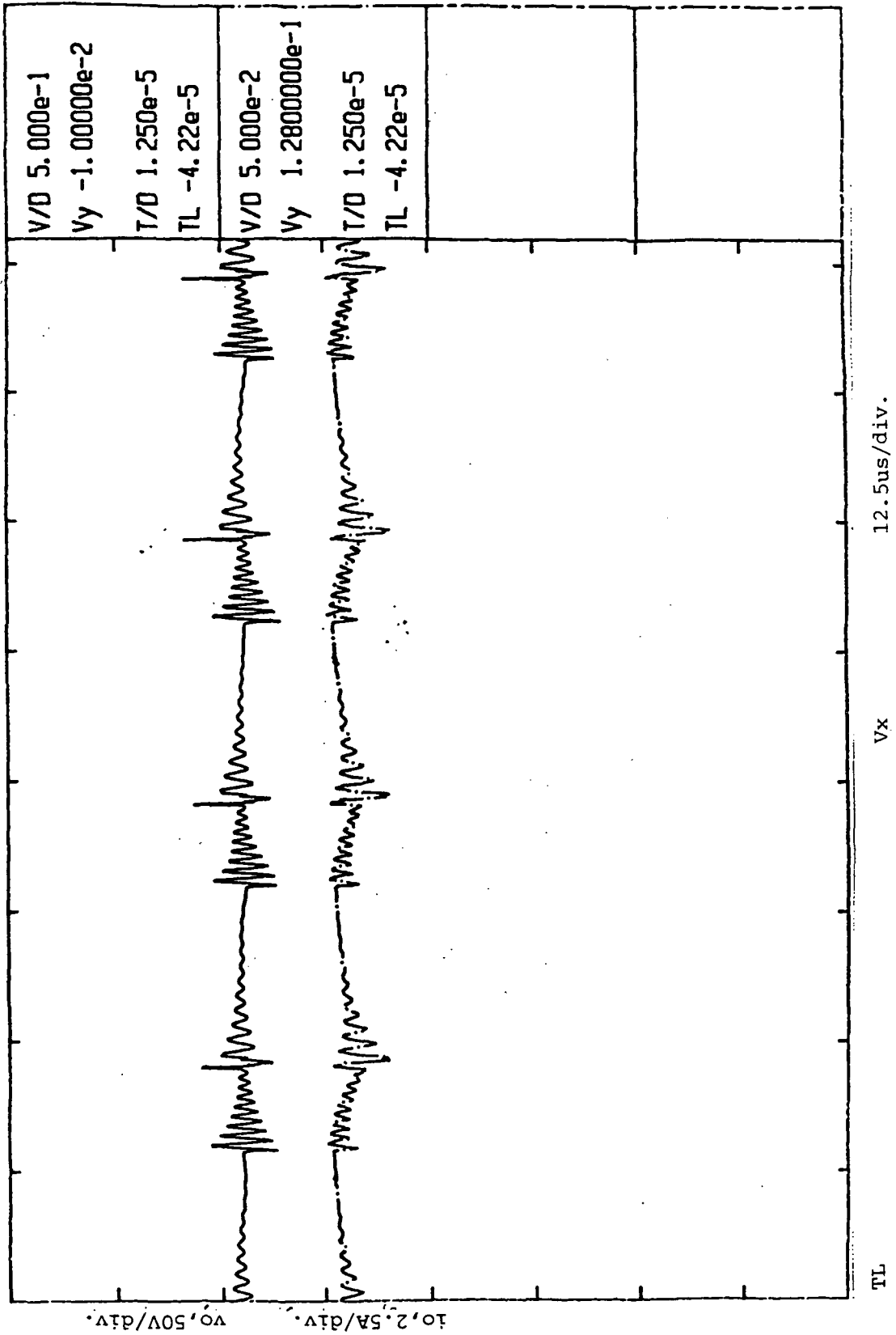
Fig. 8.11. Steady state vo and io with 384uH choke (output voltage and current ripple).

V/D	5.000e-2
Vy	1.2800000e-1
T/D	1.250e-4
TL	-4.9e-5

V/D	1.000e1
Vy	-3.20000e-1
T/D	1.250e-4
TL	-4.8e-5

Vo, 1KV/div.

Io, 25A/div.

125us/div.

Vx
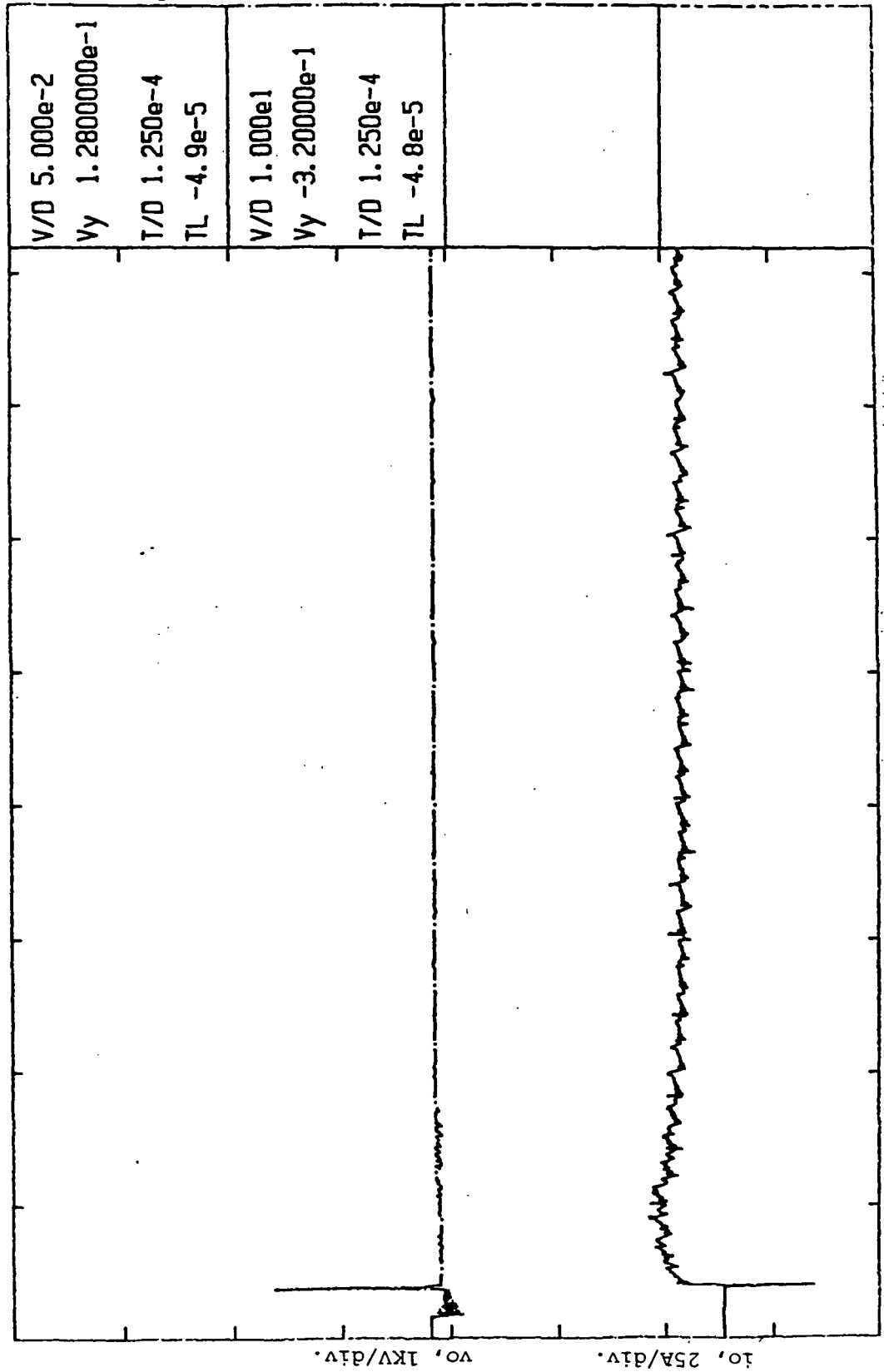
TL

Chapter 9

SUMMARY FOR PART II

It appears that the arcjet power supply functions properly and no operating problems were observed. Every attempted ignition was successful, and the control circuit appears to be immune from EMI and instability problems. Of course, further optimization is always possible, and there are certain areas of investigation that might lead to reductions in cost and/or weight. One of those may be a further reduction in the output filter choke, since values below 384 μH were not tested.

REFERENCES

[1] Curran, F. M. and Haag, T. W., "An Extended Life and Performance Test of a Low Power Arcjet," *Conference Record of the 24th Joint Propulsion Conference*, AIAA 88-3106, July 1988.

[2] Gruber, R. P., "Power Electronics for a 1-Kilowatt Arcjet Thruster," *Conference Record of the 22nd Joint Propulsion Conference*, AIAA 86-1507, June 1986.

[3] "Lewis Research Center 1941-1991: A Half Century of Technology Leadership," *NASA Tech Briefs*, p.13, May 1991.

[4] Hamley, J. A., "Arcjet Load Characteristics," *Conference Record of the 21st International Electric Propulsion Conference*, AIAA-90-2579, July 1990.

[5] Gruber, R. P., "5KW Arcjet Power Electronics," *Conference Record of the 25th Joint Propulsion Conference*, AIAA-89-2725, July 1989.

[6] Kassakian, J. G. and Lau, D., "An Analysis and Experimental Verification of Parasitic Oscillations in Parallel Power MOSFETs," *IEEE Transactions on Electron Devices*, pp. 959-963, Vol. ED-31, No. 7, July 1984.

[7] "Motorola Linear and Interface ICs," Series D, Motorola Inc., Pheonix, Arizona, pp. 11-22 to 35, 1983.

[8] "PSpice User's Guide," Microsim Corporation, Irvine, California, 1990.

[9] "11401 and 11402 Digitizing Oscilloscopes User's Reference Manual," Tektronix,

Inc., Beaverton, Oregon, 1988.

[10] Cornu, J., "Advanced Welding Systems: Consumable Electrode Processes," IFS (Publications) Ltd., Bedford, UK and Springer-Verlag, Berlin, Germany, Vol. 2, p. 22, 1988.

[11] "3562A Dynamic Signal Analyzer Operating Manual," Hewlett-Packard Co., Everett, Washington, 1985.

[12] Stuart, T. A., King, R. J. and Chen, K., "An Investigation of Full Bridge DC/DC Converters for Arcjet Thrusters," Report prepared for the NASA Lewis Research Center on Grants NAG3-959 and NAG3-1102, The University of Toledo, December 1990.

[13] Sarmiento, C. J. and Gruber, R. P. "Low Power Arcjet Thruster Pulse Ignition," *Conference Record of the 23rd Joint Propulsion Conference*, AIAA-87-1951, June-July 1987.

[14] Mitchell, D. M., "DC-DC Switching Regulator Analysis," McGraw-Hill, New York, New York, pp. 117-119, 1988.

[15] Cho, Bo H. and Lee, C. Y., "Modeling and Analysis of Spacecraft Power Systems," *IEEE Transactions on Power Electronics*, pp. 44-54, Vol. 3, No. 1, January 1988.